

# DECOHERENCE AND EXCITATION-TRANSFER MECHANISMS IN SEMICONDUCTOR QUANTUM DOTS

THÈSE N° 3812 (2007)

PRÉSENTÉE LE 8 JUIN 2007

À LA FACULTÉ DES SCIENCES DE BASE

UNITÉ DU PROF. SAVONA

PROGRAMME DOCTORAL EN PHYSIQUE

ÉCOLE POLYTECHNIQUE FÉDÉRALE DE LAUSANNE

POUR L'OBTENTION DU GRADE DE DOCTEUR ÈS SCIENCES

PAR

Gaetano PARASCANDOLO

Laurea in fisica, Università degli studi di Napoli Federico II, Napoli, Italie  
et de nationalité italienne

acceptée sur proposition du jury:

Prof. R. Schaller, président du jury

Prof. V. Savona, directeur de thèse

Prof. A. Fiore, rapporteur

Dr W. Langbein, rapporteur

Dr P. Schwendimann, rapporteur



ÉCOLE POLYTECHNIQUE  
FÉDÉRALE DE LAUSANNE

Suisse, EPFL

2007



# Abstract

The aim of this thesis is to supply a theoretical study of the interaction mechanisms between quantum dots beyond the simple picture of macroatoms. Coulomb interaction between excitons, exciton-phonon interaction as well as radiative interaction are, in particular, considered. These mechanisms can be exploited to coherently couple quantum dots, thus being the physical tool enabling quantum information processing using quantum-dot-based logic gates. On the other hand, the same mechanisms are responsible for the decoherence of the quantum-state that prevent the storing of the quantum information.

Already if considered as simple two-level systems, quantum dots are subject to mutual interaction. Quantum dots in the excited state can be considered as dipoles, and are thus coupled with each other via the dipole-dipole electrostatic interaction. This results in excitation transfer between dots over distances of a few tens of nanometers. In Chapter 2 we show that taking into account the retarded nature of the electromagnetic field results in a correction to this effect, that become a leading contribution at large distances, effectively coupling quantum dots over distances of a few hundreds of nanometers.

Strong exciton-phonon-coupling in quantum dots results in a very efficient decoherence mechanism. The strongly localized polarization in an excited quantum dot can induce virtual phonon emission and reabsorption processes which act as a phase-destroying mechanism. In quantum dot molecules the decay rate of the interband polarization is almost one order of magnitude larger than in the single quantum dot case, and depends on the interdot distance. The description of this coupling mechanism is possible only beyond the macroatom picture. In Chapter 3 we develop a model that describes the phonon-mediated interaction between quantum dots in a dot molecule, explaining the strong distance dependence of the exciton dephasing rates in terms of a matching condition between the phonon wavelength and the interdot distance, which enhances the phonon-assisted scattering from bright to dark states.

The heterodyne spectral interferometry is a novel implementation of tran-

sient nonlinear spectroscopy that enables to study the transient nonlinear polarization emitted from individual localized electronic transitions, in both intensity and phase. Two-dimensional spectra obtained by means of this technique display signals that can be associated to the coherent coupling between different resonances of the system under study. This technique is theoretically modeled for the first time in Chapter 4, where a very satisfactory description of the measured spectra is provided, showing that coherent coupling between different optical transitions of a quantum system result in off-diagonal peaks of the two-dimensional excitation spectrum. Furthermore, we show that in the low intensity regime, each spectral signal can be associate to a specific pair of coupled resonances as long as the level structure of the system under study is known.

**Keywords:** semiconductors, excitons, nanostructures, quantum dots, quantum dot molecules, Coulomb correlation, radiative interaction, resonant excitation transfer, exciton-phonon coupling, nonlinear spectroscopy, four wave mixing, heterodyne spectral interferometry.

# Riassunto

Scopo di questa tesi è lo studio teorico di alcuni meccanismi di interazione tra quantum dot descritti al di là del semplice modello di macroatomo. Sono trattati, in particolare, l'interazione Coulombiana tra eccitoni, l'interazione eccitone-fonone e l'interazione radiativa. Questi meccanismi possono essere sfruttati per realizzare l'accoppiamento coerente tra quantum dot, e pertanto risultano essere gli strumenti adatti a realizzare schemi computazionali di informazione quantistica su porte logiche basate su quantum dot. D'altra parte, gli stessi meccanismi sono responsabili della decoerenza dello stato quantistico che impedisce di immagazzinare l'informazione.

Già se considerati come semplici sistemi a due livelli, i quantum dot sono soggetti a mutua interazione. Quantum dot che si trovino nel proprio stato eccitato possono essere considerati come dipoli elettrici, e quindi sono accoppiati tramite interazione elettrostatica dipolo-dipolo. Ne risulta un trasferimento dell'eccitazione su distanze di poche decine di nanometri. Nel Capitolo 2 mostriamo che prendere in considerazione la natura ritardata del campo elettromagnetico risulta in una correzione a questo effetto, che diventa dominante a grandi distanze, accoppiando efficientemente quantum dot su distanze di poche centinaia di nanometri.

L'accoppiamento forte eccitone-fonone nei quantum dot è causa di meccanismi di decoerenza efficienti. La polarizzazione fortemente localizzata in un quantum dot eccitato può indurre processi virtuali di emissione e riassorbimento di fononi, che agiscono come meccanismi di perdita di fase. In molecole di quantum dot il tasso di decadimento della polarizzazione interbanda è circa un ordine di grandezza maggiore che in quantum dot isolati, e dipende dalla distanza tra i dot. Una descrizione del meccanismo di accoppiamento è possibile solo al di là dello schema di macroatomo. Nel Capitolo 3 sviluppiamo un modello tramite cui è descritta l'interazione mediata da fononi tra i quantum dot che formano una molecola, spiegando la forte dipendenza del tasso di perdita di fase dell'eccitone in termini di una condizione di matching tra la lunghezza d'onda del fonone e la distanza tra i dot, che favorisce l'interazione assistita da fononi tra stati otticamente attivi e non attivi.

La heterodyne spectral interferometry è una nuova implementazione di spettroscopia transiente non lineare che permette lo studio sia dell'intensità che della fase della polarizzazione emessa da transizioni elettroniche isolate e localizzate. Negli spettri bidimensionali ottenuti tramite questa tecnica sono osservati segnali che si suppone essere associati all'accoppiamento coerente tra diverse risonanze del sistema in analisi. Nel Capitolo 4 sviluppiamo il primo modello teorico capace di descrivere questa tecnica, che fornisce una descrizione soddisfacente degli spettri misurati sperimentalmente, mostrando che l'accoppiamento coerente tra diverse transizioni ottiche di un sistema quantistico si manifesta in picchi non diagonali nello spettro bidimensionale di eccitazione. Inoltre, mostriamo che nel regime di basse intensità, ogni segnale spettrale può associarsi ad una specifica coppia di risonanze accoppiate, fintanto che la struttura dei livelli del sistema in analisi è nota.

**Parole chiave:** semiconduttori, eccitoni, nanostrutture, quantum dot, molecole di quantum dot, correlazione Coulombiana, interazione radiativa, trasferimento risonante d'eccitazione, accoppiamento eccitone-fonone, spettroscopia non lineare, mixing a quattro onde, heterodyne spectral interferometry.

# Contents

Abstract, Keywords . . . . .	i
Riassunto, Parole chiave . . . . .	iii
<b>1 Introduction</b>	<b>1</b>
1.1 Semiconductor materials: from bulk to quantum dots . . . . .	4
1.1.1 Bulk semiconductors . . . . .	4
1.1.2 Quantum wells, wires and dots . . . . .	8
1.1.3 Wannier excitons in semiconductors . . . . .	10
1.1.4 Quantum dot fabrication. Self-assembling . . . . .	12
1.2 Quantum dot carrier wave functions . . . . .	13
1.3 Coulomb interaction in quantum dots . . . . .	19
<b>2 Long-range radiative coupling between semiconductor QDs</b>	<b>23</b>
2.1 The Maxwell-Schrödinger formalism . . . . .	26
2.1.1 The linear susceptibility tensor . . . . .	26
2.1.2 The scattering approach . . . . .	27
2.2 The coupling tensor . . . . .	30
2.3 Numerical results . . . . .	33
2.3.1 LT spitting for one anisotropic QD . . . . .	33
2.3.2 Two QDs: dependence on distance and detuning . . . . .	35
2.3.3 N-QDs ensemble . . . . .	37
2.4 Conclusions . . . . .	41
<b>3 Phonon-induced exciton dephasing in QD molecules</b>	<b>43</b>
3.1 Exciton-phonon coupling in second order Born approximation	46
3.1.1 QD molecule and interaction Hamiltonian . . . . .	46
3.1.2 Density matrix formalism . . . . .	48
3.2 Results . . . . .	54
3.3 Conclusions . . . . .	62

---

<b>4</b>	<b>Coherent coupling of localized exciton transitions</b>	<b>63</b>
4.1	Four-wave-mixing and heterodyne spectral interferometry . . .	65
4.2	Formulation of the model . . . . .	68
4.2.1	Hamiltonian and density matrix approach . . . . .	69
4.2.2	Simulation of HSI experiments - response to a two- $\delta$ - pulses excitation field . . . . .	72
4.3	Results . . . . .	74
4.4	Conclusions . . . . .	84
	<b>Conclusions</b>	<b>87</b>
<b>A</b>	<b>Microscopic derivation of Coulomb interaction in crystals</b>	<b>91</b>
	Acknowledgments . . . . .	97
	<b>Bibliography</b>	<b>99</b>
	Curriculum Vitae . . . . .	113

# Chapter 1

## Introduction

Semiconductor Quantum Dots (QDs) are solid-state structures that provide a confinement of carriers. This results in a discrete energy spectrum for electrons and holes and, consequently, in atomic-like electronic and optical properties. In QD systems, the energy scales and other physical properties can be tuned, by varying the structural properties of the QD. They therefore represent an ideal system for both experimental and theoretical investigations, where the light matter interaction can be studied in a fully controlled, well-characterized environment. All these features make semiconductor QDs very appealing for the realization of highly performing electro-optical devices [Bimb 99].

In the limit of strong confinement, the so-called *macroatom* [Zana 98, Biol 00] regime, QDs can be considered as two-level systems. This makes them good candidates for the realization of a *quantum-bit* (qubit), the basic unit of a quantum computer, that can be thought of as a physical system having a quantum mechanical degree of freedom whose quantum state can be systematically controlled [Benn 00, Bouw 00]. Furthermore, the requirement for a quantum information device to be scalable up to a large number of qubits and to be integrated into conventional electronics, can be accomplished by solid state implementations, making semiconductor QDs more interesting than other systems, such as atomic or nuclear spins or photons [QCR 04].

Present ultrafast laser technology allows to coherently generate and manipulate exciton states in QDs over very short time scales in the 100 fs range. Rabi oscillations (RO) of the population inversion that are typical of two discrete level systems, have been observed and characterized in the exciton-ground state transition of several QD ensembles [Kama 01, Borr 02, Htoo 02]. The inversion of the two-level QD-system can be induced via optical pumping of the sample [Zren 02, Patt 05]. Several proposals of realizing all-optical gates able to perform single- and two-qubit operations on a subpicosecond

time scale are based on single QDs [Troi 00, Li 03] or arrays of interacting QDs [Zana 98, Biol 00, Love 03, Bert 04, Vill 04].

Data processing needs quantum logic gates between, at least, two coupled qubits. The coupling must be coherent so that the quantum information is not lost during the gate operation. Among all the geometrical schemes proposed for implementing quantum gates, that of QD molecules (QDM) have attracted great attention. A QDM consists of a vertically stacked pair of InAs QDs formed via strain-driven self assembly in a GaAs matrix. Spectroscopic observation of coherent coupling between exciton states in QDM and state manipulation using both magnetic [Ortn 03] and electric fields [Baye 01, Kren 05, Ortn 05a, Stin 06] have been reported. The evidence for the coherence of the two states is obtained from anticrossing in the fine structure of their energy levels. The coupling between the exciton states arises from the interplay between the tunneling of the carrier wave functions and their Coulomb interaction.

One of the greatest obstacles to the implementation of quantum computation schemes is *decoherence*, i.e. the spoiling of the unitary character of quantum evolution due to an uncontrolled coupling to environmental degrees of freedom. Robustness against decoherence of the interband polarization in QDs is expected as a result of quantum confinement, that results in discrete energy levels with a very restricted phase space available for various scattering mechanisms. This simplified view was however recently questioned, after the observation of a very effective decoherence mechanism due to strong electron-phonon coupling [Beso 01, Borr 01, Fave 03]. The strongly localized polarization in an excited QD can induce virtual inelastic phonon emission and reabsorption processes which act as a phase-destroying mechanism.

In the same simplified picture, QDs in an ensemble would basically behave as non-interacting objects, as long as no external field is applied. Experiments performed on QDM [Borr 03] show instead that the decay rate of the interband polarization is almost one order of magnitude larger than in the single QD case, and depends on the interdot distance, thus proving that the two dots in a QDM are not isolated.

Phonon-coupling is a typical example of an interaction mechanism occurring via overlapping wave functions. However, interaction between polarizable media can also take place without tunneling. The prototype of this class of mechanisms is the dipole-dipole electrostatic interaction, also known as *Förster Resonant Energy Transfer* (FRET), that is responsible of excitation transfer over distances of a few tens of nanometers. This mechanism originates from the spin-scattering component of the exchange Coulomb interaction, and then is contained in the instantaneous limit of the electromagnetic interaction. Taking into account the retarded nature of the electromag-

netic field gives a correction to FRET, that becomes a leading contribution for large interdot distances [Para 05, Hugh 06, Para 07]. This means that QDs are expected to generate a cooperative radiation field and then interact through it over a distance range of the order of the wavelength, i.e. a few hundreds of nanometers. This picture is supported by a recent experimental observation [Sche 07] of the influence of the QD density on the photoluminescence decay rate in single mesas.

This thesis presents a theoretical description of the various interaction mechanisms between excitons in semiconductor QDs beyond the simple picture of macroatoms. The solutions and predictions of the theoretical models are closely compared with recent experiments, mostly focusing on coherent optical spectroscopy.

In Chapter 2 we develop a Maxwell–Schrödinger formalism in order to describe the radiative interaction mechanism between semiconductor quantum dots. We solve the Maxwell equations for the electromagnetic field coupled to the polarization field of a quantum dot ensemble through a linear non-local susceptibility and compute the polariton resonances of the system.

The radiative coupling, mediated by both radiative and surface photon modes, causes the emergence of collective modes whose lifetimes are longer or shorter compared to the ones of non-interacting dots. The magnitude of the coupling and the collective mode energies depend on the detuning and on the mutual quantum dot distance. The spatial range of this coupling mechanism is of the order of the optical wavelength. This part of the work was the first theoretical prediction, back in 2005, of the radiative coupling mechanism, that has been very recently the object of experimental verification [Sche 07].

In Chapter 3 we develop a theory of the linear optical spectrum of excitons in QDM, including the effect of exciton-phonon coupling in the second-order Born approximation. The model reproduces both the phonon broadband and the broadening of the zero-phonon line (ZPL) that characterize the spectra of exciton resonances in a QD system [Beso 01, Borr 01, Krum 02, Zimm 02, Fave 03, Lang 04b, Mulj 04]. The general trend of the ZPL broadening as a function of interdot distance that were recently measured [Borr 03], namely the unexpectedly broad linewidths and their large variation as a function of the distance, is explained in terms of both the non-Markov nature of the coupling and of the matching of the phonon wavelength to the interdot distance.

In Chapter 4 we supply a theoretical analysis of a novel implementation of transient nonlinear spectroscopy, the heterodyne spectral interferometry (HSI) [Lang 06, Lang 07]. This technique is based on two-dimensional Fourier transform spectroscopy and enables to study the transient nonlinear polarization emitted from individual localized electronic transitions, in both

intensity and phase. In the framework of a density matrix approach, written for a multilevel system of Coulomb correlated exciton and biexciton states, we show that the coherent coupling between two states results in off-diagonal peaks of the two-dimensional FWM spectrum, thus confirming the interpretation of Langbein *et al.* [Lang 06, Lang 07] of the observed HSI spectra. We then give a solid theoretical support to a powerful experimental technique enabling to identify the coherent coupling between strongly confined quantum systems *independently* from the coupling mechanism.

Throughout this thesis, QD states are modeled in the effective mass approximation – a powerful theoretical tool for studying the electronic and optical properties of crystals. In the Sec. 1.1 we give a brief overview of the calculation of the electronic structure of bulk semiconductors and nanostructures and of the derivation of the Wannier exciton in semiconductors. In particular, in Sec. 1.1.4 we briefly describe the system of self-organized InAs/GaAs quantum dots, showing that the particular geometrical arrangement of QDs in such a sample is intrinsically related to the self-assembling growth technique. The envelope function for carriers confined in this model QD system is calculated in Sec. 1.2, and will be at the basis of the three presented results. Finally, in Sec. 1.3 we show how the Coulomb interaction between the electron-hole pair states calculated in Sec. 1.2 is taken into account in order to describe, at least partially, Coulomb correlation effects.

## 1.1 Semiconductor materials: from bulk to quantum dots

### 1.1.1 Bulk semiconductors

The energy levels of electrons in isolated atoms are discrete. However, when  $\sim 10^{23}$  atoms are closely packed in a crystal structure, the energy levels split up into bonding and anti-bonding states leading to the formation of continuous energy bands. In semiconductors, at zero temperature the electrons *completely* fill the lower energy bands up to the so-called *valence band* (VB), leaving unoccupied the successive *conduction band* (CB). For this kind of material, the minimum of the CB and the maximum of the VB are separated by a band gap  $E_g$  whose magnitude is of the order of 1 eV.

The calculation of the crystal band structure implies solving the Schrödinger equation describing the many-body Coulomb interaction between all crystal electrons and nuclei, here considered as spinless particles. This is an impossible task that requires a series of approximations. As the masses of the nuclei are several order of magnitude larger than the free electron mass, their

motion can be described on a timescale much larger than that of the electron motion. One can assume that the nuclei, fixed in the equilibrium positions of the lattice  $\mathbf{R}_i$ , generate a potential  $V_0(\{\mathbf{R}_i\})$  in which the Coulomb interacting electrons move (in the following, as  $\mathbf{R}_i$  are fixed we set  $V_0 = V_0(\{\mathbf{R}_i\})$ ). Then, the eigenvalues of the electronic problem  $E_n(\{\mathbf{R}_i\})$  enter as a potential in the problem of the lattice vibrations. The described approach is known as the *adiabatic* (Born-Oppenheimer) approximation, because the electrons *adiabatically* follow the motion of the nuclei. The further step is to assume the *mean field* approximation, that allows to solve of the electron problem with the hypothesis that each electron experiences the same average potential  $V(\mathbf{r})$  due to the interaction with all the other electrons. The motion of a single electron is the solution of the Schrödinger equation

$$\left( \frac{p^2}{2m} + U(\mathbf{r}) \right) \psi_n(\mathbf{r}) = E_n \psi_n(\mathbf{r}), \quad (1.1)$$

where  $n$  is the band index and  $U(\mathbf{r}) = V_0 + V(\mathbf{r})$  is the periodic crystal potential, that can be calculated from *first principles* or by empirical approaches. In the second case,  $U(\mathbf{r})$  is expressed in terms of parameters which are determined fitting experimental results. In quantum optics experiments, one measures both energy gaps and oscillator strengths of the transitions. In the  $\mathbf{k} \cdot \mathbf{p}$  method [Yu 96] the band structure over the entire Brillouin zone (i.e. the elementary cell in reciprocal space) can be extrapolated from the zone center energy gaps and optical matrix elements. Thus, the  $\mathbf{k} \cdot \mathbf{p}$  method is particularly suitable for interpreting the optical spectra. Using the Bloch theorem, the solutions of Eq. (1.1) read

$$\phi_{n,\mathbf{k}}(\mathbf{r}) = u_{n,\mathbf{k}}(\mathbf{r}) \exp(i\mathbf{k} \cdot \mathbf{r}), \quad (1.2)$$

where  $\mathbf{k}$  lies in the Brillouin zone, and  $u_{n,\mathbf{k}}(\mathbf{r})$  has the periodicity of the lattice. When  $\phi_{n,\mathbf{k}}(\mathbf{r})$  is substituted into (1.1) we obtain an equation for  $u_{n,\mathbf{k}}(\mathbf{r})$  of the form

$$\left( \frac{p^2}{2m} + \frac{\hbar \mathbf{k} \cdot \mathbf{p}}{m} + \frac{\hbar^2 k^2}{2m} + U(\mathbf{r}) \right) u_{n,\mathbf{k}}(\mathbf{r}) = E_{n,\mathbf{k}} u_{n,\mathbf{k}}(\mathbf{r}). \quad (1.3)$$

Once  $E_{n,\mathbf{k}}$  and  $u_{n,\mathbf{k}}(\mathbf{r})$  are calculated for a fixed point  $\mathbf{k}$  in the Brillouin zone, the solutions at a neighboring point  $\mathbf{k} + \delta\mathbf{k}$  are found treating the terms  $\hbar\delta\mathbf{k} \cdot \mathbf{p}/m$  and  $\hbar^2\delta k^2/2m$  as perturbations in Eq. (1.3), using either the degenerate or nondegenerate perturbation theory. Let us focus on the case of a band that is nondegenerate at the energy  $E_{n,\mathbf{k}}$ . Around  $\mathbf{k}$  the dispersion reads

$$E_{n,\mathbf{k}+\delta\mathbf{k}} = E_{n,\mathbf{k}} + \frac{\hbar}{m} \delta\mathbf{k} \cdot \mathbf{p}_{n,n} + \frac{\hbar^2 \delta k^2}{2m} + \frac{\hbar^2}{m^2} \sum_{m \neq n} \frac{|\delta\mathbf{k} \cdot \mathbf{p}_{n,m}|^2}{E_{n,\mathbf{k}} - E_{m,\mathbf{k}}}, \quad (1.4)$$

where  $\mathbf{p}_{n,m} = \langle u_{n,\mathbf{k}} | \mathbf{p} | u_{m,\mathbf{k}} \rangle$  are the matrix elements of the optical transitions and  $E_{n,\mathbf{k}} - E_{m,\mathbf{k}}$  the energy gaps. The limit  $\delta\mathbf{k} \rightarrow (0,0,0)$  shows the continuity of the energy in any point of the Brillouin zone where  $E_{n,\mathbf{k}}$  is nondegenerate. In this limit, one define the effective mass tensor, whose components are

$$\begin{aligned} \frac{1}{m_{ij}^*} &= \frac{1}{\hbar^2} \frac{\partial^2 E_{n,\mathbf{k}+\delta\mathbf{k}}}{\partial k_i \partial k_j} \\ &= \frac{1}{m} \delta_{i,j} + \frac{1}{m^2} \sum_{m \neq n} \frac{p_{n,m}^i p_{m,n}^j + p_{n,m}^j p_{m,n}^i}{E_{n,\mathbf{k}} - E_{m,\mathbf{k}}}. \end{aligned} \quad (1.5)$$

In semiconductors, the interesting point in the Brillouin zone are the minima of the CB and the maxima of the VB. In correspondence of the extrema, and in terms of the effective mass tensor, Eq. (1.4) reads

$$E_{n,\mathbf{k}+\delta\mathbf{k}} = E_{n,\mathbf{k}} + \frac{\hbar^2}{2} \sum_{i,j} \frac{\delta k_i \delta k_j}{m_{ij}^*}. \quad (1.6)$$

Around these points one can assume a constant, possibly direction dependent, effective mass. Many semiconductors have an absolute minimum at  $\mathbf{k} = (0,0,0)$  where, moreover, the effective mass is scalar. Then, the electron dispersion (1.6) in the CB simplifies to

$$E_{n,\mathbf{k}} = E_{n,0} + \frac{\hbar^2 k^2}{2m^*}, \quad (1.7)$$

that is a function quadratic in  $|\mathbf{k}|$ , and  $m^*$  is given by

$$\frac{1}{m^*} = \frac{1}{m} + \frac{2}{m^2 k^2} \sum_{m \neq n} \frac{|\mathbf{k} \cdot \mathbf{p}_{n,m}|^2}{E_{n,0} - E_{m,0}}. \quad (1.8)$$

The electron in the CB behaves as a free electron in the vacuum with modified mass  $m^*$  that accounts for the coupling between the electronic states of the different bands via the  $\mathbf{k} \cdot \mathbf{p}$  term. The electron will e.g. accelerate when it is subject to an electric field, yielding charge current. This description of the electron in the crystal, derived from the  $\mathbf{k} \cdot \mathbf{p}$  method, is known as *effective mass approximation* (EMA). On the other hand, electrons in a fully occupied VB will not be affected by small electric fields, since no free states of higher energy are available in the VB. However, if an electron is removed from the VB, a free state becomes available, which can move similarly to the electron in the CB. Such a free VB state can be regarded as a positively charged particle, which is referred to as a *hole*.

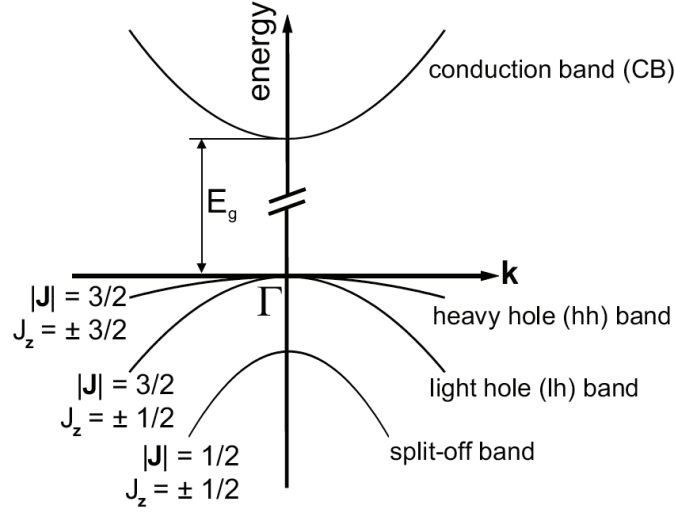


Figure 1.1: Band structure of GaAs as resulting from the effective mass approximation. Around the  $\Gamma$ -point ( $\mathbf{k} = 0$ ) the energy bands have parabolic dispersion.

For the calculation of the VB structure, we focus on crystals with cubic lattice symmetry (e.g. GaAs). In this case, a degeneracy for  $|\mathbf{k}| = 0$  has to be taken into account. Coupling the degenerate bands via a Kohn-Luttinger Hamiltonian matrix [Lutt 55] results again in a parabolic band description, but with two different effective hole masses. Corresponding bands are referred to as the heavy hole (hh) and light hole (lh) band with angular momentum  $|\mathbf{J}| = 3/2$  and projections on the  $z$ -axis (i.e. the direction of the  $\mathbf{k}$  vector)  $J_z = \pm 3/2$  and  $J_z = \pm 1/2$ , respectively. In addition, there is the split-off band corresponding to  $|\mathbf{J}| = 1/2$  which is shifted down in energy as an effect of spin-orbit coupling. The corresponding dispersion curves are illustrated in Fig. 1.1.

Electron-hole recombination in semiconductors results in the emission of a photon corresponding to the total energy of the electron hole pair. The light emitted due to such an optical transitions is referred to as luminescence. Due to momentum and energy conservation radiative recombination is only allowed for electrons and holes with identical  $\mathbf{k}$ , since the momentum of the emitted photon is negligible as compared to that of the recombining carriers. In general, the CB has additional local energy minima displaced from  $\mathbf{k} = (0, 0, 0)$ . Materials with the global CB minimum at  $\mathbf{k} = (0, 0, 0)$  coinciding with the VB maximum are called *direct* semiconductors, as opposed to *indirect* semiconductors. The photon emission efficiency in direct semiconductors is much better than in indirect semiconductors.

### 1.1.2 Quantum wells, wires and dots

As we have seen in the last section, the quantum mechanical description of the microscopic structure of crystals enables to explain the optical properties of bulk materials in terms of their electronic structure. Nevertheless, until the beginning of 1970s quantization effects were experimentally accessible only on isolated particles and atoms. At the same time semiconductor devices were mostly fabricated from bulk materials. The development of sophisticated crystal-growth techniques such as molecular beam epitaxy (MBE) [Cho 71] and metallic-organic vapor phase epitaxy (MOVPE) marked the beginning of a new era in solid state physics. It became possible to sandwich a very thin layer of semiconductor between two layers of another semiconductor with a higher bandgap. Such a quasi-two-dimensional structure has been named quantum well (QW) since quantum effects become apparent as the thickness of the sandwiched layer becomes close to the de Broglie length of the electron. The discovery of quantum effects related to the reduced dimensionality attracted many scientist to the study of *quantum nanostructures*, resulting in the achievement of further electron confinement to one- (quantum wires or QWR) and zero-dimensional (quantum dots or QD) systems. In QWs, QWRs and QDs the energy dispersion is strongly modified as compared to the band structure of a bulk semiconductor given in Eq. (1.7)

For any of these geometries, the energy of a single CB electron can be calculated by extending the EMA to the envelope function approximation. This yields expressions of the electron wave function as products of Bloch-functions and the envelope functions  $\Phi(\mathbf{r})$  for the confined directions or plane waves for the non-confined ones. The envelope wave functions  $\Phi(\mathbf{r})$  is the solution of the Schrödinger equation [Bast 92]

$$\left( -\frac{\hbar^2}{2} \nabla_{\mathbf{r}} \frac{1}{m^*(\mathbf{r})} \nabla_{\mathbf{r}} + V(\mathbf{r}) \right) \Phi(\mathbf{r}) = E \Phi(\mathbf{r}). \quad (1.9)$$

where the potential  $V(\mathbf{r})$  models the quantum confinement. Assuming infinitely deep rectangular confinement, it is possible to analytically calculate the carrier energies as a function of the lateral confinement  $L_i$  ( $i = x, y, z$ ). The dispersions for the two-dimensional (2D), 1D and 0D cases are

$$E_l^{2D}(k_x, k_y) = \frac{\hbar^2 \pi^2}{2m^*} \frac{l^2}{L_z^2} + \frac{\hbar^2}{2m^*} (k_x^2 + k_y^2), \quad (1.10a)$$

$$E_{lm}^{1D}(k_x) = \frac{\hbar^2 \pi^2}{2m^*} \left( \frac{l^2}{L_z^2} + \frac{m^2}{L_y^2} \right) + \frac{\hbar^2 k_x^2}{2m^*}, \quad (1.10b)$$

$$E_{lmn}^{0D} = \frac{\hbar^2 \pi^2}{2m^*} \left( \frac{l^2}{L_z^2} + \frac{m^2}{L_y^2} + \frac{n^2}{L_x^2} \right). \quad (1.10c)$$

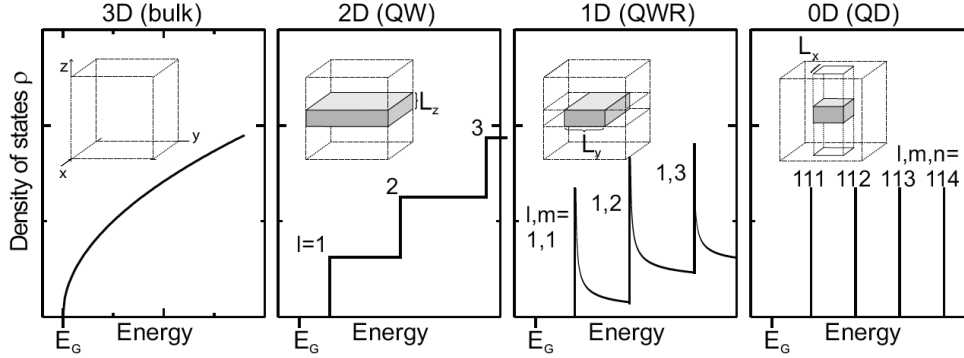


Figure 1.2: Density of states  $\rho(E)$  for a bulk semiconductor and for semiconductor heterostructures of decreasing dimensionality.

These equations show that 2D and 1D energy bands are superposed to quantized energy levels in the case of QWs and QWRs respectively, while the QD spectrum is fully quantized. For this reason, QDs are also called *artificial atoms*. Based on (1.10) it is possible to calculate the number of available states per volume and energy unit, namely the density of states (DOS)  $\rho(E)$ , for the 3D, 2D, 1D and 0D case as a function of the electron energy  $E$

$$\rho_{3D}(E) = \left( \frac{\hbar^2}{2m^*} \right)^{-3/2} \frac{E^{1/2}}{2\pi^2}, \quad (1.11a)$$

$$\rho_{2D}(E) = \left( \frac{\hbar^2}{m^*} \right)^{-1} \frac{1}{\pi L_z} \sum_l \Theta(E - E_l^{2D}(0,0)), \quad (1.11b)$$

$$\rho_{1D}(E) = \left( \frac{\hbar^2}{2m^*} \right)^{-1/2} \frac{1}{\pi L_z L_y} \sum_{lm} (E - E_{lm}^{1D}(0))^{-1/2}, \quad (1.11c)$$

$$\rho_{0D}(E) = \frac{2}{L_z L_y L_x} \sum_{lmn} \delta(E - E_{lmn}^{0D}), \quad (1.11d)$$

where  $\Theta(E)$  is the Heaviside step function and  $\delta(E)$  the Dirac distribution. Spin degeneracy is included and the resulting curves are schematically plotted in Fig. 1.2 as a function of  $E$ . Again, this figure shows the discrete character of the energy structure of QD electrons.

In Sec. 1.2 we describe the model adopted throughout this thesis for the carrier wave functions in a QD and derive the envelope wave functions for the carriers confined in a many-QD system. In particular, we consider either random planar distributions of QDs or vertically stacked quantum dots. These are typical geometries of self-organized QDs, as shown in Sec. 1.1.4.

### 1.1.3 Wannier excitons in semiconductors

In Sec. 1.1.1, we have solved the Schrödinger equation for the electron in a crystal in the mean field approximation and derived the band structure of the crystal in the effective mass approximation. In this framework, we have shown that an empty electron state in the valence band can be described in terms of a positively charged quasiparticle that we call hole. In the Hartree-Fock (HF) approximation the first excited state of the crystal is assumed to be a free electron-hole pair state. The actual excited state is instead the *exciton* state, in which electron-hole Coulomb correlation is taken into account. Properly speaking, using the solutions of Eq. (1.1), the electron-hole pair state is given by the Slater determinant

$$\Phi_{c\mathbf{k}'+\mathbf{k}_{ex},v\mathbf{k}'}(\mathbf{r}_1, \dots, \mathbf{r}_N) = \frac{1}{\sqrt{N!}} \text{Det} \{ \phi_{\mathbf{k}_1}^v(\mathbf{r}_1) \dots \phi_{\mathbf{k}'+\mathbf{k}_{ex}}^c(\mathbf{r}') \dots \phi_{\mathbf{k}_N}^v(\mathbf{r}_N) \} , \quad (1.12)$$

where  $N$  is the total number of electrons in the crystal and we are assuming the two-band approximation, that consists in restrict to the topmost valence band and the lowest conduction band states. In the state (1.12) all the electrons are in the valence band, except one that has been promoted from the valence state  $\phi_{\mathbf{k}'}^v(\mathbf{r}')$  to the conduction state  $\phi_{\mathbf{k}'+\mathbf{k}_{ex}}^c(\mathbf{r}')$ . The state has total wave vector  $\mathbf{k}_{ex}$  and energy  $E_0 - E_v(\mathbf{k}') + E_c(\mathbf{k}' + \mathbf{k}_{ex})$ , being  $E_0$  the energy of the crystal ground state that has all the electrons in the valence band and total wave vector equal to zero. The HF state (1.12) is not a good first excited state, because the potential  $U(\mathbf{r})$  appearing in Eq. (1.1) is constructed in a self consistent way by minimizing the expectation value of the full Hamiltonian of the system  $\hat{H}_0$  (i.e., describing the Coulomb interacting electrons and nuclei) over the ground state. When an electron is promoted to the conduction band, the total charge density is modified with respect to the ground state and, consequently, the state (1.12) can be considered only as the zero-order approximation of the first excited state. The first order state is obtained as a linear combination of Slater determinants of the kind of (1.12)

$$\Phi_{ex} = \sum_{\mathbf{k}'} A(\mathbf{k}') \Phi_{c\mathbf{k}'+\mathbf{k}_{ex},v\mathbf{k}'} . \quad (1.13)$$

The coefficient  $A(\mathbf{k}')$  can be interpreted as the Fourier transform of a wave function of the excited state in real space, i.e.  $F(\mathbf{r}) = \sum_{\mathbf{k}'} A(\mathbf{k}') \exp(i\mathbf{k}' \cdot \mathbf{r})$ . These coefficients are chosen by minimizing the expectation value of  $\hat{H}_0$  on the states (1.12) and imposing the normalization of (1.12), that writes  $\sum_{\mathbf{k}'} |A(\mathbf{k}')|^2 = 1$ . In the Wannier model, or *weakly bound* exciton, one assume that the exciton wave function extends over a region much larger than the lattice period or, equivalently,  $A(\mathbf{k}')$  involves only a small range

of  $\mathbf{k}'$  around zero. Then, the single particle states have the explicit form given in Eq. (1.2), and the energy bands have a parabolic dispersion as in Eq. (1.7). Furthermore, one neglects the electron-hole exchange interaction (for a consistent analysis of the short range exchange interaction see Sec. 1.3 and Appendix A). Using these approximations, an integral equation for the coefficients  $A(\mathbf{k}')$  is obtained. The Fourier transform of this integral equation in the variable  $\mathbf{k}'$  gives a differential equation for  $F(\mathbf{r})$ , that reads

$$\left( -\frac{\hbar^2 \nabla^2}{2\mu_{ex}} - \frac{e^2}{\epsilon_\infty r} \right) F(\mathbf{r}) = (E - E_g) F(\mathbf{r}). \quad (1.14)$$

that provides a simple description of the exciton states in terms of a hydrogen-like atom with reduced mass  $1/\mu_{ex} = 1/m_e + 1/m_h$  in a polarizable medium. The background dielectric constant  $\epsilon_\infty$  exactly accounts for the screening effect of all the electron states belonging to the energy bands that have been neglected in the two-band approximation as well as for the coupling to the lattice vibrations [Kohn 58, Knox 63, Sham 66]. The effective Rydberg of the exciton problem (i.e. the binding energy  $E_B^{ex}$  of the lowest exciton state) is

$$E_B^{ex} = \frac{\mu_{ex} e^4}{2\epsilon_\infty^2 \hbar^2} = 13.6 \frac{\mu_{ex}}{m} \frac{1}{\epsilon_\infty^2} \text{ eV}. \quad (1.15)$$

Typically in semiconductors  $\epsilon_\infty \approx 10$  and  $\mu_{ex}/m \approx 0.1$  and thus the binding energy is of the order of a few meV. The effective Bohr radius of the ground exciton state is

$$a_{ex} = \frac{\hbar \epsilon_\infty}{\mu_{ex} e^2} = a_B \frac{m}{\mu_{ex}} \epsilon_\infty, \quad (1.16)$$

so that the exciton wave function can extend over several thousand unit cells in semiconductors.

A similar derivation of the Wannier exciton can be done in QW and QWR structures, resulting in an hydrogen-like particle as in the case of the exciton in bulk. In the case of an ideal 2D crystal, the binding energy of the ground exciton state is four times larger than in the corresponding bulk crystal, while it is infinite in the 1D case. Nevertheless the correction due to the finite size of the crystal in the directions of the quantum confinement, results in a slightly smaller binding energy for the QW exciton with respect to the ideal 2D case and in a finite one for the QWR exciton.

In QDs the exciton picture is completely different. The electron energy levels are fully quantized, and the quantum confinement effect typically dominates over the Coulomb correlation. Electron-hole pair states are strongly confined in the volume of the dot, and the Coulomb correlation induces only an energy shift of the ground exciton energy and a moderate quantitative change in the probability amplitude of the ground exciton optical

transition [Stie 99, Zimm 02]. On the other hand, the existence of bound biexciton states can be explained only in terms of Coulomb correlation. It is not possible to construct a biexciton state from only two exciton states. Decreasing the QD size, the biexciton complex changes from bonding to antibonding. This is attributed in particular to the decreasing of the number of localized excited states which quenches the impact of correlation and exchange [Rodt 03]. In order to calculate the biexciton states, the full diagonalization of the Coulomb interaction is in principle required.

#### 1.1.4 Quantum dot fabrication. Self-assembling

QD structures can be fabricated using several methods. In the early 1980s, the nano patterning of a QW was considered to be the most straightforward way to fabricate a QD. Here, one speaks of a *top-down* approach. For direct lateral patterning the most developed approaches are electron beam lithography [Howa 85], focused ion beam lithography [Komu 83] and nanoimprint lithography [Krau 97]. Depending on the resolution of the particular lithographic technique used, QDs of arbitrary lateral shape, size and arrangement can be realized providing many degree of freedoms for the QD study. However these structures suffer from interface damage caused by the patterning procedure that is strongly detrimental for the QD optical properties. Another possibility is to use a *bottom-up* approach. The direct formation of QDs on patterned substrates as V-grooves or corrugated surfaces has been demonstrated to provide structures with good optical properties [Kapo 87, Lebe 90]. These structures can be interesting as they permit the deterministic positioning of the QDs in the desired sample region (of interest for the study and application of single QDs), but don't allow the achievement of high dot densities that would be required for conventional applications as in lasers, optical amplifiers or superluminescent diodes. This requirement is accomplished by the most investigated and widely used growth-technique, the *self-assembled growth*, exploiting the self-organization of 3D strained islands generated in lattice-mismatched materials.

Self-organized growth of quantum dots has been successfully demonstrated using both molecular beam epitaxy (MBE) [Gold 85, Berg 88, Mo 90, Gran 93, Nabe 94] and metalorganic vapor phase epitaxy (MOVPE) [Carl 94, Notz 94]. For a lattice-mismatched system with small interface energy such as InAs/GaAs, initial growth may occur layer by layer mostly by adapting the lattice parameter of the deposited material. With increasing thickness the accumulated elastic energy increases until, reached a critical thickness, the 2D layer can release its energy by forming isolated islands in which the strain is relaxed. The nature of this process was already well known for a long time and is

named Stranski-Krastanow (SK) growth mode, after an old paper of I. N. Stranski and L. von Krastanow [Stra 37]. The QD size, shape, areal density and optical properties depend on growth parameters, such as growth temperature, growth rate and amount of InAs deposited. The phase transition from the epitaxial structure to the random arrangement of QDs relieves the strain elastically without introducing defects, which opens the door for optoelectronic device applications. The natural process of QD formation implies a statistical distribution of all the different QD properties such as size, shape, strain and material composition, which results in an inhomogeneous broadening of the DOS.

Multiple layers of QDs are used to implement devices such as laser diodes. In SK epitaxy vertical self-alignment of QDs occurs because the strain field of a dot in the first layer facilitates the growth of a second dot above it [Gold 85, Xie 95, Solo 96, Fafa 99, Fafa 00]. This happens if the GaAs spacer between the two InAs layers is thin enough, so that a residual strain field from the buried InAs island extend to the surface leaving the GaAs locally strained and possibly distorted. In this way *molecules* consisting of two or more vertically stacked QDs can be fabricated.

## 1.2 Quantum dot carrier wave functions

In this section we illustrate the model adopted in this thesis for the electron-hole pair wave functions in QD systems. We assume elliptical dots lying on the  $(x, y)$ -plane, as illustrated in Fig. 1.3.(a). Here, the semimajor and the semiminor axes of the ellipse are  $\varrho_x$  and  $\varrho_y$  respectively and  $a$  is the distance of each focus from the center of the ellipse. The anisotropy of an ellipse can be quantified by means of a parameter, the *eccentricity*, that is defined as the ratio  $e = a/\varrho_x$  and whose values vary in the interval  $]0, 1[$ . The circular symmetry is recovered in the limit  $e = 0$ . The height of the QD in the  $z$ -direction is  $h$ , and a small aspect ratio  $h/\varrho_y$  (and  $h/\varrho_x$ ) is always assumed, as occurring for most real QD systems [Grun 95, Bona 98, Hart 00, Li 03, Baie 04]. Moreover, two geometries of the many-QD system are considered in the following chapters. In Chapter 2 we address random planar  $(x, y)$  distributions of QDs, whose average interdot (center to center) distance  $R$  is significantly larger than  $\varrho_x, \varrho_y$ . In Chapters 3 and 4 we consider vertically stacked QDs with vertical separation comparable to  $h$ , as shown in Fig. 1.3.(b) in the case of two QDs. As we have seen in Sec. 1.1.4, these are two typical geometries for monolayers and multilayers of self assembled QDs such as Stranski-Krastanow grown InAs/GaAs QDs. Let us focus on the vertically stacked QD geometry for the moment. The choice of the cartesian

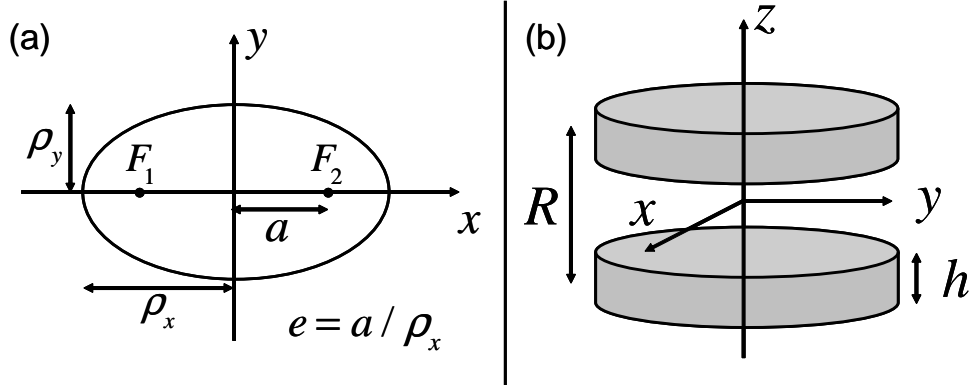


Figure 1.3: (a)  $(x, y)$ -projection of a QD.  $\rho_x$  and  $\rho_y$  are the semimajor and semiminor axis of the ellipse respectively, and  $a$  is the semi-distance between the foci. The eccentricity of the ellipse is  $e = a / \rho_x$ . (b) Schematic diagram of two vertically stacked QDs.  $h$  is the height of each QD along the  $z$ -direction and  $R$  is the distance between the two QDs.

coordinate system is such that the  $x$  and  $y$  axes coincide with the axes of the ellipse as in Fig. 1.3.(a). We assume electron-hole pair wave functions which are factored in their electron and hole part as

$$\Psi(\mathbf{r}_e, \mathbf{r}_h) = \Phi^e(\mathbf{r}_e) \Phi^h(\mathbf{r}_h), \quad (1.17)$$

thus neglecting for the moment the electron-hole Coulomb correlation. Here we are implicitly using the two-band approximation. We assume that the topmost valence states are heavy hole states which is typical for GaAs type materials. States (1.17) can be used as a basis for diagonalizing the Coulomb interaction and thus obtain exciton and biexciton states. In this way the Coulomb correlation is taken into account. For a strongly confined single QD, the Coulomb correlation induces only a moderate quantitative change in the probability amplitude of the ground exciton optical transition [Stie 99, Zimm 02]. This quantitative effect can be accounted for by adjusting the interband matrix element in order to reproduce e.g. the single-QD radiative recombination rate, while the factored states (1.17) are a good approximation for the exciton wave function. On the other hand, the existence of bound biexciton states can be explained only in terms of Coulomb correlation. It is not possible to construct a biexciton state from only two exciton states. In fact, the matrix element of the Coulomb interaction between the latter results in a positive contribution to the energy, that is, to an unbound four particle state [Rodt 03]. In order to calculate the biexciton states, the full

diagonalization of the Coulomb interaction is in principle required. Nevertheless, in this thesis we are not interested to provide a complete description of the biexciton states, that will enter in our models only through their energy eigenvalue and dipole matrix element. For these reasons, we will use exciton and biexciton states that are calculated by diagonalizing the Coulomb interaction over a few electron-hole pair states. The carrier (electron or hole) wave functions  $\Phi^c(\mathbf{r})$  in Eq. (1.17), are the eigenvectors of the Hamiltonian

$$\hat{H} = -\frac{\hbar^2}{2} \nabla_{\mathbf{r}} \frac{1}{m_c(\mathbf{r})} \nabla_{\mathbf{r}} + V_c(\mathbf{r}), \quad (1.18)$$

describing the motion of a particle with position-dependent effective mass  $m_c(\mathbf{r})$ , in a potential  $V_c(\mathbf{r})$  that models the band profile of the QD system. We assume that the problem is separable in its in-plane and  $z$ -components, namely the confinement potential can be written as

$$V_c(\mathbf{r}) = V_c^0(\mathbf{r}) + V_c^1(\mathbf{r}), \quad (1.19a)$$

$$V_c^0(\mathbf{r}) = U_c(\boldsymbol{\rho}) + W_c(z), \quad (1.19b)$$

$$V_1(\mathbf{r}) = V_c(\mathbf{r}) - U_c(\boldsymbol{\rho}) - W_c(z), \quad (1.19c)$$

where  $U_c(\boldsymbol{\rho})$  is a single-well potential in the  $(x, y)$ -plane,  $W_c(z)$  a multiple-well potential in the  $z$ -direction, each dip corresponding to a QD, and  $V_1(\mathbf{r})$  is a perturbation potential, whose contribution to the energy of the confined state we neglect.  $V_c(\mathbf{r})$ ,  $U_c(\boldsymbol{\rho})$ ,  $W_c(z)$  and  $V_1(\mathbf{r})$  are schematically represented in Fig. 1.4. The consequence of the separation of variables is that the carrier wave function is also separated as

$$\Phi_{\nu}^c(\mathbf{r}) = \phi^c(\boldsymbol{\rho}) h_{\nu}^c(z), \quad (1.20)$$

and its  $(x, y)$ -projection  $\phi^c(\boldsymbol{\rho})$  is the same for all values of  $z$ . In Eq. (1.20),  $\nu$  is the energy quantum number. We have evaluated, at the first order of perturbation, the error introduced by neglecting  $V_c^1(\mathbf{r})$ . This error is less than 1% for the confined functions, that is negligible also considering the other approximations made.

It is known that, in strong confinement regime, the exciton wave function in a many-QD system is localized in one of the dots, as long as the QDs are sufficiently far apart. This condition is fulfilled in the case of the planar distribution of QDs considered in Chapter 2, but not in the case of vertically stacked QDs considered in Chapters 3 and 4. In this case, the overlap of the  $z$ -component of the carrier wave functions results in electron tunneling, that plays a key role in the interaction mechanisms considered. In both cases, the in-plane projection of the carrier wave function  $\phi^c(\boldsymbol{\rho})$  is assumed

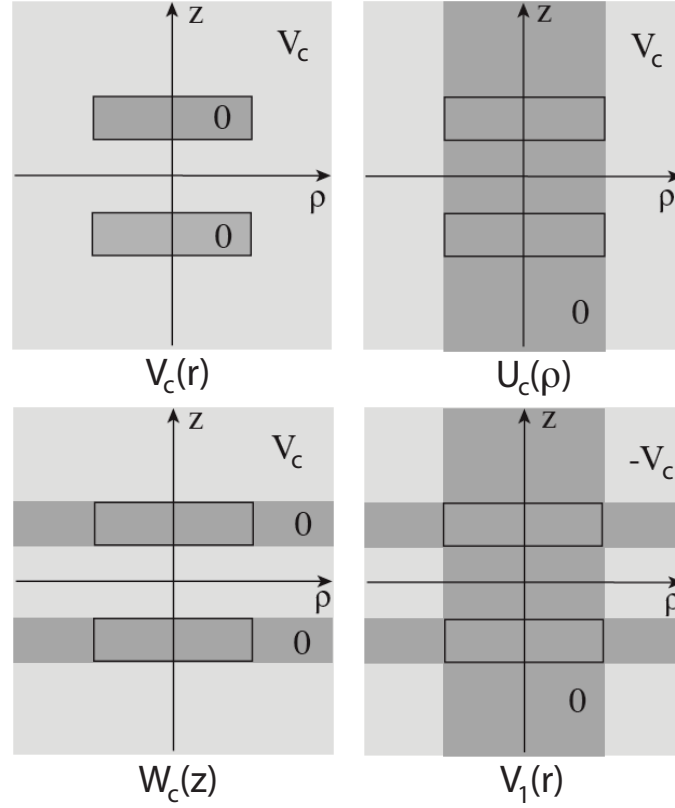


Figure 1.4: Schematic representation of the potentials  $V_c(\mathbf{r})$ ,  $U_c(\boldsymbol{\rho})$ ,  $W_c(z)$  and  $V_1(\mathbf{r})$  defined in Eq. (1.19).

as being completely localized in a single potential dip, and can be calculated by considering the QD centered at  $(x, y) = (0, 0)$ . In the case of the planar distribution of QDs, if  $\mathbf{R}_\alpha$  is the position of the  $\alpha$ -th dot in the chosen coordinate frame, the in-plane carrier wave function is then obtained via a rigid shift as

$$\zeta_\alpha^c(\boldsymbol{\rho}) = \phi^c(\boldsymbol{\rho} - \mathbf{R}_\alpha). \quad (1.21)$$

As we consider QDs with a small aspect ratio, the energy spacing between the in-plane carrier states is expected to be much smaller than that between the  $z$  states. Nevertheless, in the following chapters we will always consider only the  $N$  lower electron and hole energy states for systems of  $N$  vertically stacked QDs. It is easy to demonstrate that, in this geometry, the lower  $N$  states differ from each other for their  $z$ -component, having the same ground-state  $(x, y)$ -projection  $\phi^c(\boldsymbol{\rho})$ . Given the confining potential  $U_c(\boldsymbol{\rho})$ ,  $\phi^c(\boldsymbol{\rho})$  is a first kind Bessel function in the QD, while outside of the QD decays expo-

nentially as a first kind Hankel function with imaginary argument [Para 05]. Nevertheless, we assume for  $\phi^c(\boldsymbol{\rho})$  a gaussian shape [Mulj 05] resulting from a parabolic confining potential and from setting  $m_c(\boldsymbol{\rho}) = m_c$ , that well approximate the real ground state in-plane wave function. This assumption will allow in the following to carry out many calculations analytically. Then, we can write the in-plane carrier wave function as

$$\phi^c(\boldsymbol{\rho}) = f^c(x)f^c(y), \quad (1.22)$$

whose normalized  $x$ - and  $y$ -component read

$$f^c(s) = \frac{1}{(\pi\sigma_{cs}^2)^{1/4}} \exp(-s^2/2\sigma_{cs}^2), \quad (1.23)$$

being  $\sigma_{cs}$  the standard deviation of the Gauss function. The energy of the quantum state associated to the confinement is given by the expectation value of the total hamiltonian (1.18) on the electron-hole pair wave function  $\Psi(\mathbf{r}_e, \mathbf{r}_h)$ . As an example, taking into account only the kinetic Hamiltonian

$$\hat{H} = - \sum_{c=e,h} \frac{\hbar^2}{2m_c} \nabla_{\mathbf{r}_c}^2, \quad (1.24)$$

the analytical expression for the kinetic term is

$$\langle \Psi(\mathbf{r}_e, \mathbf{r}_h) | \hat{H}_k | \Psi(\mathbf{r}_e, \mathbf{r}_h) \rangle = \varepsilon_e^0 + \varepsilon_h^0 + \Delta E(\sigma_e, \sigma_h). \quad (1.25)$$

Here  $\varepsilon_e^0$  ( $\varepsilon_h^0$ ) is the contribution to the kinetic energy coming from the motion of the electron (hole) along the  $z$  direction, and  $\Delta E(\sigma_e, \sigma_h)$  is the  $(x, y)$ -kinetic energy, whose analytical expression is

$$\Delta E(\sigma_e, \sigma_h) = \langle \phi^e(\boldsymbol{\rho}_e) \phi^h(\boldsymbol{\rho}_h) | \hat{H}_{k||} | \phi^e(\boldsymbol{\rho}_e) \phi^h(\boldsymbol{\rho}_h) \rangle = \sum_{c=e,h} \frac{\hbar^2}{4m_c\sigma_c^2}, \quad (1.26)$$

and depends on the quantity  $\sigma_c$ , given by  $\sigma_c^{-2} = \sigma_{cx}^{-2} + \sigma_{cy}^{-2}$ . In Chapter 2 we will need the Fourier transform of the in-plane electron-hole wave function  $\phi^e(\boldsymbol{\rho}_e) \phi^h(\boldsymbol{\rho}_h)$ , evaluated at  $\boldsymbol{\rho}_e = \boldsymbol{\rho}_h$ . This quantity is proportional to the dipole matrix element giving the interband transition amplitude, and reads

$$\begin{aligned} \varphi_{\mathbf{k}} &= \frac{1}{2\pi} \int d\boldsymbol{\rho} \exp(i\mathbf{k} \cdot \boldsymbol{\rho}) \phi^e(\boldsymbol{\rho}) \phi^h(\boldsymbol{\rho}) \\ &= \frac{\sigma_x \sigma_y}{\pi \sqrt{\sigma_{ex} \sigma_{ey} \sigma_{hx} \sigma_{hy}}} \exp(-k_x^2 \sigma_x^2 / 2) \exp(-k_y^2 \sigma_y^2 / 2), \end{aligned} \quad (1.27)$$

being  $\sigma_s$  defined by  $\sigma_s^{-2} = \sigma_{es}^{-2} + \sigma_{hs}^{-2}$ .

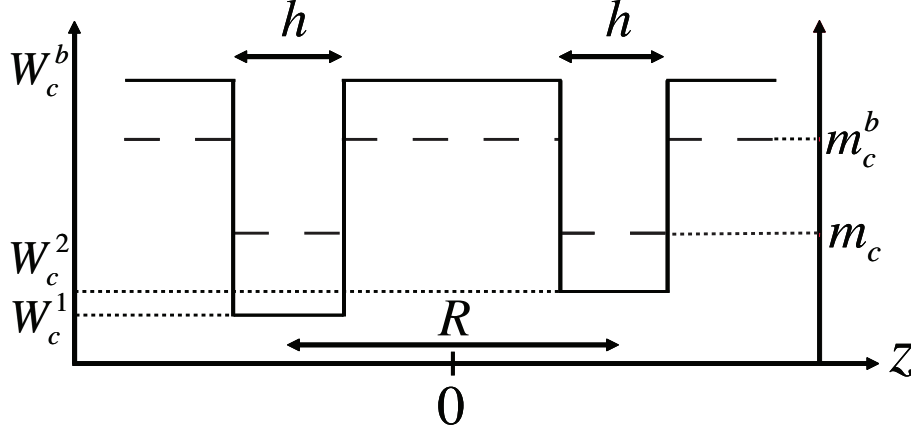


Figure 1.5: Profiles of the  $z$ -dependent confinement potential (solid line) and effective mass (dashed line) for the carrier in the two-QD system in Fig. 1.3.(b).

The  $z$ -component of the carrier wave function is calculated numerically as the eigenfunction of the effective mass Hamiltonian operator

$$\hat{H}_z = -\frac{\hbar^2}{2} \frac{d}{dz} \frac{1}{m_c(z)} \frac{d}{dz} + W_c(z). \quad (1.28)$$

The profiles of the effective mass of the carrier  $m_c(z)$  and that of the confining potential  $W_c(z)$  are shown in Fig. 1.5 in the case of two QDs. The confining potential is assumed to be a square potential that takes constant values  $W_c^b$  in the barrier and  $W_c^j$  in the  $j$ -th QD. Assuming an asymmetry between different QDs, we simulate the effect of the fluctuation of the structural properties from dot to dot [Mulj 05] that is typical of self-assembled QDs. A similar assumption of piecewise constant value is made for  $m_c(z)$ , as displayed in Fig. 1.5, in order to model different QD and barrier materials. At the interfaces  $\bar{z}$  between the QDs and the surrounding medium, the eigenfunctions of the Hamiltonian operator (1.28) must satisfy the boundary conditions

$$h_\nu^c(\bar{z}^-) = h_\nu^c(\bar{z}^+), \quad (1.29a)$$

$$\frac{1}{m_c^-} \left[ \frac{d}{dz} h_\nu^c(z) \right]_{z=\bar{z}^-} = \frac{1}{m_c^+} \left[ \frac{d}{dz} h_\nu^c(z) \right]_{z=\bar{z}^+}, \quad (1.29b)$$

being  $\bar{z}^-$  and  $\bar{z}^+$  the left and right limits of  $z$  to  $\bar{z}$  respectively and  $m_c^\pm = m_c(\bar{z}^\pm)$ . In Fig. 1.6 we plot the lowest-energy electron and hole wavefunctions resulting from the diagonalization of the Hamiltonian (1.28) in the

case of two QDs, in order to compare them in several cases. In particular, we use InAs/GaAs parameters for the two-QDs potential and for the carriers effective masses in the  $z$ -direction, namely

$$W_{e/h}(z) = \begin{cases} W_{e/h}^b = 672 \text{ meV}/288 \text{ meV}, & \text{in the barrier} \\ W_{e/h}^1 = 0, & -\frac{h+R}{2} \leq z \leq \frac{h-R}{2} \\ W_{e/h}^2 = 13.44 \text{ meV}/5.76 \text{ meV}, & \frac{h-R}{2} \leq z \leq \frac{h+R}{2} \end{cases} \quad (1.30)$$

$$m_{e/h}(z) = \begin{cases} m_{e/h}^b = 0.067m/0.327m, & \text{in the barrier} \\ m_{e/h} = 0.027m/0.265m, & \text{in the QDs} \end{cases} \quad (1.31)$$

being  $m$  the free electron mass. In Fig. 1.6.(a), the two lowest-energy electron wave functions are plotted for an interdot distance  $R = 10$  nm, small enough to obtain states that are delocalized on the whole QD system. In Fig. 1.6.(b) we compare the ground electron and hole wave functions, showing that the electron wave functions are broader than those of the hole. This is because of the smaller value of the effective mass of the electron with respect to that of the hole (see Eqs. 1.31). In Fig. 1.6.(c) we plot the two lowest-energy electron wave-functions for  $R = 30$  nm. The comparison to Fig. 1.6.(a) shows that a larger distance results in states that are strictly localized in one of the two QDs. Finally, Fig. 1.6.(d) is a detail from Fig. 1.6.(a), where we show that, according to the boundary conditions (1.29), the wave-function  $h_\nu^c(z)$  is continuous at the border coordinates  $\bar{z}$ , with a discontinuous first derivative.

## 1.3 Coulomb interaction in quantum dots

In the previous section we have calculated the electron-hole pair wave functions for our model QD system, neglecting any Coulomb correlation between the charged particles. Here, we discuss how the Coulomb interaction is included in the quantum-mechanical description of the QD system, in the envelope function approximation. The microscopic derivation of the second quantization Coulomb hamiltonian for a generic semiconductor medium is given in Appendix A.

In the second quantization formalism the few-electron and -hole states derived in Sec. 1.2 are represented by kets in a Fock space. In the following the carrier wave function will be labeled with a spin quantum number  $\sigma = \pm 1$  corresponding to electron (heavy hole) spin  $\pm 1/2$  ( $\pm 3/2$ ). In

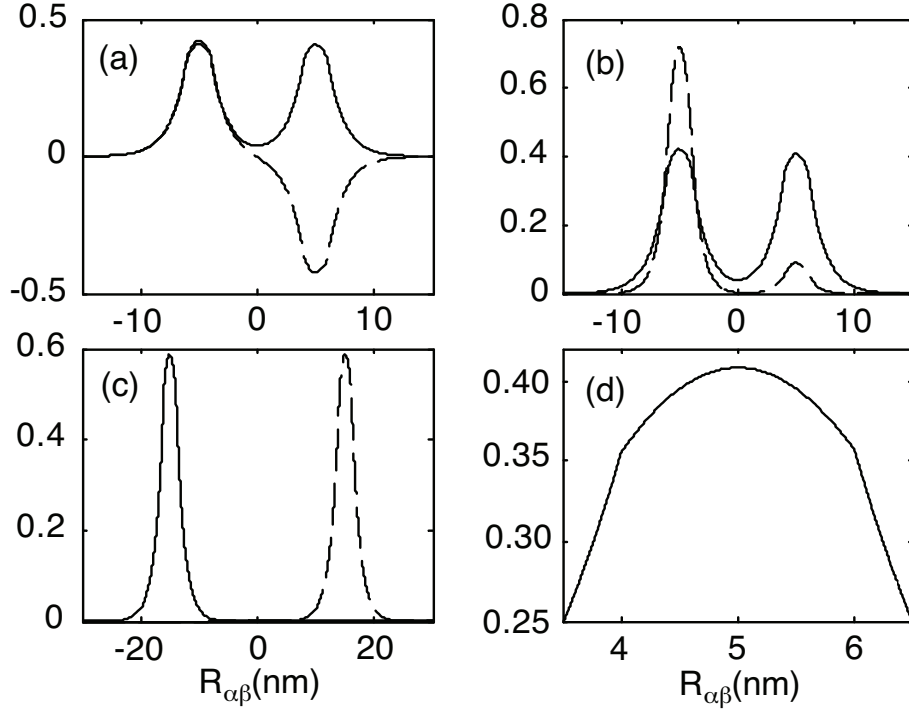


Figure 1.6: (a) wave functions of the ground (solid line) and first excited (dashed) electron states along the  $z$ -direction in a two-QD system, for an interdot distance  $R = 10$  nm. The thickness of each QD is  $h = 2$  nm, the carriers band offsets are given in Eq. (1.30) and their effective masses in Eq. (1.31). The wave functions are delocalized on the whole system. (b) comparison between the wave functions of the ground electron (solid) and hole (dashed) states, for the system in (a). The electron wave function is broader than the hole one, because of the smaller value of the effective mass. Note that both states are not symmetric with respect to  $z$ -inversion, because of the asymmetry of the confining potential (see Eq. (1.30) and Fig. 1.5). (c) The same as in (a), but for  $R = 30$  nm. (d) Magnification of (a). According to the boundary conditions (1.29), the carrier wave function is continuous at the interface between the QD and the surrounding medium, with a discontinuous first derivative.

fact, the Coulomb interaction allows spin transfer between different excitonic states. The state  $\Phi_i^e(\mathbf{r})$  ( $\Phi_i^h(\mathbf{r})$ ) of definite spin  $\sigma$  corresponds to the ket  $\hat{c}_{i\sigma}^\dagger|0\rangle$  ( $\hat{d}_{i\sigma}^\dagger|0\rangle$ ), where  $\hat{c}_{i\sigma}^\dagger$  and  $\hat{c}_{i\sigma}$  ( $\hat{d}_{i\sigma}^\dagger$  and  $\hat{d}_{i\sigma}$ ) are the electron (hole) operators, obeying Fermi commutation rules, and  $|0\rangle$  is the vacuum state in the electron-hole representation. In this notation, the Coulomb Hamiltonian

reads

$$\begin{aligned} \hat{H}_c = & \frac{1}{2} \sum_{ijlm} \sum_{\sigma\sigma'} \left( V_{ijlm}^{ee} \hat{c}_{i\sigma}^\dagger \hat{c}_{j\sigma} \hat{c}_{l\sigma'}^\dagger \hat{c}_{m\sigma'} + V_{ijlm}^{hh} \hat{d}_{i\sigma}^\dagger \hat{d}_{j\sigma} \hat{d}_{l\sigma'}^\dagger \hat{d}_{m\sigma'} \right. \\ & \left. - 2V_{ijlm}^{eh} \hat{c}_{i\sigma}^\dagger \hat{c}_{j\sigma} \hat{d}_{l\sigma'}^\dagger \hat{d}_{m\sigma'} + 2V_{ijlm,\sigma\sigma'}^{ex} \hat{c}_{i\sigma}^\dagger \hat{d}_{j\sigma} \hat{d}_{l\sigma'}^\dagger \hat{c}_{m\sigma'} \right). \end{aligned} \quad (1.32)$$

where the four terms describe the repulsion between electrons and between holes, the electron-hole attraction, and the exchange (Förster) interaction, respectively. The spin transfer mechanism is contained in the exchange term with  $\sigma = -\sigma'$ . The explicit expression of the direct and Förster Coulomb matrix elements is

$$V_{ijlm}^{cc'} = \int d\mathbf{r} d\mathbf{r}' \Phi_i^{c*}(\mathbf{r}) \Phi_j^{c*}(\mathbf{r}) \frac{e^2}{\epsilon_\infty |\mathbf{r} - \mathbf{r}'|} \Phi_l^{c'}(\mathbf{r}') \Phi_m^{c'}(\mathbf{r}'), \quad (1.33a)$$

$$V_{ijlm,\sigma\sigma'}^{ex} = \int d\mathbf{r} d\mathbf{r}' \Phi_i^{e*}(\mathbf{r}) \Phi_j^{h*}(\mathbf{r}) \frac{e^2}{\epsilon_\infty |\mathbf{r} - \mathbf{r}'|} \Phi_l^h(\mathbf{r}') \Phi_m^e(\mathbf{r}'), \quad (1.33b)$$

where  $c$  ( $c'$ ) is either  $e$  or  $h$ , and  $\epsilon_\infty$  is the background dielectric constant. In our QD model, the carrier wave function is the factored product of a  $(x, y)$ - and a  $z$ -component, according to Eq. (1.20). Then, the direct and exchange Coulomb matrix elements can be written as

$$V_{ijlm}^{cc'} = \int dz dz' h_i^{c*}(z) h_j^{c*}(z) V_C^{cc'}(z - z') h_l^{c'}(z') h_m^{c'}(z'), \quad (1.34a)$$

$$V_{ijlm,\sigma\sigma'}^{ex} = \int dz dz' h_i^{e*}(z) h_j^{h*}(z) V_F^{\sigma\sigma'}(z - z') h_l^h(z') h_m^e(z'), \quad (1.34b)$$

where the  $z$ -dependent potentials read

$$V_C^{cc'}(z) = \int d\boldsymbol{\rho} d\boldsymbol{\rho}' |\phi^c(\boldsymbol{\rho})|^2 W_C^{cc'}(\boldsymbol{\rho} - \boldsymbol{\rho}', z) |\phi^{c'}(\boldsymbol{\rho}')|^2, \quad (1.35a)$$

$$V_F^{\sigma\sigma'}(z) = \int d\boldsymbol{\rho} d\boldsymbol{\rho}' \phi^e(\boldsymbol{\rho}) \phi^h(\boldsymbol{\rho}) W_F^{\sigma\sigma'}(\boldsymbol{\rho} - \boldsymbol{\rho}', z) \phi^e(\boldsymbol{\rho}') \phi^h(\boldsymbol{\rho}'). \quad (1.35b)$$

Here,  $W_C^{cc'}(\mathbf{R} \equiv (\boldsymbol{\rho}, z))$  is the sum of the leading term of the multipole expansion of the direct Coulomb potential  $W_C^0(\mathbf{R}) \propto 1/R$ , and of the correction  $\Delta W_C^{cc'}(\mathbf{R}) \propto 1/R^3$ . These two terms are explicitly calculated in Appendix A and their expression are given in Eq. (A.11) and Eq. (A.12), respectively. In the Förster potential the leading term is  $W_F^{\sigma\sigma'}(\mathbf{R}) \propto 1/R^3$  because the term of order  $1/R$  vanishes (see discussion in Appendix A). The explicit expression of  $W_F^{\sigma\sigma'}(\mathbf{R})$  for  $\sigma = \sigma'$  or  $\sigma = -\sigma'$  is given in Eq. (A.22) and in (A.23), respectively. Then, the correction  $\Delta W_C^{cc'}$  to the direct Coulomb potential is

of the same order of the Förster potential and must be taken into account for consistence. Using the in-plane gaussian wave functions given in Eq. (1.22) and Eq. (1.23), the two contributions to the direct  $z$ -potential become

$$V_{C0}(z) = \Lambda \int d\theta \frac{\eta[a(\theta)|z|]}{a(\theta)}, \quad \text{with} \quad \Lambda = \frac{e^2}{\pi \epsilon_\infty \bar{\sigma}_x \bar{\sigma}_y} \quad (1.36)$$

$$\Delta V_C^{cc'}(z) = \xi^{cc'} \Lambda \int d\theta \left[ a(\theta) \left[ \frac{1}{2} + a^2(\theta) z^2 \right] \eta[a(\theta)|z|] - a^2(\theta) z^2 \right] \quad (1.37)$$

where  $\bar{\sigma}_s^2 = \sigma_{es}^2 + \sigma_{hs}^2$ ,  $a^2(\theta) = \cos^2 \theta / \bar{\sigma}_x^2 + \sin^2 \theta / \bar{\sigma}_y^2$ ,  $\xi^{cc'}$  is defined in Eq. (A.24) and  $\eta(x) = 2 \exp(x^2) \int_x^\infty dt \exp(-t^2)$  is the modified error function. The spin-conserving and spin-scattering Förster potentials read instead

$$V_F^{\sigma\sigma}(z) = \mu^2 \Lambda \int d\theta \left[ b(\theta) \left[ \frac{1}{2} + b^2(\theta) z^2 \right] \eta[b(\theta)|z|] - b^2(\theta) z^2 \right] \quad (1.38a)$$

$$V_F^{\sigma-\sigma}(z) = \mu^2 \Lambda \int d\theta \exp(-2i\theta) \times \left[ b(\theta) \left[ \frac{3}{2} + b^2(\theta) z^2 \right] \eta[b(\theta)|z|] - b^2(\theta) |z| \right], \quad (1.38b)$$

where  $\mu$  is the basic dipole moment calculated in Appendix A, and we have defined  $b^2(\theta) = \cos^2 \theta / 4\sigma_x^2 + \sin^2 \theta / 4\sigma_y^2$  with  $\sigma_s^{-2} = \sigma_{es}^{-2} + \sigma_{hs}^{-2}$ . Note the similarity between Eqs. (1.37) and (1.38a) (see Eq. (A.25) and the following discussion). For an isotropic QD with  $\sigma_{e/hx} = \sigma_{e/hy} \equiv \sigma_{e/h}$ , the  $\theta$  dependence in Eqs. (1.36), (1.37) and (1.38) can be integrated analytically, resulting in the following simplified expressions for the  $z$ -potentials

$$V_C(z) = \frac{e^2}{\epsilon_\infty \bar{\sigma}} \eta(|z|/\bar{\sigma}), \quad (1.39a)$$

$$\Delta V_C^{cc'}(z) = \frac{e^2 \xi^{cc'}}{\epsilon_\infty \bar{\sigma}^3} \chi(|z|/\bar{\sigma}), \quad (1.39b)$$

$$V_F(z) = \frac{e^2 \mu^2}{\epsilon_\infty \bar{\sigma}^2 \sigma} \chi(|z|/\sigma), \quad (1.39c)$$

with  $\bar{\sigma}^2 = \sigma_e^2 + \sigma_h^2$ ,  $\sigma^{-2} = (\sigma_e^{-2} + \sigma_h^{-2})/4$  and  $\chi(x) = \eta''(2) = (2x^2 + 1)\eta(x) - 2x$ . The Förster potential in Eq. (1.39c) is the spin-conserving component, while the spin-scattering component is zero. Then, in two-dimensional isotropic systems the two orthogonally polarized exciton states are degenerate, as we will explain in detail in Sec. 2.3.1. For equal in-plane confinement of electron and hole,  $\sigma_e = \sigma_h$ , we have  $\bar{\sigma} = \sigma$  and, assuming the approximation (A.26), get identical values for the Förster potential and electron-hole Coulomb correction in the  $z$ -direction.

## Chapter 2

# Long-range radiative coupling between semiconductor QDs

Physical phenomena based on reduced dimensionality have been one of the main subjects of research in condensed matter physics in the last three decades. As we have seen in Chapter 1, quantum confinement at nanoscale gives rise to electronic-states whose energy levels are discrete. This resulted in an atom-like picture of QDs, where electronic states are expected to be strongly isolated from the environment and to show long coherence-times, an essential feature for applications in many fields (e.g. quantum information technology [Burk 99]). Nevertheless, experiments demonstrate that interaction mechanisms, whose relevance increases dramatically with increasing the extension of the quantum system, are still cause of decoherence. These mechanisms can be grouped into two classes. In a first class, the interaction occurs via overlapping wave functions. In simpler terms, when two confined systems are brought sufficiently close, the electronic states are extended over the two parts, effectively corresponding to the situation of a confined system of larger extension. As an example, in Fig. 1.6 we have shown that the carrier wave function in a many QD system is localized in one of the dots as long as they are far apart, while it is delocalized over the whole QD system if the dots are sufficiently close in space. To a larger system correspond more closely spaced energy levels and more efficient inelastic scattering mechanisms mediated by a thermal bath, thus increasing the decoherence rate. An example is the acoustic-phonon dephasing in QD molecules, described in Chapter 3.

Interaction between polarizable systems can also occur without tunneling. In this case, one speaks of *excitation transfer mechanisms*. The prototype of this class of mechanisms is the electrostatic dipole-dipole interaction, known as Förster Resonant Energy Transfer (FRET) [Fors 65, Govo 03]. This mechanism has a key role in many biological processes, such as the transfer of

excitation from an excited donor molecule to an acceptor molecule [Kuri 88] or in the photosynthesis [Oppe 41, Van 94]. In semiconductors, the Förster mechanism corresponds to the so-called electron-hole *exchange* part of the electrostatic Coulomb interaction [Bass 75]. Within a two-band Hartree-Fock model of the exciton, this effect corresponds to the direct (Hartree) Coulomb interaction in the conduction-valence-band picture, whereas the conduction-valence exchange term (Fock) gives the direct electron-hole electrostatic interaction responsible of the excitonic Rydberg [Bass 75]. Within the envelope-function approximation, the Förster potential is expressed by the dipole-dipole coupling

$$W_F(\mathbf{R}) = \frac{R^2 |\mu_{cv}|^2 - 3 |\mathbf{R} \cdot \boldsymbol{\mu}_{cv}|^2}{\epsilon_\infty R^5}, \quad (2.1)$$

where  $\epsilon_\infty$  is the background dielectric constant,  $\mathbf{R}$  is the distance between the two dipoles and

$$\boldsymbol{\mu}_{cv} = e \int d\mathbf{r} w_c^*(\mathbf{r}) \mathbf{r} w_v(\mathbf{r}), \quad (2.2)$$

is the dipole matrix element of the interband optical transition, here expressed in terms of the conduction and valence Wannier functions  $w_{c/v}(\mathbf{r})$ . In Eq. (2.2),  $e$  is the electron charge, and the integral is extended to the elementary cell volume. Eqs. (2.1) and (2.2) are derived in Appendix A. The dipole-dipole potential in Eq. (2.1) decays versus distance as  $R^{-3}$ . Moreover, FRET is a strongly resonant mechanism. The probability of a transition from an initial state  $|n\rangle$  to any accessible final state  $|m\rangle$  is given by the Fermi golden rule

$$W_n = \frac{2\pi}{\hbar} \sum_m |\langle n | V_F | m \rangle|^2 \delta(E_n - E_m). \quad (2.3)$$

The electrostatic FRET is contained in the instantaneous limit  $c \rightarrow \infty$  of a full Maxwell-Schrödinger description of light-matter interaction [Andr 90, Andr 94]. The eigenmodes of the Maxwell equations coupled to the polarization field of a semiconductor structure are the exciton-polaritons. Bulk exciton-polaritons are mixed modes of one exciton and one photon mode having the same momentum, as imposed by translational invariance [Hopf 58]. This one-to-one selection rule results into a strong mixing and an energy-dispersion that displays the anticrossing typical of normal-mode coupling [Andr 94]. In GaAs, the normal-mode splitting at resonance is 16 meV, larger than the exciton binding energy. In systems with reduced dimensionality, such as quantum wells and quantum wires, the partial breaking of the translational symmetry allows coupling of excitons to a continuum

of photon modes, and the polariton becomes a resonance of a discrete exciton state linearly coupled to a photon continuum, analogously to a Fano resonance [Fano 61]. In this case the importance of the coupling, expressed by the magnitude of the polariton self-energy correction to the bare exciton energy, is considerably smaller [Tass 90, Citr 92, Citr 93a, Citr 93b, Jord 93, Andr 94, Jord 94, Tass 95]. When the dimensionality of the electromagnetic field is also reduced, e.g. in semiconductor planar microcavities, the one-to-one coupling typical of a bulk semiconductor is recovered and strongly-coupled polaritons with full exciton-photon mixing characterize the optical spectrum [Weis 92, Houd 94, Savo 95, Savo 96].

In the case of a QD, where the electron-hole system is fully confined in the three spatial directions, it is already established [Bock 93, Citr 93b, Gil 02] that the coupling to the electromagnetic field results in a finite probability of recombining via emission of one photon. In presence of more than one QD, the emitted photon can propagate and eventually be absorbed by another QD, resulting in an excitation transfer process. Since the emitted photon propagates as a spherical wave, the transfer probability amplitude is expected to vary as  $R^{-1}$  as a function of the QD distance  $R$ , in the limit  $R \rightarrow \infty$ . However, this radiative mechanism must describe also the FRET in the electrostatic limit of instantaneous light propagation,  $c \rightarrow \infty$ . We thus expect the radiative transfer to be a small correction to FRET for small  $R$  and to dominate over FRET at larger  $R$  where FRET depends on  $R^{-3}$ .

In this chapter we develop a theory for the radiative coupling between QDs distributed on a plane, embedded in a homogeneous bulk semiconductor medium. We solve the Maxwell equations for the electromagnetic field coupled to the interband polarization field of the QD ensemble and compute the polariton resonances of the system. In the resulting analytical expression for the probability amplitude of the transfer process, the instantaneous Förster term and the retarded correction are well distinguished. They decay as  $R^{-3}$  and  $R^{-1}$  respectively. In the instantaneous limit ( $c \rightarrow \infty$ ) we recover the pure  $R^{-3}$  FRET. The collective modes of the coupled QD system display modified radiative lifetimes, some of them being strongly *sub-radiant* or *super-radiant* with respect to the bare QDs lifetime.

The chapter is organized as follows. In Sec. 2.1, starting from the Maxwell equations and a linear non-local susceptibility tensor, we analytically derive the eigenmode equations that hold in presence of radiative coupling. In Sec. 2.2 we discuss the dependence of the interaction on the QD distance. Sec. 2.3 contains the results of the numerical diagonalization of the problem in the case of a single anisotropic dot and of two- and many-QD systems, followed by a discussion of the computed results. In Sec. 4.4 we present some concluding remarks.

## 2.1 The Maxwell-Schrödinger formalism

The semiclassical model of QD interband excitation in interaction with the electromagnetic field is based on the solution of Maxwell equations coupled to a nonlocal linear susceptibility which accounts for the interband optical transition. This is done in full analogy with the polariton formalism in bulk semiconductors and heterostructures [Tass 90, Andr 94]. In what follows, we restrict the discussion to the transition between the semiconductor ground state and the ground electron-hole pair state (i.e. the first excited state) in each QD.

### 2.1.1 The linear susceptibility tensor

The QD system under study consists in a random distribution of cylindrical dots lying on the  $(x, y)$ -plane. The QD labeled with  $\alpha$  has radius  $\varrho_\alpha$  and height  $h$ , with a small aspect ratio  $h/\varrho_\alpha$ . We are therefore treating a quasi two-dimensional system, as illustrated in Fig. 2.1 in the case of two QDs  $\alpha$  and  $\beta$ . This QD system is completely described by the linear susceptibility tensor derived from the linear response theory [Kubo 57] and calculated within the effective mass approach. In particular, we consider the electron-heavy-hole optical transition in a semiconductor with cubic lattice symmetry. In this case, in analogy with a quantum well [Savo 02], the component of the interband electron-hole polarization vector in the confinement direction  $z$  is zero. Then, only the  $x$ - and  $y$ -components are coupled to the electromagnetic field, and the susceptibility tensor reads

$$\hat{\chi}(\mathbf{r}, \mathbf{r}', \omega) = \frac{\mu_{cv}^2}{\hbar} \sum_{\alpha} \frac{\Psi_{\alpha}(\mathbf{r}, \mathbf{r}) \Psi_{\alpha}^*(\mathbf{r}', \mathbf{r}')}{\omega_{\alpha} - \omega - i0^+} \begin{pmatrix} 1 & 0 & 0 \\ 0 & 1 & 0 \\ 0 & 0 & 0 \end{pmatrix}. \quad (2.4)$$

The susceptibility is non-local in the three spatial coordinates, as expected from the breaking of translational invariance. In Eq. (2.4), the quantities  $\hbar\omega_{\alpha}$  and  $\Psi_{\alpha}(\mathbf{r}_e, \mathbf{r}_h)$  are respectively the electron-hole pair energy and wave function in the  $\alpha$ -th dot, that have been calculated in detail in Sec. 1.2. Note that in (2.4) the wave function  $\Psi_{\alpha}$  is evaluated at  $\mathbf{r}_e = \mathbf{r}_h$ , according to the effective mass theory of the interband optical transition [Andr 94]. By using simple Lorentz resonances in Eq. (2.4), we assume that the non-radiative lineshape of each QD is a Dirac delta function. As we thoroughly discuss in Chapter 3, non-perturbative coupling of the exciton with acoustic phonons is responsible for a broad phonon-assisted contribution to the non-radiative QD spectral function [Borr 01, Krum 02, Zimm 02]. However, at low temperatures the phonon sidebands tends to be small, especially for low

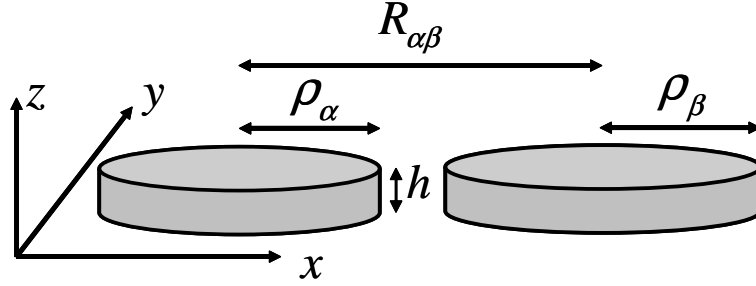


Figure 2.1: Schematic diagram of the cylindrical dot ensemble.  $h$  is the height of QD  $\alpha$  in the  $z$ -direction,  $\rho_\alpha$  its radius in the  $(x, y)$ -plane, and  $R_{\alpha\beta}$  is the distance between the two QDs.

quantum confinement. The zero-phonon line (ZPL) on the other hand is the sum of two contributions. The first comes from the finite lifetime of the carriers populations, due to both radiative and non-radiative recombination. The second is the so called *pure dephasing*, that is the loss of coherence of the polarization without a corresponding decrease of populations, whose nature is still debated. Nevertheless, it has been recently shown that the dephasing time is dominated by the radiative lifetime at low temperature [Lang 04b]. This is also an outcome of the present approach, as we show in the following.

### 2.1.2 The scattering approach

The Maxwell equation for the electric field  $\mathcal{E}$ , expressed in the space and frequency domain, can be written as

$$\begin{aligned} \nabla \wedge \nabla \wedge \mathcal{E}(\boldsymbol{\rho}, z, \omega) - \frac{\omega^2}{c^2} [\epsilon_\infty \mathcal{E}(\boldsymbol{\rho}, z, \omega) \\ + 4\pi \int d\boldsymbol{\rho}' dz' \hat{\chi}(\boldsymbol{\rho}, \boldsymbol{\rho}', z, z', \omega) \cdot \mathcal{E}(\boldsymbol{\rho}', z', \omega)] = 0, \end{aligned} \quad (2.5)$$

where we distinguish between the  $z$ - and the in-plane  $\boldsymbol{\rho}$ -direction. In what follows we omit the  $\omega$ -dependence in the notation for the electric field, unless required. In Eq. (2.5) we assumed an uniform background with dielectric constant  $\epsilon_\infty$ , which models the semiconductor medium surrounding the QD. The in-plane and  $z$ -components of the electric field are defined as  $\mathcal{E} = (\mathbf{E}, E_z)$ . Because of the particular matrix form of tensor (2.4),  $E_z$  is not coupled to the polarization field and can be easily eliminated from Eq. (2.5). We solve the resulting equation for the in-plane electric field in reciprocal space. The Fourier transform to in-plane  $\mathbf{k}$ -space is defined as  $\mathbf{E}(\boldsymbol{\rho}, z) = \sum_{\mathbf{k}} \mathbf{E}_{\mathbf{k}}(z) \exp[i\mathbf{k} \cdot \boldsymbol{\rho}]$ .

After some algebra, the resulting equation for the in-plane components  $\mathbf{E}_{\mathbf{k}}(z)$  reads

$$-\left(1 + \frac{1}{k_z^2} \frac{\partial^2}{\partial z^2}\right) \begin{pmatrix} k_0^2 - k_y^2 & k_x k_y \\ k_x k_y & k_0^2 - k_x^2 \end{pmatrix} \mathbf{E}_{\mathbf{k}}(z) = 4\pi \frac{k_0^2}{\epsilon_\infty} \sum_{\mathbf{k}'} \int dz' \hat{\chi}_{\mathbf{k},\mathbf{k}'}(z, z') \cdot \mathbf{E}_{\mathbf{k}'}(z'), \quad (2.6)$$

where  $k_0 = (\omega/c) \sqrt{\epsilon_\infty}$  is the photon dispersion,  $\mathbf{k}$  and  $k_z = \sqrt{k_0^2 - k^2}$  are the in-plane and the  $z$ -component of the photon wave vector respectively. In what follows, the  $\omega$ -dependence of the various quantities in the equations is implicitly contained in their  $k_0$ - and  $k_z$ -dependence. In Eq. (2.6) the susceptibility  $\hat{\chi}_{\mathbf{k},\mathbf{k}'}(z, z')$  is now a rank-2 tensor acting on the  $(k_x, k_y)$ -plane, obtained by Fourier transforming to  $\mathbf{k}$ -space the  $(x, y)$ -block of the tensor (2.4). Eq. (2.6) can be solved using the scattering approach proposed in Ref. [Mart 98]. The background Green's function of the system is defined as the solution of the left-hand side of Eq. (2.6) with an inhomogeneous term  $\hat{\mathbf{I}}\delta(z)$  ( $\hat{\mathbf{I}}$ , being the 2 by 2 unit matrix) on the right-hand side and with outgoing boundary conditions. This Green's function can be derived analytically and reads

$$\hat{\mathbf{G}}_{\mathbf{k}}(z) = \frac{i}{2k_0^2 k_z} \begin{pmatrix} k_0^2 - k_x^2 & -k_x k_y \\ -k_x k_y & k_0^2 - k_y^2 \end{pmatrix} \exp(ik_z |z|). \quad (2.7)$$

The basis of this 2 by 2 tensor corresponds to the  $x$  and  $y$  directions of the electric field polarization and of the interband optical polarization. The nondiagonal terms give rise to the long-range part of the electron-hole exchange interaction, which is contained in a full Maxwell-Schrödinger formalism [Andr 94]. For a single QD having cylindrical symmetry, the nondiagonal terms average to zero when evaluating the optical transition amplitude, as expected in an isotropic system. If the system displays an anisotropy, as is the case for two or more QDs, these nondiagonal terms are responsible for the *longitudinal-transverse* (LT) or fine structure splitting of the resulting polariton modes. This result is discussed in detail in [Tass 90] in the case of a quantum well, where a complete description of the propagation of electromagnetic waves in an inhomogeneous material with translational symmetry broken in the  $z$ -direction is formulated using a non-local susceptibility analogous to (2.4), together with the Maxwell equations (2.5). The contributions to the susceptibility tensor are divided in those coming from the quantum confined electronic states of the well and those which are not dependent on these states. Two types of solutions of the Maxwell equations are identified, that are resonant polariton modes extending away from the

quantum-confining system, and surface polaritons which are confined into the well. Radiative shifts from the dispersion of the bare quantum well exciton and lifetimes of these resonances are analytically calculated, whose value is different if the polariton mode propagates in a direction that is parallel (L modes) or orthogonal (T modes) to the direction of propagation of the electromagnetic wave.

The Green's function (2.7) allows to express Eq. (2.6) in terms of a Dyson equation as follows

$$\begin{aligned} \mathbf{E}_{\mathbf{k}}(z) = & \mathbf{E}_{\mathbf{k}}^0(z) \\ & + 4\pi \frac{k_0^2}{\epsilon_\infty} \sum_{\mathbf{k}'} \int dz' dz'' \hat{\mathbf{G}}_{\mathbf{k}}(z - z') \cdot \hat{\chi}_{\mathbf{k},\mathbf{k}'}(z', z'') \cdot \mathbf{E}_{\mathbf{k}'}(z''), \end{aligned} \quad (2.8)$$

where  $\mathbf{E}_{\mathbf{k}}^0$  is a solution of the free propagating field in the dielectric background, namely in the absence of the resonant non-local susceptibility, and represents here an input electric field. As already pointed out, we consider cylindrical QDs whose thickness in the  $z$ -direction is very small compared to their size in the  $(x, y)$ -plane. In this case we can approximate the  $z$ -dependence of the electron-hole pairs wave functions  $\Psi_\alpha(\mathbf{r}_e, \mathbf{r}_h)$  calculated in Sec. 1.2 with a Dirac-delta function. This allows us to rewrite Eq. (2.8) in the simpler form

$$\mathbf{E}_{\mathbf{k}} = \mathbf{E}_{\mathbf{k}}^0 + 4\pi \frac{k_0^2}{\epsilon_\infty} \frac{\mu_{cv}^2}{\hbar} \sum_{\mathbf{k}', \alpha} \frac{\psi_{\alpha,\mathbf{k}} \psi_{\alpha,\mathbf{k}'}^*}{\omega_\alpha - \omega - i0^+} \hat{\mathbf{G}}_{\mathbf{k}} \cdot \mathbf{E}_{\mathbf{k}'}, \quad (2.9)$$

where all the quantities are defined at the  $(x, y)$ -plane position  $z = 0$ . Here,  $\psi_{\alpha,\mathbf{k}}$  is the two-dimensional Fourier transform of the in-plane projection of the electron-hole pair wave function in the  $\alpha$ -th QD,  $\psi_\alpha(\boldsymbol{\rho})$ . As we explained in Sec. 1.2, if  $\mathbf{R}_\alpha$  is the position of the QD in the chosen coordinate frame, then

$$\psi_\alpha(\boldsymbol{\rho}) = \varphi_\alpha(\boldsymbol{\rho} - \mathbf{R}_\alpha), \quad (2.10)$$

where  $\varphi_\alpha(\boldsymbol{\rho})$  is the  $\alpha$ -th QD wave function centered at the origin of the coordinate frame. The Fourier transform in  $\mathbf{k}$ -space then reads

$$\psi_{\alpha,\mathbf{k}} = \varphi_{\alpha,\mathbf{k}} \exp[i\mathbf{k} \cdot \mathbf{R}_\alpha], \quad (2.11)$$

where  $\varphi_{\alpha,\mathbf{k}}$  is given in Eq. (1.27). By projecting Eq. (2.9) onto the set of Fourier-transformed electron-hole pair wave functions  $\psi_{\alpha,\mathbf{k}}$ , we obtain

$$\mathbf{E}_\alpha = \mathbf{E}_\alpha^0 - \sum_{\beta} \frac{\hat{\mathbf{G}}_{\alpha\beta}}{\omega_\beta - \omega - i0^+} \mathbf{E}_\beta, \quad (2.12)$$

where  $\mathbf{E}_\alpha = \sum_{\mathbf{k}} \psi_{\alpha,\mathbf{k}} \mathbf{E}_{\mathbf{k}}$  and

$$\hat{\mathbf{G}}_{\alpha\beta} = -2\eta k_0^2 \sum_{\mathbf{k}} \psi_{\alpha,\mathbf{k}} \hat{\mathbf{G}}_{\mathbf{k}} \psi_{\beta,\mathbf{k}}^*. \quad (2.13)$$

is the coupling tensor, being  $\eta = 2\pi\mu_{cv}^2/\epsilon_\infty\hbar$ . Here, as above, the  $\omega$ -dependence enters these expressions through the definitions of  $k_0$ ,  $k_z$ , and  $\hat{\mathbf{G}}_{\mathbf{k}}$ . The set of functions  $\psi_{\alpha,\mathbf{k}}$  is in general a non-complete set and therefore, by making this projection, we lose information on the value assumed by the electric field  $\mathbf{E}_{\mathbf{k}}$  in all  $\mathbf{k}$ -space. Formally, once the quantities  $\mathbf{E}_\alpha$  have been computed, the electric field in all  $\mathbf{k}$ -space could in principle be reconstructed by solving again Maxwell equations, using the values  $\mathbf{E}_\alpha$  at each QD as source terms. As it will become clear later, however, the projected values of the electric field are sufficient for the purpose of the present analysis, which is to compute the polariton resonances of the system. It clearly emerges from the structure of Eq. (2.12) that, in the absence of coupling, the input field is scattered by each QD individually. Radiative coupling is responsible for the reabsorption of the scattered photons by other QDs, through the terms  $\hat{\mathbf{G}}_{\alpha\beta}$  with  $\alpha \neq \beta$ . In Sec.2.3 we solve the coupled Dyson Eqs. (2.12) in three different cases: a single anisotropic QD, two-QD and many-QD systems. Before showing this result, we now discuss the main characteristics of the coupling tensor.

## 2.2 The coupling tensor

Turning the sum into an integral, the QD coupling matrix in Eq. (2.13) can be written as

$$\begin{aligned} \hat{\mathbf{G}}_{\alpha\beta} = & -i\eta \int d\mathbf{k} \frac{\varphi_{\alpha,\mathbf{k}} \varphi_{\beta,\mathbf{k}}^*}{k_z} \begin{pmatrix} k_0^2 - k_x^2 & -k_x k_y \\ -k_x k_y & k_0^2 - k_y^2 \end{pmatrix} \\ & \times \exp[-ikR_{\alpha\beta} \cos(\phi - \theta_{\alpha\beta})], \end{aligned} \quad (2.14)$$

where  $\mathbf{R}_{\alpha\beta} = \mathbf{R}_\alpha - \mathbf{R}_\beta$  is the distance vector between QDs  $\alpha$  and  $\beta$ ,  $\phi$  and  $\theta_{\alpha\beta}$  are the angles that the vectors  $\mathbf{k}$  and  $\mathbf{R}_{\alpha\beta}$  respectively form with the  $x$ -axis of the chosen coordinate frame. In particular, in Eq. (2.14) the in-plane momentum  $k$  is integrated over the whole range, including both radiative modes with  $k < k_0$  and surface modes with  $k > k_0$ . These latter modes, which are evanescent in the  $z$  direction, span the largest part of the exchanged photon phase space and are thus ultimately responsible for the transfer mechanism we are describing. Eq. (2.14) accounts also for the LT splitting in anisotropic dots, as we show in the next section. For each pair of isotropic QDs, it is possible to set the  $x$ -axis along  $\mathbf{R}_{\alpha\beta}$  by rotating the 2

by 2 matrix in Eq. (2.14) by an angle  $\theta_{\alpha\beta}$ . The rotation results in a diagonal coupling matrix is

$$\hat{\mathbf{G}}'_{\alpha\beta} = \hat{\mathbf{R}}_{\theta_{\alpha\beta}} \hat{\mathbf{G}}_{\alpha\beta} \hat{\mathbf{R}}_{\theta_{\alpha\beta}}^{-1} = \begin{pmatrix} g_{\alpha\beta}^L & 0 \\ 0 & g_{\alpha\beta}^T \end{pmatrix}, \quad (2.15)$$

in which the two field polarizations are decoupled. In Eq. (2.15)  $\hat{\mathbf{R}}_{\theta_{\alpha\beta}}$  is the rotation matrix. In the rotated basis, is now possible to analytically integrate the angular dependence of tensor (2.15), finally resulting in the coupling tensor

$$\begin{aligned} \hat{\mathbf{G}}'_{\alpha\beta} = & -i \int \frac{k dk}{k_z} \varphi_{\alpha,\mathbf{k}} \varphi_{\beta,\mathbf{k}}^* \\ & \times \left[ \eta_1 \begin{pmatrix} k_z^2 & 0 \\ 0 & k_0^2 \end{pmatrix} J_0(kR_{\alpha\beta}) + \eta_2 \begin{pmatrix} k & 0 \\ 0 & -k \end{pmatrix} \frac{J_1(kR_{\alpha\beta})}{R_{\alpha\beta}} \right], \end{aligned} \quad (2.16)$$

where  $J_n(x)$  is the  $n$ -th order Bessel function of the first kind,  $\eta_1 = 2\pi\eta$  and  $\eta_2 = 4\sqrt{\pi}\Gamma(3/2)\eta$ , being  $\Gamma(x)$  the Euler gamma function. The integral over  $k$  is performed numerically. The result is then rotated back by an angle  $-\theta_{\alpha\beta}$  to obtain the complete coupling matrix in the original coordinate frame, that reads

$$\hat{\mathbf{G}}_{\alpha\beta} = \begin{pmatrix} g_{\alpha\beta}^L \cos^2 \theta_{\alpha\beta} + g_{\alpha\beta}^T \sin^2 \theta_{\alpha\beta} & (g_{\alpha\beta}^L - g_{\alpha\beta}^T) \sin \theta_{\alpha\beta} \cos \theta_{\alpha\beta} \\ (g_{\alpha\beta}^L - g_{\alpha\beta}^T) \sin \theta_{\alpha\beta} \cos \theta_{\alpha\beta} & g_{\alpha\beta}^L \sin^2 \theta_{\alpha\beta} + g_{\alpha\beta}^T \cos^2 \theta_{\alpha\beta} \end{pmatrix}. \quad (2.17)$$

In Eq. (2.16), it is immediate to identify the radiative and the Förster contributions of the coupling tensor as the first and the second term in square brackets respectively. In fact, all the Bessel functions of the first kind  $J_n(x)$  display an oscillatory behaviour with an amplitude that decays as  $1/\sqrt{x}$  for  $x \rightarrow \infty$ , so that the square modulus of these two terms decay as  $R_{\alpha\beta}^{-1}$  and  $R_{\alpha\beta}^{-3}$  respectively. Moreover, only the first contribution depends on the speed of light  $c$  via the terms  $k_0^2$  and  $k_z^2$  and goes to zero in the instantaneous limit. In Fig. 2.2 we show a logarithmic scale plot of the transverse component of the coupling matrix versus the interdot distance  $R_{\alpha\beta}$ , in the case of two energetically degenerate QDs, together with the two separate contributions, as dashed and dotted lines, according to Eq. (2.16). The energy scale is relative to the physical parameters of Stranski-Krastanov grown InAs/GaAs QDs, reported in Tab. 2.1 together with those of CdSe QDs that we use in section 2.3.3. The figure shows that the  $R^{-3}$  contribution is dominant for closely spaced QDs, while the radiative contribution decaying as  $R^{-1}$  takes over with increasing the dot-dot distance. Although the overall coupling rate is small, corresponding to a transfer time of above 1 ns, at long distance the

radiative mechanism nevertheless dominates over FRET and must therefore be accounted for when considering QD coupling in future applications where long transfer times are important.

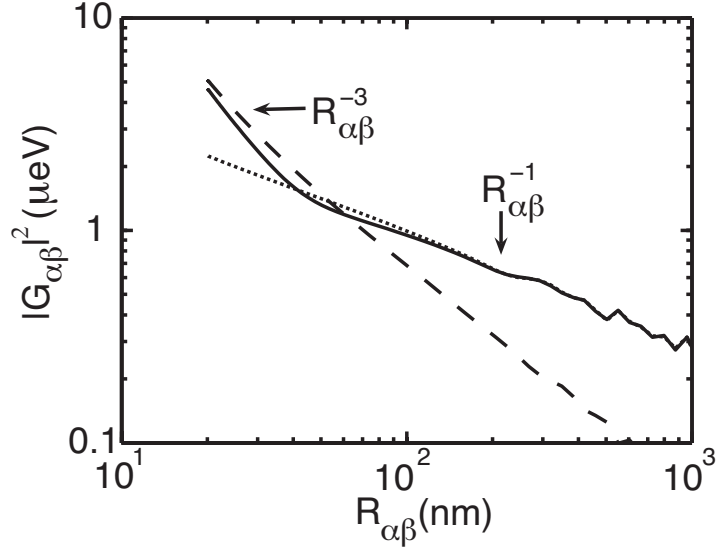


Figure 2.2: The square modulus of the transverse component  $[\hat{\mathbf{G}}'_{\alpha\beta}]_{y,y}$  of the coupling tensor is plotted versus interdot distance (solid line). The F\u00f6rster (dashed line) and the radiative (dotted line) contributions dominate in the short- and in the long-range respectively. The energy scale is relative to InAs QDs whose physical parameters are given in Tab. 2.1.

	InAs	CdSe
$\epsilon_{\infty}$	12.5	8.35
$E_G$ (meV)	1200	2200
$m_e(m)$	0.067	0.13
$m_h(m)$	0.14	0.45
$\mu_{cv}$ (meV $\cdot$ nm <sup>3</sup> )	480	780
$\varrho$ (nm)	10	2.5
density(QDs/ $\mu\text{m}^2$ )	300	1000

Table 2.1: Physical parameters for InAs and CdSe QDs.  $E_G$  is the energy gap between the valence band and the conduction band.  $m_e$  and  $m_h$  are the electron and hole in-plane effective masses in free electron mass units  $m$ . The spatial densities of QDs in the column line are used for the numerical simulations discussed in section 2.3.3.

## 2.3 Numerical results

In this section, we solve the coupled Dyson Eqs. (2.12) for different QDs systems. In order to have a quantitative estimate of the effect of the coupling, we show results relative to the realistic case of self-assembled InAs/GaAs QDs. As we have seen in Sec. 1.1.4, these structures attract great interest because of the high quality of their crystalline structure, that is intrinsic to the Stranski-Krastanov growth process, and that reflects in high level electro-optical performances. For comparison, in Sec. 2.3.3 we discuss a result relative to CdSe QDs, grown by molecular beam epitaxy (MBE) [Litv 02].

The polariton resonances of the multiple-QD system are the poles of the homogeneous set of equations obtained by setting  $\mathbf{E}_\alpha^0 = 0$  in Eq. (2.12). We compute these poles numerically within the exciton-pole approximation [Tass 90, Citr 93b, Jord 93, Jord 94], which consists in replacing the  $\omega$ -dependence of  $\hat{\mathbf{G}}_{\alpha\beta}$  tensor by an average electron-hole energy  $\hbar\omega_0$ . This approximation is generally valid when the dielectric medium does not present sharp resonances, as is the case in the present model where the QDs are embedded in a constant dielectric background. In order to check the validity of this assumption, we evaluated the  $\omega$ -dependence of the coupling tensor  $\hat{\mathbf{G}}_{\alpha\beta}$  for a pair of QDs and checked that all its components are essentially constant over the energy interval corresponding to a typical inhomogeneous QD distribution. Some of these components are plotted in Fig. 2.3 as a check. Complex eigenenergies  $\Omega_n = \Delta_n - i\Gamma_n$  are obtained, corresponding to collective radiative modes of the QD ensemble. The number of these poles is twice the number of QDs, corresponding to the two independent states of the interband polarization vector. The real part of the  $n$ -th eigenvalue  $\Delta_n$  induces a radiative shift with respect to the energies of the non-interacting dots, while the imaginary part  $\Gamma_n$  represents the radiative recombination rate of the  $n$ -th collective mode of the system. We first address the case of a single dot, showing how the fine-structure splitting rises from the asymmetry. Then we consider a two-QD system, in order to establish how the radiative coupling mechanism depends on the detuning and on the mutual QD distance. Finally, we discuss the results obtained for an ensemble of several dots.

### 2.3.1 LT spitting for one anisotropic QD

The formalism developed in Sec. 2.1, allows to compute the polariton resonances of any two-dimensional system that is coupled to a radiative field. Here we address the problem of calculating the LT energy splitting of the two polariton modes in a single anisotropic QD. In this case, the coupling

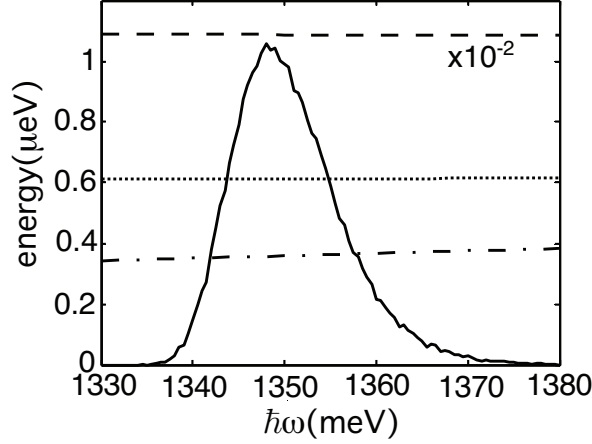


Figure 2.3: QD transition energy distribution (solid line, arbitrary units). The asymmetry with a more pronounced high-energy tail is due to  $R^{-2}$ -dependence of the  $\alpha$ -th QD confinement energy on the QD radius  $R_\alpha$ , the radii being Gauss-distributed. The  $(x, x)$ -component of the coupling energy tensors  $\text{Re}(G_\alpha)$  (dashed line, see section 2.3.1 for the definition of  $G_\alpha$ ),  $\text{Re}(G_{\alpha\beta}^{xx})$  (dotted line), and  $\text{Im}(G_\alpha)$  (dot-dashed line), for two QDs labelled  $\alpha$  and  $\beta$ , is plotted as a function of  $\hbar\omega$ .

tensor in Eq. (2.14) simplifies to

$$\hat{\mathbf{G}}_{\alpha\alpha} = -i\eta \int d\mathbf{k} \frac{|\varphi_{\alpha,\mathbf{k}}|^2}{k_z} \begin{pmatrix} k_0^2 - k_x^2 & -k_x k_y \\ -k_x k_y & k_0^2 - k_y^2 \end{pmatrix}. \quad (2.18)$$

It is straightforward to verify that if the electron-hole pair wave function of the dot has cylindrical symmetry in the  $(x, y)$ -plane, then the non-diagonal terms of Eq. (2.18) integrate to zero. Moreover, the diagonal terms are identical and the coupling tensor reads  $\hat{\mathbf{G}}_{\alpha\alpha} = \hat{\mathbf{I}}G_\alpha$  with

$$G_\alpha = -i\pi\eta \int_0^\infty dk |\varphi_{\alpha,\mathbf{k}}|^2 \frac{k(2k_0^2 - k^2)}{k_z}. \quad (2.19)$$

The quantity  $G_\alpha$  is the radiative self energy of the  $\alpha$ -th QD, with its real and imaginary parts describing the radiative energy shift and radiative linewidth (inverse lifetime) respectively. Then, there is no energy splitting between the longitudinal and the transverse exciton in a cylindrical dot. On the other hand, if the dot is anisotropic, as it is always the case in real QDs, the  $x - y$  symmetry of the integrals in Eq. (2.18) is lost, and a finite fine structure splitting is recovered. The simplest way to introduce a geometrical anisotropy in our equations, is to consider a dot whose projection in the

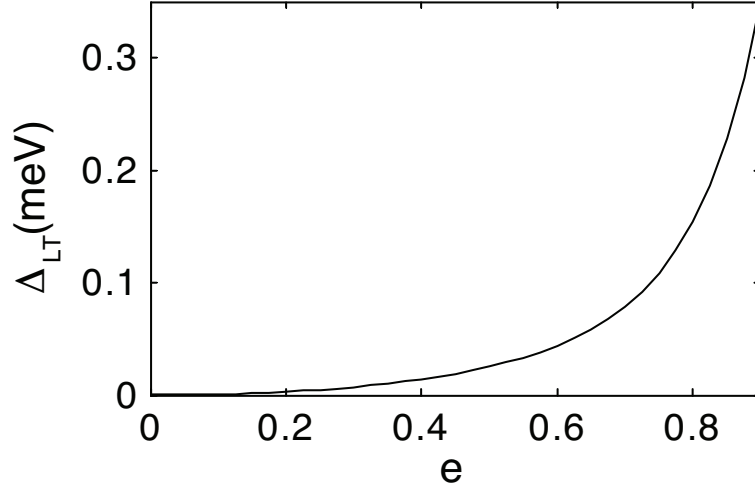


Figure 2.4: L-T splitting of the two polariton modes of a single elliptical InAs QD versus eccentricity.

$(x, y)$ -plane is an ellipse. This choice also allows to quantify the anisotropy by means of a parameter, that is the eccentricity of the ellipse. In Fig. 2.4 the calculated L-T splitting of the two polariton modes is plotted versus the eccentricity, for an InAs QD. It is evident that the fine structure splitting increases dramatically by increasing the eccentricity of the dot, that is, its *anisotropy*.

### 2.3.2 Two QDs: dependence on distance and detuning

In this paragraph we address a two-QD system, in order to establish how the radiative coupling mechanism depends on the *detuning* and to show how its dependence on the mutual QD distance  $R_{\alpha\beta}$  reflects on the polariton modes of the ensemble. Here, the detuning is defined as the difference between the optical transition energies of the two QDs. In particular, we assume cylindrical InAs QDs. The detuning is changed by varying the size of one of the QDs. In Fig. 2.5 the imaginary (a) and the real (b) part of the poles of Eq. (2.12) (that is,  $\Gamma_n$  and  $\Delta_n$  respectively) are plotted versus the detuning  $\hbar\delta\omega = \hbar(\omega_1 - \omega_2)$  of the two QDs, at a fixed distance  $R_{\alpha\beta} = 50$  nm. The numerical simulations show that, as expected, no appreciable coupling effect is observed for large detuning. On the other hand, for small detuning the energies of the four poles are well distinct. In particular, if we look at  $\Gamma_n$  in Fig. 2.5.(a), we can see that two *sub-radiant* and two *super-radiant* states are present. The two states with small  $\Gamma_n$ , thus, decay in a time much longer than

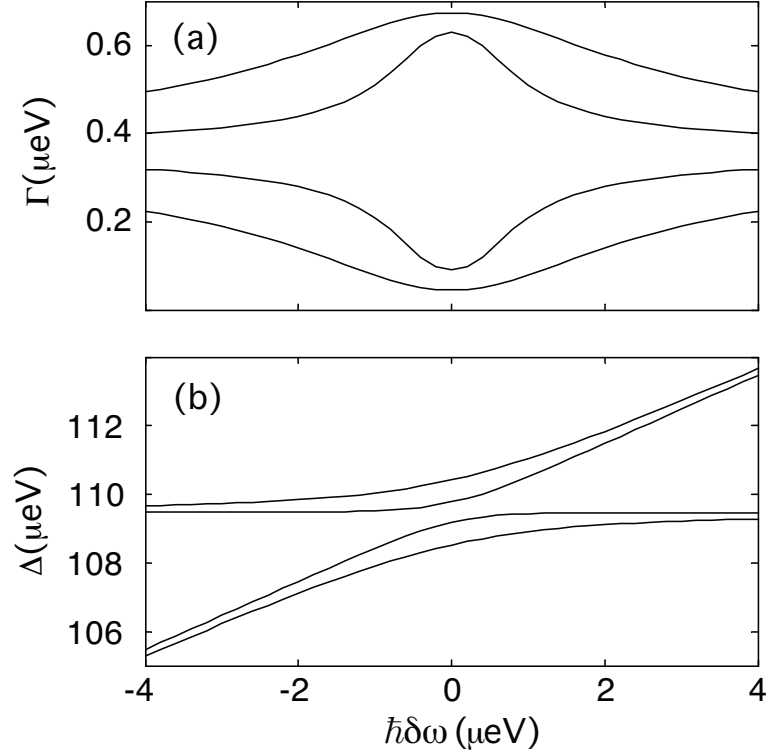


Figure 2.5: Imaginary (a) and real (b) part of the energy poles as a function of the detuning between two InAs QDs, at fixed distance  $R_{\alpha\beta} = 50$  nm. Note that for small detuning the four poles are well separated in energy, so that in (a) two sub-radiant and two super-radiant states are distinguishable.

the two others. The computed energy shift with respect to non-interacting dots is of the same order of  $\Gamma_n$ , that is of the order of  $1 \mu\text{eV}$ . Such an energy shift is negligible if compared to the typical inhomogeneous broadening of a QD ensemble. The main consequence of radiative coupling is thus the effect on the lifetimes of the collective modes of the system.

Fig. 2.6 displays the dependence of the interaction on the distance between the QDs. The imaginary (a) and the real (b) part of the poles oscillate as a function of the distance between the two dots. The oscillations originate from interference effects. At distances which are multiple of the half wavelength, anti-Bragg conditions are satisfied and the oscillations display a maximum or a node, respectively. Fig. 2.6 also illustrates the long-range character of this radiative coupling mechanism already described in the previous section. Using the analytical expression of the coupling tensor in Eq. (2.16) we have already shown that the magnitude of the coupling decreases

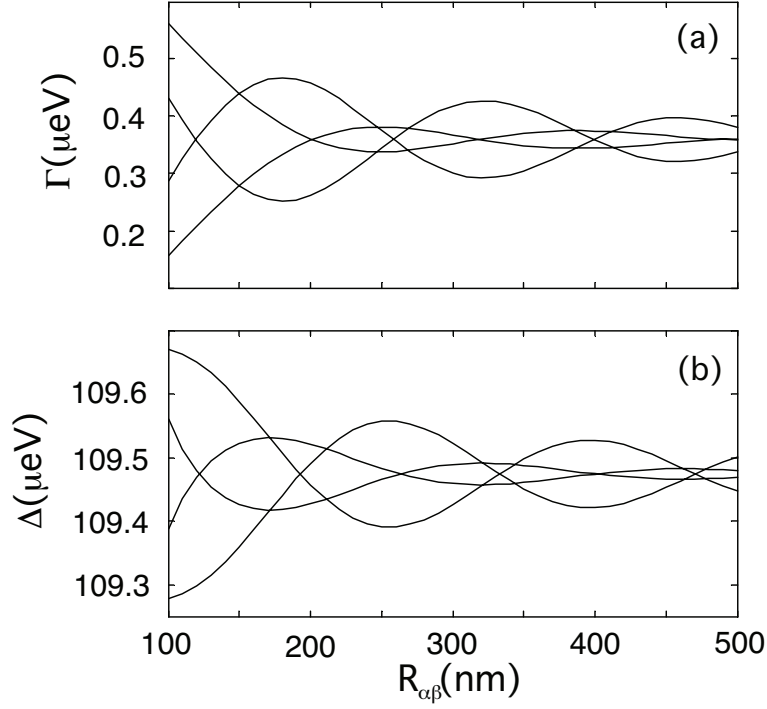


Figure 2.6: Imaginary (a) and real (b) part of the energy poles as a function of the distance between two InAs QDs, at zero detuning. The oscillatory nature of the interaction as a function of distance, according to the anti-Bragg condition, clearly appears.

as  $R_{\alpha\beta}^{-1}$  (see Fig. 2.2). The same polynomial decay is obtained for the envelope of the curves in Fig. 2.6.(a) and (b). As already pointed out, this dependence is much slower than the characteristic  $R_{\alpha\beta}^{-3}$  dependence of the Förster coupling [Fors 65, Govo 03].

### 2.3.3 N-QDs ensemble

Now that the features of the radiative coupling mechanism have been clarified, we consider the case of a large number of interacting QDs. The same emission-absorption mechanism that couples a pair of dots can now involve several QDs and the transfer of excitation between them results in collective modes analogous to the ones previously described, that is, sub-radiant or super-radiant if compared to the excited states of the non-interacting dots. As a first example, we consider InAs QDs (see Tab. 2.1) which are randomly distributed on the  $(x, y)$ -plane. In a real situation, the dots have different

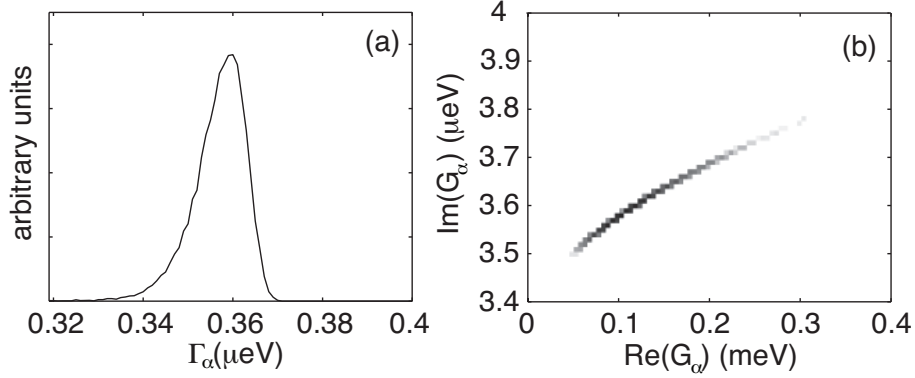


Figure 2.7: (a) Histogram representing the energy distribution of the single QD radiative rates, expressed as the imaginary part of the single QD radiative self-energy  $\Gamma_\alpha = \text{Im}(G_\alpha)$ . (b) Two-dimensional histogram of the distribution of the real and imaginary parts of the single-QD radiative self-energy.

shape, size and composition causing the inhomogeneous energy broadening of the QD luminescence spectrum. To simulate this broadening, we introduce a Gauss distributed dot size centered at dot radius  $\varrho = 10$  nm, with a standard deviation of  $\delta\varrho = 1$  nm. This variance in size induces a variation of the confinement energy  $\hbar\delta\omega$  which is proportional to  $\delta\varrho/\varrho^3$  as implied by the energy quantization of a particle in a box. This energy variation is what finally produces the inhomogeneous energy distribution of the QDs. The choice  $\delta\varrho = 1$  nm, given our simple model for the QD wave functions, results in an inhomogeneous broadening of about 15 meV, as seen in Fig. 2.3. The asymmetry of this distribution, with a more pronounced high-energy tail, is simply related to the  $\varrho^{-3}$ -dependence of the confinement energy and to the Gauss assumption for the distribution of QD sizes. The same size fluctuation is also responsible for a variation of the QD optical matrix element [Borr 02] and consequently of both its radiative shift and lifetime, via the diagonal part (i.e.  $\beta = \alpha$ ) of Eq. (2.12) and the single-dot self-energy (2.19). The numerically computed radiative energy shifts are of the order of a few  $\mu\text{eV}$ , thus negligible if compared to the QD inhomogeneous energy broadening. They are therefore irrelevant to the present discussion. The imaginary part of the single-dot self-energy is on the contrary what gives the inhomogeneous distribution of radiative linewidths  $\Gamma_\alpha = \text{Im}(G_\alpha)$ . Their distribution is plotted in Fig. 2.7.(a). Finally, in Fig. 2.7.(b) a two-dimensional histogram of  $\text{Re}(G_\alpha)$  and  $\text{Im}(G_\alpha)$  shows the correlation between radiative shift and radiative broadening resulting from the present model. In a realistic situation [Borr 02], a variation of the dipole moment is not only induced by

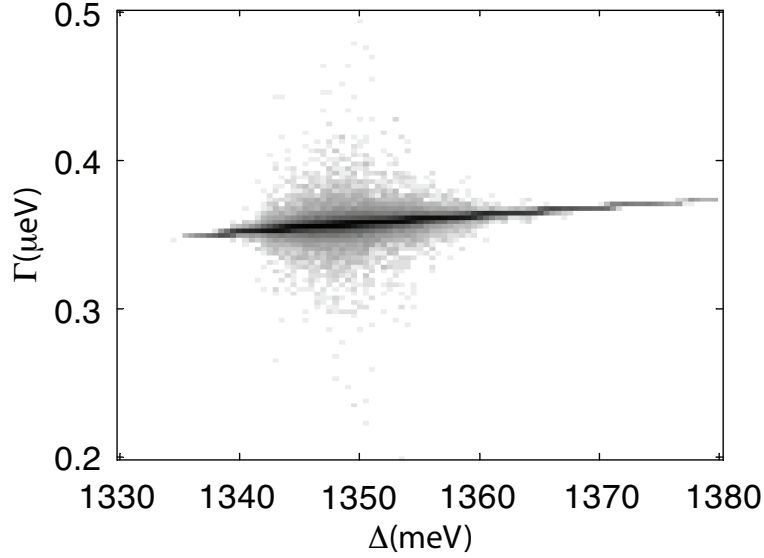


Figure 2.8: Histogram expressing the number of collective modes as a function of the real and imaginary part of the complex energy poles of an InAs QDs ensemble. Logarithmic color scale over three orders of magnitude. Because of the radiative coupling, a fraction of the QDs shows a large radiative shift compared to the case of non-interacting QDs in Fig. 2.7.(b).

size fluctuations. Other factors such as QD shape, strain and piezoelectric fields, and indium concentration within the QD body produce a variation of dipole moment even for a fixed QD size [Lang 04a]. The 20% variance of the dipole moments derived in [Borr 02] is significantly larger than the one obtained here from size fluctuations (approx. 3% for the InAs case). However we note that the inhomogeneous broadening of the sample by Borri *et al.* is also larger than the one considered here, presumably due to an even larger QD-size fluctuation. Introducing a larger size fluctuation in the present model would partly account for the observed dipole-moment fluctuation. Our final result for a radiatively-coupled QD ensemble however (see discussion below and Figs. 2.8 and 2.9), predicts an even broader distribution of radiative linewidths which might be at least partly responsible for the measured dipole moment distribution.

We compute the collective modes of an ensemble of 100 QDs by finding the complex poles of Eq. (2.12). We repeat this procedure for many random realizations of the system. Provided the system size is larger than the wavelength, we expect this configuration average to give the same results as a simulation over a larger spatial domain. This is expected because of the fall-off

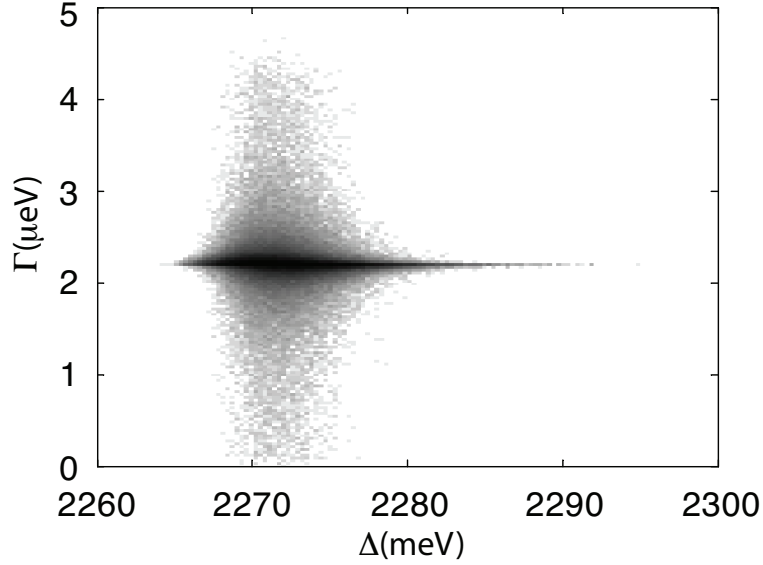


Figure 2.9: The same histogram of Fig. 2.8, but for CdSe QDs. In this case radiative shifts up to one order of magnitude larger than in the case of InAs QDs are obtained as an effect of the coupling.

scale computed in Fig. 2.6. In particular, the occurrence of quasi-degenerate QD pairs within a given realization has a finite though small probability. Repeating the simulation over many randomly generated configurations finally allows to sample over a large-enough number of such quasi-degenerate cases and produces a significant statistics. We plot in Fig. 2.8 an histogram, on a logarithmic scale, of the real and imaginary parts of the computed energy poles. Most of the collective modes lie on the curve determined by the distribution of non-interacting QDs displayed in Fig. 2.7.(b), due to the large detunings that are induced by the inhomogeneity of the QD ensemble. Nevertheless, for a small fraction of the states a large radiative shift is achieved, as a result of the coupling. We also point out that the deviation from the non-interacting QDs case is more pronounced at the center of the QD inhomogeneous line. The reason is that, as already stated, the radii of the QDs are Gauss-distributed around a mean value. Most of the QDs fall in this energy region and consequently small values of the detuning are more likely to occur. For different materials, one can observe larger radiative coupling effects. In Fig. 2.9 we show the histogram obtained for a CdSe QD sample (see parameters in Tab. 2.1). Once again the histogram results from many realization of the sample, with randomly distributed QDs, having randomly Gauss-distributed size. In this case the deviation from the noninteracting

case is more pronounced because of the higher QD density and of the larger dipole matrix element  $\mu_{cv}$ . A radiative shift of a few  $\mu\text{eV}$  is achieved, that is one order of magnitude larger with respect to the case of InAs QDs. In this case, some of the collective modes have vanishing radiative rates, showing how the radiative coupling can profoundly change the dephasing rates of many QD systems.

## 2.4 Conclusions

We have shown that, already in the simplified picture of the macroatom, QDs do not behave as isolated objects. The radiative coupling between QDs causes the emergence of collective modes that are sub-radiant and super-radiant with respect to the excited state of an isolated QD. The effect on the radiative decay-rate is expected to be of the order of 1  $\mu\text{eV}$  and to strongly depend on the dipole matrix element of the material that constitutes the QDs and on their spatial density. Despite its small magnitude, radiative coupling decays as  $1/R$  and effectively couples QDs over a distance of a few hundreds of nanometers. We have shown that the radiative coupling is a long-range correction to the FRET mechanism, due to the retardation in the electromagnetic field propagation [Para 05, Para 07]. In [Para 05] we suggest that in a dense QD sample this effect should be observable as a non-exponential decay of the photoluminescence (PL) signal. Recently [Sche 07] Scheibner *et al.* have observed the increase of the PL emission rate in QD mesas when passing from strictly non-resonant to quasi-resonant excitation, suggesting radiative coupling between the QDs. Furthermore, by reducing the QD density (i.e. QD are physically removed from the sample) they verify that the range of the interaction in CdSe/ZnSe QDs is at least 150 nm. This result seems to provide a first evidence of radiative coupling. However, more accurate experiments, perhaps with spatial resolution [Lang 06], will be required to fully characterize this phenomenon.



## Chapter 3

# Phonon-induced exciton dephasing in QD molecules

Semiconductor quantum dots (QDs) are often considered as candidate devices for a solid-state implementation of quantum information processing [Loss 98, Burk 99, Biol 00, Li 03]. This interest is justified by the alleged long-lasting coherence of the interband polarization, which might be exploited for storing quantum information. Robustness against decoherence in QDs is usually expected as a result of quantum confinement, implying discrete energy levels below the semiconductor bandgap with a very restricted phase space available for various scattering mechanisms. This simplified view was however recently questioned, after the observation of a very efficient decoherence mechanism due to strong electron-phonon coupling [Beso 01, Borr 01, Fave 03]. The strongly localized polarization in an excited QD can induce virtual inelastic phonon emission and reabsorption processes which act as a phase-destroying mechanism. Theoretically, this stems from the exact solution of a two-level system coupled to a phonon bath - the so called *independent boson model* (IBM) [Maha 90]. In practice, the decoherence rate of the interband polarization is extremely fast in the first few picoseconds following excitation and becomes very small afterwards. To this corresponds a distinctive spectral feature with a sharp zero-phonon line (ZPL) and phonon-assisted broad sidebands. Both time-resolved and spectral signatures of this mechanism have been characterized by several groups [Beso 01, Borr 01, Fave 03, Krum 02, Zimm 02, Lang 04b, Mulj 04].

According to the IBM, that takes into account only the linear coupling to phonons, the ZPL relative to a single QD electron-hole level is not broadened. The measured ZPL linewidth, and the consequent dephasing time in the nanosecond range [Borr 01], are seemingly related to the radiative recombination process [Lang 04b]. Another source of dephasing, not included

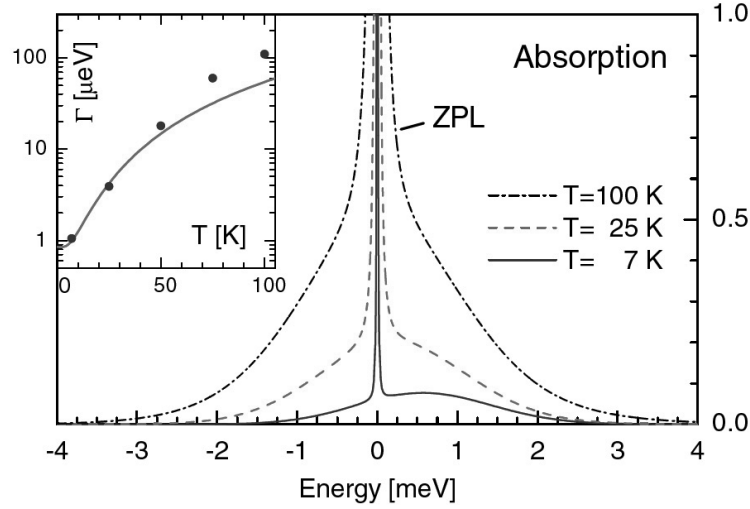


Figure 3.1: Absorption spectra for an InAs QD at different temperatures. The ZPL transition energy is taken as zero of energy. Inset: Calculated broadening of the ZPL (solid line) compared with the experimental results by Borri *et al.* [Borr 01] (circles) (from [Mulj 04]).

in the IBM, is the finite phonon decay rate  $\gamma_{\mathbf{q}} > 0$  [Goup 02, Zimm 02]. Furthermore, a recent theoretical analysis [Mulj 04] has suggested that virtual acoustic-phonon-assisted transitions to excited levels might provide a dephasing of the ZPL, with a rate comparable to the radiative one. The QD spectra and the broadening of the ZPL calculated by Muljarov *et al.* are shown in Fig. 3.1, where are compared to the experimental results by Borri *et al.* [Borr 01]. According to this analysis, based on *exact* numerical solution of the quadratic coupling to phonons, they also demonstrate that the spectrum produced by quadratic coupling to dispersionless longitudinal optical (LO) phonons consists of discrete unbroadened lines, as long as a few exciton levels are taken into account [Mulj 06a]. Nevertheless, the inclusion of a very large number of exciton states results in spectral broadening and in pronounced LO phonon-induced dephasing [Mulj 06b].

Recently, the system of two vertically stacked QDs, called QD molecules, has been experimentally studied [Baye 01, Borr 03, Ortn 05b]. A QD molecule might in principle provide the minimal system of two coupled qubits required for the implementation of quantum gates [Burk 99, Biol 00]. The electron and hole wave functions in QD molecules can tunnel through the thin barrier separating the QDs, giving rise to exciton states [Best 04, Vill 04, Ortn 05b], whose energies are split by the effect of tunneling through the barrier and by

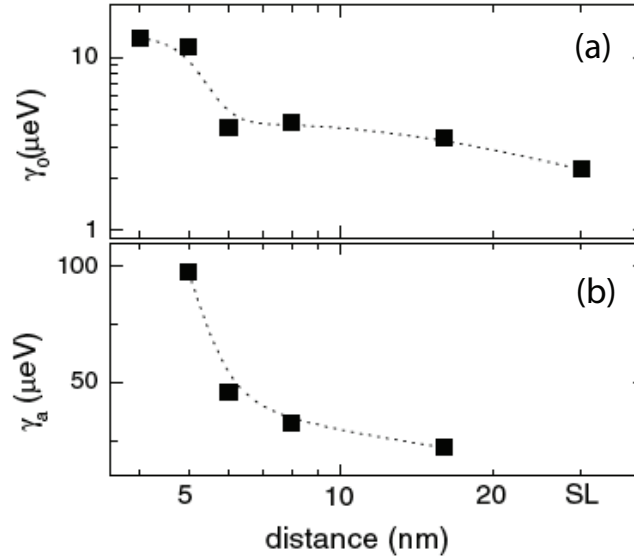


Figure 3.2: Dependence on the interdot distance of (a) the zero-temperature extrapolated ZPL width and of (b) the ZPL width at  $T = 10$  K. SL corresponds to single layer data (from [Borr 03]).

Coulomb interaction. Nevertheless, as already for a single QD, the phonon induced dephasing of the exciton polarization in the QD molecule is a major obstacle to the realization of a semiconductor-based implementation of a quantum gate. The suppression of the phonon dephasing in QD molecules via external magnetic field has been hypothesized in [Bert 04] while according to [Zana 98] it would result from the periodicity of the multidot quantum states in a regular array of many QDs. However, in both cases a very precise control of the QD structural and electronic properties is required. In a recent experimental study using coherent ultrafast four-wave-mixing spectroscopy [Borr 03], the decoherence time of the exciton interband polarization in QD molecules has been measured. It turns out that the ZPL linewidths are generally larger than in the case of a single QD by almost one order of magnitude. Furthermore, the linewidths decrease dramatically as the interdot distance is increased. This result is shown in Fig. 3.2. Quantitatively, these larger linewidths can only partially be explained in terms of the larger volume of exciton states in a QD molecule, while the strong dependence on the interdot distance is still unexplained.

In this chapter we present a model of exciton optical response in a QD molecule, accounting for the strong exciton-acoustic-phonon interaction. In Sec. 3.1, the electron-phonon coupling is treated within the second-order

Born approximation in the non-Markov limit. In Sec. 3.2, we discuss our numerical results. Linear optical spectra are computed at varying interdot distance. ZPL widths in the order of tens of  $\mu\text{eV}$  are calculated that oscillate versus the interdot distance, according to previous results [Mulj 05]. The oscillations are attributed to a wave-matching effect between the phonon wavelength and the interdot distance, which enhances the phonon-assisted scattering from bright to dark states. These results could explain the strong distance dependence measured [Borr 03]. Finally, in Sec. 3.3 we give some concluding remark.

### 3.1 Exciton-phonon coupling in second order Born approximation

In this section we develop a model for the exciton-acoustical-phonon linear coupling in QD molecules. The QD molecule exciton states are described within the effective mass scheme, according to Sec. (1.2). Starting from the standard hamiltonian for localized excitons coupled to lattice vibration, we develop a density matrix formalism for the linear interband polarization. This is done in the framework of the second-order Born (2B) approximation for the exciton-phonon interaction, without performing the Markov limit. This approximation is known to reproduce qualitatively and, to a fairly good accuracy, quantitatively the exact result in the single QD case [Krum 02].

#### 3.1.1 QD molecule and interaction Hamiltonian

The QD system addressed in this chapter is a dot molecule composed of two vertically stacked cylindrical QDs at mutual distance  $R$ , as sketched in Fig. 1.3.(b). As already in Chapter 2, we refer to self assembled InAs QDs, whose physical parameters are given in Tab. 3.1. Neglecting the Coulomb interaction, the electron and hole wave functions  $\Phi_i^c(\mathbf{r})$  and the corresponding energies  $E_j^c$  (being  $c = e, h$  and  $i = 1, 2$ ) are calculated in Sec. 1.2 within two-band effective-mass approximation. In particular, here we assume  $\sigma_e = 6.5 \text{ nm}$  ( $\sigma_h = 6.0 \text{ nm}$ ) as standard deviation of the electron (hole) in-plane gaussian wave function, while the  $z$ -component is calculated for a QD height  $h = 1 \text{ nm}$ . Furthermore, a small asymmetry in the confining potential (see Eq. 1.30) accounts for the fluctuations of components concentration from dot to dot, as well as for size and shape fluctuations. A realistic description of a self-assembled QD ensemble must take into account this kind of asymmetry that is intrinsic to the Stranski-Krastanow growth mode [Stra 37], as explained in Sec. 1.1.4. Then, as in [Mulj 05], we suppose

$\epsilon_\infty$	$E_G$ (meV)	$V_e$ (meV)	$V_h$ (meV)	$m_e(m)$	$m_h(m)$
12.5	1200	671.7	287.9	0.027	0.265
$m_e^b(m)$	$m_h^b(m)$	$s$ (m/s)	$\rho_m$ (g/cm <sup>3</sup> )	$D_c$ (eV)	$D_v$ (eV)
0.067	0.327	$4.6 \cdot 10^3$	5.67	-13.6	-7.1

Table 3.1: Material parameters used for InAs/GaAs QDs.  $\epsilon_\infty$  is the background dielectric constant.  $E_G$  is the energy gap between the valence band and the conduction band. We assume finite band offsets  $V_e$  and  $V_h$  between the QD and the barrier material.  $m_e$  and  $m_h$  ( $m_e^b$  and  $m_h^b$ ) are the electron and hole effective mass along  $z$  in the QD (barrier) respectively, in free electron mass units  $m$ . The parameters that enter the electron-phonon coupling (see Eq. (3.4)) are the sound velocity  $s$ , the mass density  $\rho_m$  and the deformation potential constants  $D_c$  and  $D_v$  for the conduction and valence bands.

that the confining potentials of the bottom QD are 2% deeper than those of the top one. Given the large energy separation of higher levels, compared to the Coulomb and deformation potential interactions, we can restrict our calculations to the two lowest electron and hole levels. As we are going to describe the electron-phonon interaction in a second quantization formalism, it is useful to give the representation of these states in the Fock space. Here, at the state  $\Phi_i^e(\mathbf{r})$  ( $\Phi_i^h(\mathbf{r})$ ) corresponds the ket  $\hat{c}_i^\dagger|0\rangle$  ( $\hat{d}_i^\dagger|0\rangle$ ), where  $\hat{c}_i^\dagger$  and  $\hat{c}_i$  ( $\hat{d}_i^\dagger$  and  $\hat{d}_i$ ) are the time-dependent electron (hole) operators, obeying Fermi commutation rules, and  $|0\rangle$  is the vacuum state in the electron-hole representation.

The Hamiltonian that describes the QD molecule in interaction with the acoustic-phonon bath is

$$\hat{H} = \hat{H}_{QD} + \hat{H}_{ph}. \quad (3.1)$$

Here, the QD molecule Hamiltonian can be written as the sum of two terms  $\hat{H}_{QD} = \hat{H}_0 + \hat{H}_c$ , that read

$$\hat{H}_0 = \sum_{i,\gamma} \left( E_i^e \hat{c}_i^\dagger \hat{c}_i - E_i^h \hat{d}_i^\dagger \hat{d}_i \right), \quad (3.2a)$$

$$\hat{H}_c = - \sum_{ijklm} V_{ijlm}^{eh} \hat{c}_i^\dagger \hat{c}_j \hat{d}_l^\dagger \hat{d}_m, \quad (3.2b)$$

the first being the bare carrier contribution, the second the electron-hole (e-h) Coulomb interaction. The latter is included in our model because the phonon-mediated effects we are describing depend on the difference in binding energies between distinct exciton levels. Note that in Eq. (3.2b) we consider only e-h terms, thus neglecting electron-electron (e-e) and hole-hole (h-h)

terms that give rise to terms proportional to the densities of particles, and would therefore be important only beyond the limit of linear optical response. The Coulomb matrix elements  $V_{ijlm}^{eh}$  are calculated according to Eq. (1.33a). Electron states are coupled to acoustic-phonons via the deformation potential interaction. The electron-phonon interaction Hamiltonian can be written as  $\hat{H}_{ph} = \hat{H}_{ph}^d + \hat{H}_{ph}^{nd}$ , where its diagonal and non-diagonal parts are

$$\hat{H}_{ph}^d = \sum_{\mathbf{q}} \hbar\omega_{\mathbf{q}} \hat{a}_{\mathbf{q}}^\dagger \hat{a}_{\mathbf{q}} + \sum_{i,\mathbf{q}} \left( M_{\mathbf{q}}^{ie,ie} \hat{c}_i^\dagger \hat{c}_i - M_{\mathbf{q}}^{ih,ih} \hat{d}_i^\dagger \hat{d}_i \right) (\hat{a}_{\mathbf{q}}^\dagger + \hat{a}_{-\mathbf{q}}) \quad (3.3a)$$

$$\hat{H}_{ph}^{nd} = \sum_{i \neq j, \mathbf{q}} \left( M_{\mathbf{q}}^{ie,je} \hat{c}_i^\dagger \hat{c}_j - M_{\mathbf{q}}^{ih,jh} \hat{d}_i^\dagger \hat{d}_j \right) (\hat{a}_{\mathbf{q}}^\dagger + \hat{a}_{-\mathbf{q}}) . \quad (3.3b)$$

Here  $\hat{a}_{\mathbf{q}}^\dagger$  and  $\hat{a}_{\mathbf{q}}$  are the time-dependent phonon operators, obeying Bose commutation rules, and the matrix element for deformation potential coupling with acoustic phonons of dispersion  $\omega_{\mathbf{q}} = |\mathbf{q}|s$  is given by

$$M_{\mathbf{q}}^{ic,jc} = D_c \sqrt{\frac{\hbar\omega_{\mathbf{q}}}{2\rho_m V s^2}} \int d\mathbf{r} \exp(i\mathbf{q} \cdot \mathbf{r}) \Phi_i^{c*}(\mathbf{r}) \Phi_j^c(\mathbf{r}), \quad (3.4)$$

being  $s$  the sound velocity,  $\rho_m$  the mass density,  $V$  the normalization volume and  $D_\gamma$  the deformation potential constants (see Tab. 3.1). The diagonal term  $\hat{H}_{ph}^d$  describes the coupling of each isolated electron or hole state with the phonon modes [Krum 02, Zimm 02, Fave 03]. The off-diagonal term  $\hat{H}_{ph}^{nd}$  accounts for the phonon-assisted scattering between different electron or hole states. The independent boson model can be diagonalized exactly in the case of a single electron-hole pair state [Maha 90]. Here however, because of the off-diagonal coupling  $\hat{H}_{ph}^{nd}$  and of the Coulomb interaction, the full diagonalization of the problem is a cumbersome task. The approach that we develop in the next section, consists in diagonalizing the electron Hamiltonian  $\hat{H}_{QD}$  to obtain exciton states that are superposition of electron-hole pair states, and then consistently rewrite in the new basis the two terms of the exciton-phonon Hamiltonian in Eq. (3.3). This is done in the framework of a density matrix approach, so that the diagonalization is performed in a second step, after writing the dynamical equations for the density matrix.

### 3.1.2 Density matrix formalism

Now that the Hamiltonian problem for the exciton-phonon coupling in QD molecules has been stated, we proceed to develop our density matrix formalism for the linear interband polarization. As already mentioned, we do this

in the framework of the second-order Born approximation, without performing the Markov limit. The electron-hole pair creation operators, defined as the two-operator products  $\hat{d}_i^\dagger \hat{c}_j^\dagger$ , and phonon operators evolve according to Heisenberg equations

$$i\hbar \frac{d}{dt} \hat{d}_i^\dagger \hat{c}_j^\dagger = (E_{iv} - E_{jc}) \hat{d}_i^\dagger \hat{c}_j^\dagger + \sum_{lmrs} V_{rs}^{lm} \left( \hat{d}_i^\dagger \hat{c}_l^\dagger \hat{d}_r^\dagger \hat{d}_s \delta_{mj} - \hat{c}_l^\dagger \hat{c}_m \hat{d}_r^\dagger \hat{c}_j^\dagger \delta_{si} \right) + \sum_{k,\mathbf{q}} \left( M_{\mathbf{q}}^{iv,kv} \hat{d}_k^\dagger \hat{c}_j^\dagger - M_{\mathbf{q}}^{kc,jc} \hat{d}_i^\dagger \hat{c}_k^\dagger \right) (\hat{a}_{\mathbf{q}}^\dagger + \hat{a}_{-\mathbf{q}}), \quad (3.5a)$$

$$i\hbar \frac{d}{dt} \hat{a}_{-\mathbf{q}} = \hbar\omega_q \hat{a}_{-\mathbf{q}} - \sum_{i,j} \left( M_{-\mathbf{q}}^{ih,jh} \hat{d}_i^\dagger \hat{d}_j - M_{-\mathbf{q}}^{ie,je} \hat{c}_i^\dagger \hat{c}_j \right), \quad (3.5b)$$

$$i\hbar \frac{d}{dt} \hat{a}_{\mathbf{q}}^\dagger = -\hbar\omega_q \hat{a}_{\mathbf{q}}^\dagger + \sum_{i,j} \left( M_{-\mathbf{q}}^{ih,jh} \hat{d}_i^\dagger \hat{d}_j - M_{-\mathbf{q}}^{ie,je} \hat{c}_i^\dagger \hat{c}_j \right), \quad (3.5c)$$

In Eq. (3.5b) we have used the fact that  $\omega_{-q} = \omega_q$ . From Eqs. (3.5), we derive the evolution equations for the polarizations and the phonon-assisted polarizations, that are defined by

$$P_{ij}(t) = \langle \hat{d}_i^\dagger(t) \hat{c}_j^\dagger(t) \hat{d}_i^\dagger(0) \hat{c}_j^\dagger(0) \rangle, \quad (3.6a)$$

$$P_{ij}^{a-\mathbf{q}}(t) = \langle \hat{d}_i^\dagger(t) \hat{c}_j^\dagger(t) \hat{d}_i^\dagger(0) \hat{c}_j^\dagger(0) \hat{a}_{-\mathbf{q}}(t) \rangle, \quad (3.6b)$$

$$P_{ij}^{a\mathbf{q}}(t) = \langle \hat{d}_i^\dagger(t) \hat{c}_j^\dagger(t) \hat{d}_i^\dagger(0) \hat{c}_j^\dagger(0) \hat{a}_{\mathbf{q}}^\dagger(t) \rangle, \quad (3.6c)$$

where the symbol  $\langle \hat{A} \rangle$  indicates the expectation value of the operator  $\hat{A}$  on the vacuum state. Note that we take into account only polarizations assisted by one phonon operator [Eqs. (3.6b) and (3.6c)], thus neglecting higher order phonon-assisted polarizations. These latter are factored into products of (3.6) and phonon density  $n_q = \langle \hat{a}_{\mathbf{q}}^\dagger \hat{a}_{\mathbf{q}} \rangle$ . Eq. (3.5a) shows that the Coulomb interaction couples the two operator dynamics to four-operator terms. The evolution equations for the latter should be included in the system of Eqs. (3.5) in order to solve it consistently. Nevertheless, the dynamic of four-operator terms is coupled to that of six-operator terms and so on, resulting in an infinite hierarchy of equations. We truncate this hierarchy at the lowest order, by factoring the expectation value of four operator products into all possible combinations leading to products of densities and polarizations. This yields the Hartree-Fock limit of Eqs. (3.5) [Haug 90]. The factorization must be performed on normal ordered product operators (i.e. all the creation operators must be on the left of annihilation operators), and the anticommutation relations must be taken into account in order to get the proper signs between the two-operator combinations [Haug 90]. In particular, the four-operators

terms in Eq. (3.5a) are factored as

$$\begin{aligned}\langle \hat{d}_i^\dagger \hat{c}_l^\dagger \hat{d}_r^\dagger \hat{d}_s \rangle &= \langle \hat{d}_i^\dagger \hat{c}_l^\dagger \rangle \langle \hat{d}_r^\dagger \hat{d}_s \rangle - \langle \hat{d}_i^\dagger \hat{d}_r^\dagger \rangle \langle \hat{c}_l^\dagger \hat{d}_s \rangle + \langle \hat{d}_i^\dagger \hat{d}_s \rangle \langle \hat{c}_l^\dagger \hat{d}_r^\dagger \rangle \\ &= \left[ \langle \hat{d}_i^\dagger \hat{c}_l^\dagger \rangle \delta_{rs} - \langle \hat{d}_r^\dagger \hat{c}_l^\dagger \rangle \delta_{is} \right] n_s^h\end{aligned}\quad (3.7a)$$

$$\begin{aligned}\langle \hat{c}_l^\dagger \hat{c}_m \hat{d}_r^\dagger \hat{c}_j^\dagger \rangle &= \langle \hat{c}_l^\dagger \hat{d}_r^\dagger \hat{c}_j^\dagger \hat{c}_m \rangle - \langle \hat{c}_l^\dagger \hat{d}_r^\dagger \rangle \delta_{im} \\ &= \left[ \langle \hat{d}_r^\dagger \hat{c}_j^\dagger \rangle \delta_{lm} - \langle \hat{d}_r^\dagger \hat{c}_l^\dagger \rangle \delta_{jm} \right] n_m^e + \langle \hat{d}_r^\dagger \hat{c}_l^\dagger \rangle \delta_{jm}\end{aligned}\quad (3.7b)$$

where  $n_i^e$  ( $n_i^h$ ) is the time-dependent electron (hole) density for the  $i$ -th state. Because of the Coulomb terms (3.7), the non-phononic part of the evolution equations for the polarizations in Eqs. (3.6) is non-diagonal. It can be diagonalized by a linear transformation of the electron-hole pair basis into an exciton basis. Then, the phononic part of the equations can be rewritten consistently. However, a difficulty in changing the basis arises from the presence of the time-dependent carrier densities that multiply the polarizations in the Coulomb terms. Here, we restrict to the linear optical response and assume the low density limit  $n_i^e = n_i^h = 0$ , thus neglecting all the Coulomb terms in Eqs. (3.7) except the last one on the right side of Eq. (3.7b), that is  $\langle \hat{d}_r^\dagger \hat{c}_l^\dagger \rangle \delta_{jm}$ . In the new basis, the exciton polarizations are linear combinations of the electron-hole pair polarizations

$$\Pi_\rho(t) = \sum_{ij} \alpha_\rho^{ij} P_{ij}(t), \quad (3.8)$$

and the same holds (with the same coefficients  $\alpha_\rho^{ij}$ ) for the phonon-assisted polarizations. The polarization  $\Pi_\rho(t)$  corresponds to the exciton state with wave function  $\Psi_\rho(\mathbf{r}_e, \mathbf{r}_h) = \sum_{ij} \alpha_\rho^{ij} \Psi_{ij}(\mathbf{r}_e, \mathbf{r}_h)$  and energy  $E_\rho$ , with  $\rho = 1, \dots, 4$ . These energies are plotted in Fig. 3.3.(a) as a function of the interdot distance  $R$ . The energy splitting at short  $R$  is mainly due to conduction electron tunneling between the two QDs, and is scarcely affected by the asymmetry between them and by Coulomb interaction. The Coulomb interaction produces a splitting of the exciton energies, that become important at large values of  $R$ . Moreover, it is responsible for the *anticrossing* of the two highest levels between  $R = 8$  nm and  $R = 9$  nm. The oscillator strength of the  $\rho$ -th exciton state is  $\mu_\rho = |\int d\mathbf{r} \Psi_\rho(\mathbf{r}, \mathbf{r})|$  and the corresponding radiative linewidth is  $\gamma_\rho = \omega_{LT} k_0^3 a_B^3 \mu_\rho^2 / 6$  [Gil 02], being  $\hbar\omega_{LT}$  the LT-splitting for excitons in the bulk material,  $k_0 = 2\pi/\lambda_0$  the wave vector of light at the exciton resonance frequency and  $a_B$  the Bohr radius of the exciton. Radiative linewidths are plotted versus  $R$  in Fig. 3.3.(b). At short distances, where the tunneling exceeds both the Coulomb energy and the asymmetry, the exciton states are well described in terms of electron-hole product-states. Optical active states are formed from symmetric and antisymmetric electron and hole

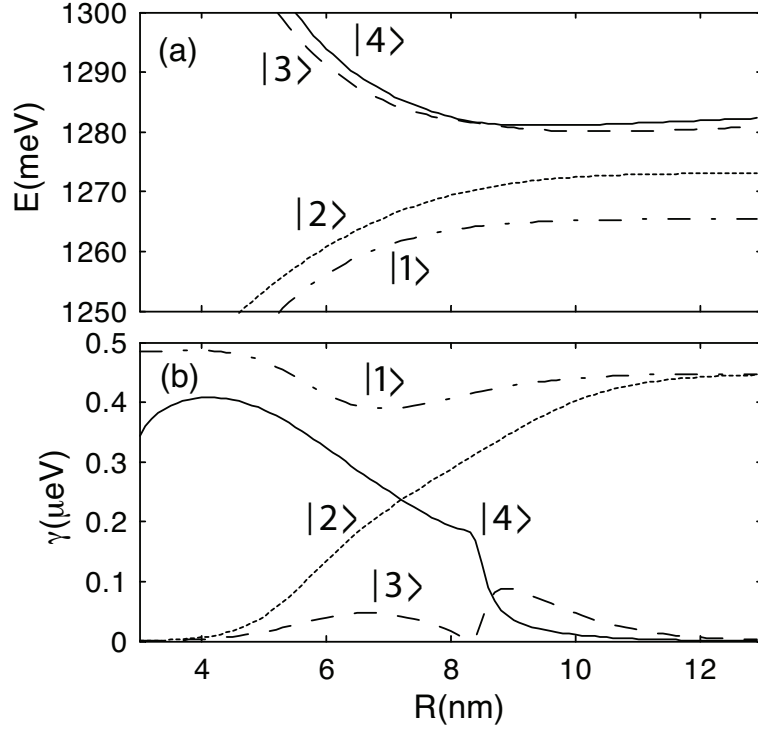


Figure 3.3: Exciton energies (a) and radiative linewidths (b) for an InAs QD molecule, accounting for Coulomb interaction and 2% asymmetry. (a) The Coulomb interaction produce an energy shift and a splitting of the exciton energies. (b) At short distance all the exciton states can be optically active. As  $R$  increase, spatially indirect excitons become dark.

( $|11\rangle$  and  $|22\rangle$  respectively, according to Sec. 1.2) states, while the other two ( $|12\rangle$  and  $|21\rangle$ ) remain dark. As  $R$  increases, the Coulomb interaction mixes these symmetric combinations that become all optically active. In the limit of large  $R$  the carriers are strictly localized in one of the two QDs, and *direct* excitons (i.e., formed by electron and hole both localized on the top or on the bottom QD) of low energy are bright, while *indirect* excitons are dark. Then, while in single QDs the Coulomb interaction results in a small correction to the polarization decay, in QD molecules it affects strongly the exciton wave functions and consequently the exciton-phonon coupling. With the present parameters, the exciton transition energies measured in [Borr 03] are well reproduced. More detailed models of the electronic states [Best 04] show that the actual energy level structure deviates from this simple description, especially with respect to the valence states. The phonon-assisted effect we are modeling, however, depends mainly on exciton-phonon coupling and, due

to the lighter effective mass, almost entirely on the conduction-electron part of this coupling. The hole wave function affects only minimally our results, finally justifying our adoption of a simple effective mass scheme.

The evolution equations for the exciton polarizations and phonon-assisted polarizations read

$$i\hbar \frac{d}{dt} \Pi_\rho(t) = -E_\rho \Pi_\rho(t) + \sum_\sigma \sum_{\mathbf{q}} M_{\mathbf{q}}^{\rho\sigma} \left[ \Pi_\sigma^{a_{\mathbf{q}}^\dagger}(t) + \Pi_\sigma^{a_{-\mathbf{q}}}(t) \right], \quad (3.9a)$$

$$i\hbar \frac{d}{dt} \Pi_\rho^{a_{-\mathbf{q}}}(t) = -(E_\rho - \hbar\omega_q) \Pi_\rho^{a_{-\mathbf{q}}}(t) + \sum_m M_{-\mathbf{q}}^{\rho\sigma} n_q \Pi_\sigma(t), \quad (3.9b)$$

$$i\hbar \frac{d}{dt} \Pi_\rho^{a_{\mathbf{q}}^\dagger}(t) = -(E_\rho + \hbar\omega_q) \Pi_\rho^{a_{\mathbf{q}}^\dagger}(t) + \sum_\sigma M_{-\mathbf{q}}^{\rho\sigma} (1 + n_q) \Pi_\sigma(t), \quad (3.9c)$$

where  $n_q = \langle a_{\mathbf{q}}^\dagger a_{\mathbf{q}} \rangle = [\exp(\beta\hbar\omega_q) - 1]^{-1}$  is the thermal phonon distribution at the lattice temperature, and we have defined

$$M_{\mathbf{q}}^{\rho\sigma} = \sum_{ij} \alpha_{\rho}^{ij} \left[ \sum_k M_{\mathbf{q}}^{iv,kv} \beta_{kj}^{\sigma} - \sum_k M_{\mathbf{q}}^{kc,jc} \beta_{ik}^{\sigma} \right], \quad (3.10)$$

being  $\beta_{\rho}^{ij}$  the coefficients of the inverse transformation with respect to  $\alpha_{ij}^{\rho}$ . Eqs. (3.9) can be solved by Fourier transforming to frequency domain. The sum of phonon-assisted polarizations in the Fourier transformed version of Eq. (3.9a) reads

$$\tilde{\Pi}_{\rho}^{a_{\mathbf{q}}^\dagger}(\omega) + \tilde{\Pi}_{\rho}^{a_{-\mathbf{q}}}(\omega) = \sum_{\sigma} M_{-\mathbf{q}}^{\rho\sigma} D_q^{\rho}(\omega) \tilde{\Pi}_{\sigma}(\omega), \quad (3.11)$$

with the phonon propagator  $D_q^{\rho}(\omega)$  given by [Maha 90]

$$D_q^{\rho}(\omega) = \frac{1 + n_q}{\hbar\omega - E_\rho - \hbar(\omega_q - i\gamma_q)} + \frac{n_q}{\hbar\omega - E_\rho + \hbar(\omega_q + i\gamma_q)}, \quad (3.12)$$

where we have added an imaginary part to the phonon energies  $\hbar\omega_q$ , whose value is fixed to the phenomenological value  $\hbar\gamma_q = 1\mu\text{eV}$ , describing the acoustic phonon damping [Goup 02, Zimm 02]. The final equation describing the  $\omega$ -dependent exciton polarizations reads

$$[E_\rho - \hbar(\omega + i\gamma_\rho)] \tilde{\Pi}_{\rho}(\omega) - \sum_{\sigma} \Sigma_{\rho\sigma}(\omega) \tilde{\Pi}_{\sigma}(\omega) = \mu_{\rho}, \quad (3.13)$$

where  $\gamma_\rho$  is the radiative linewidth of the  $\rho$ -th exciton state,  $\mu_\rho$  its oscillator strength, and the exciton-phonon Born self energy is written in terms of the

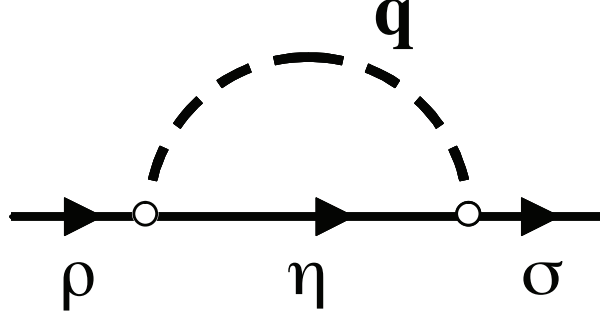


Figure 3.4: Diagram representation of the second order Born (2B) self energy. The arrow denote the exciton propagator, while the dashed line stands for the phonon propagator. Since the interaction appear twice (circles), one speak of 2B-approximation.

exciton-phonon coupling matrix elements and of the exciton propagator as

$$\Sigma_{\rho\sigma}(\omega) = \sum_{\eta, \mathbf{q}} M_{\mathbf{q}}^{\rho\eta} D_{\mathbf{q}}^{\eta}(\omega) M_{-\mathbf{q}}^{\eta\sigma}. \quad (3.14)$$

The self energy matrix is non-diagonal, resulting in cross correlation between exciton states. In particular, it describes processes where an exciton scatters from state  $\rho$  to state  $\sigma$  after having emitted and absorbed a phonon, being  $\eta$  any accessible intermediate state, according to the diagram in Fig. 3.4. The frequency dependence of the self energy in the diagrammatic approach is fully equivalent to the inclusion of memory effects. Then, our non-Markovian formalism is suitable for the description of quantum kinetic effects such as phonon broadband, as we show in the next section.

Before concluding this section, we derive the Markov limit of Eqs. (3.13) and (3.14). Eq. (3.9b) can be formally solved as

$$\begin{aligned} \Pi_{\rho}^{a-\mathbf{q}}(t) &= -\frac{i}{\hbar} \int_{-\infty}^t dt' n_{\mathbf{q}} \sum_{\sigma} M_{-\mathbf{q}}^{\rho\sigma} \Pi_{\sigma}(t') \\ &\times \exp \left[ -\frac{i}{\hbar} (E_{\rho} - \hbar\omega_{\mathbf{q}}) (t - t') \right], \end{aligned} \quad (3.15)$$

and a similar expression holds for the formal solution of Eq. (3.9c). One can assume that the polarization can be factored as  $\Pi_{\rho}(t) = \tilde{\Pi}_{\rho}(t) \exp(-iE_{\rho}t/\hbar)$ , where  $\tilde{\Pi}_{\rho}(t)$  is slowly varying in time. Then, the Markov approximation consists in taking the slow component out of the integral. This corresponds to

neglecting memory effects. Consequently, the temporal dynamics of the propagator reduces to an exponential decay with a constant damping. Eq. (3.15) becomes

$$\Pi_{\rho}^{a-q}(t) = -\frac{i\pi}{\hbar} n_q \sum_{\sigma} M_{-\mathbf{q}}^{\rho\sigma} \Pi_{\sigma}(t) \delta[\hbar\omega_q - (E_{\rho} - E_{\sigma})] , \quad (3.16)$$

where the Cauchy principal part of the integral (i.e. the polaron shift of the ZPL) has been neglected. When Eq. (3.15) and the corresponding expression for  $\Pi_{\rho}^{a\dagger}(t)$  are inserted in Eq. (3.9a), the Markovian self energy reads

$$\Sigma_{\rho\sigma}^M = \frac{i\pi}{\hbar s} \sum_{\eta\mathbf{q}} N_q M_{\mathbf{q}}^{\rho\eta} M_{-\mathbf{q}}^{\eta\sigma} \delta(q - q_{\eta\sigma}) . \quad (3.17)$$

where  $q_{\eta\sigma} = E_{\eta} - E_{\sigma}/\hbar s$  and we have defined  $N_q = n_q$  ( $N_q = n_q + 1$ ) for  $q < 0$  ( $q > 0$ ). The Markov approximation results in a self energy matrix where the frequency dependence is completely dropped. Consequently, Eq. (3.13) reduces to an algebraic set of equations. Nevertheless, the Markov self energy is non-diagonal, thus containing information on the correlation among exciton levels. In the next section we show the results of the numerical solution of Eq. (3.13), both considering memory effects and in the Markov approximation, focusing on the analysis of the exciton dephasing rates.

## 3.2 Results

The formalism developed in the last section allows the description of the phonon broadband and of the broadening of the ZPL that characterize the spectra of exciton resonances in a QD system. In particular, the non-Markovian treatment of the exciton-acoustic phonon coupling in QD molecules describes both the temperature and the interdot distance dependence of these spectral features. A similar analysis has recently been carried out by Mannarini *et al.* [Mann 06] on the system of excitons localized by interface roughness in a quantum well. There, the weaker exciton confinement results in smaller phonon sidebands and mainly the temperature dependence was studied. Here, we focus on the effect of the interdot distance on the exciton-phonon coupling or, in other words, to the phonon-mediated interaction between the two spatially separated quantum systems. All the numerical results shown in the following, are relative at a temperature of  $T = 10$  K.

We numerically solve Eq. (3.13) for the exciton polarizations  $\Pi_{\rho}(\omega)$ . The optical spectrum is related to the imaginary parts of these quantities. Typical exciton spectra of the QD molecule under study are plotted in Fig. 3.5 for

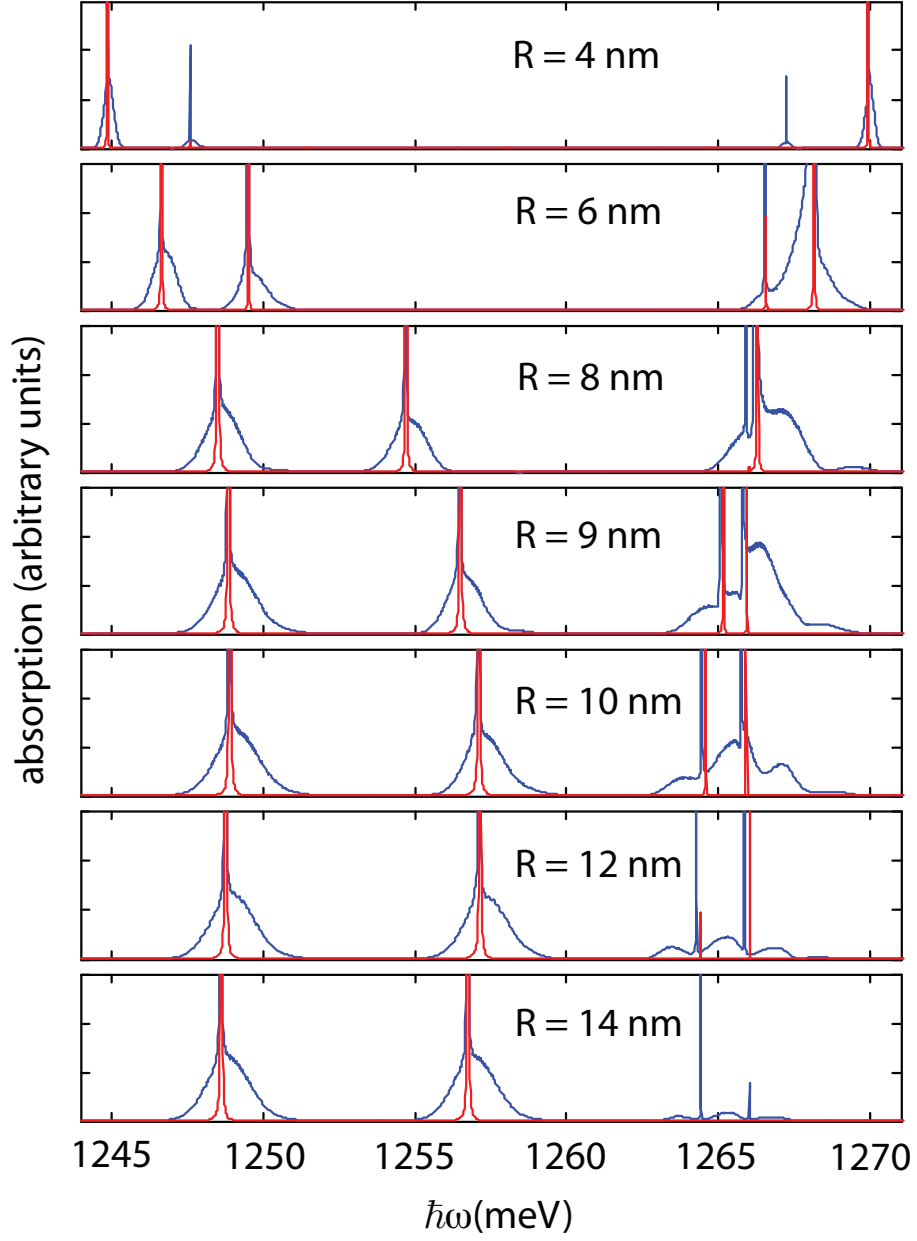


Figure 3.5: Comparison between the non-Markov (blue lines) and Markov (red lines) spectra of an asymmetric QD molecule calculated at  $T = 10$  K for different interdot distances  $R$ . The scale is linear, but the ZPLs are truncated to magnify the phonon sidebands. To get an estimate of the line intensity, one should refer to the oscillator strengths as extracted from Fig. 3.3.

different values of the interdot distance  $R$ . Each peak of the non-Markovian spectra (blue line) is characterized by a narrow ZPL (the peaks of ZPLs are truncated) and phonon sidebands corresponding to phonon absorption (at the left of the ZPL) and emission (at the right). The phonon broadband originate from the diagonal elements  $\Sigma_{\rho\rho}(\omega)$  of the exciton-phonon self-energy in Eq. (3.14), as in the single QD case [Krum 02, Zimm 02]. All four exciton states, however, are coupled to each other via the off-diagonal terms of the exciton-phonon self-energy, resulting in the phonon broadening of the ZPL [Mulj 04, Mulj 05]. The distance dependence of the spectral positions and relative intensity of the ZPL peaks is explained as for Fig. 3.3. Remarkably, in correspondence with the Coulomb anticrossing around  $R = 8$  nm, the ZPL width of the two higher states drops and never restores. This is because for  $R > 8$  nm the two states are indirect excitons, and the exciton-phonon matrix element between them vanishes by symmetry. Thus, real transitions between these states are not allowed any more and their dephasing is due to virtual transitions into the lower states [Mulj 05]. The spectra calculated using the Markov self-energy (3.17) are plotted for comparison (red line), and consist in the simple superposition of Lorentzian lines. Note that the non-Markovian peaks are shifted with respect to the Lorentzian resonances (polaron shift).

The phonon linewidths of the ZPL can be calculated from the imaginary part of the frequency dependent Born self energy in Eq. (3.14), once it is expanded around the exciton pole  $E_\rho$ . This can be done at different levels of approximation. In the so-called *semi-Markov* approximation [Mann 06] one neglects the off-diagonal elements of the self energy matrix, while keeping the frequency dependence, i.e.,  $\Sigma_{\rho\sigma}(\omega) = \delta_{\rho\sigma}\Sigma_{\rho\rho}^{SM}(\omega)$ . This approach is correct as long as the off-diagonal elements are small with respect to the differences between diagonal elements, resulting in linewidths that are in excellent agreement with the full non-Markov calculation in a large range of temperatures [Mann 06]. The approximation is expected to fail in spectral regions with a high density of overlapping states. Nevertheless, this condition is more likely to occur in spatially extended nanostructures, e.g., for exciton states localized in disordered quantum wells. In the Markov approximation the phonon linewidths of the ZPL are calculated at the first order of the self energy expansion, i.e., from the Markov self energy (3.17). Neglecting the non-diagonal terms corresponds to the first order of the semi-Markov approximation, and reproduces Fermi's Golden Rule (FGR) for the phonon-assisted transitions

$$\Gamma_\rho^{FGR} = -\text{Im} \left[ \Sigma_{\rho\rho} \left( \omega = \frac{E_\rho}{\hbar} \right) \right] = \pi \sum_{\sigma\mathbf{q}} N_q |M_{\mathbf{q}}^{\rho\sigma}|^2 \delta(q - q_{\rho\sigma}) . \quad (3.18)$$

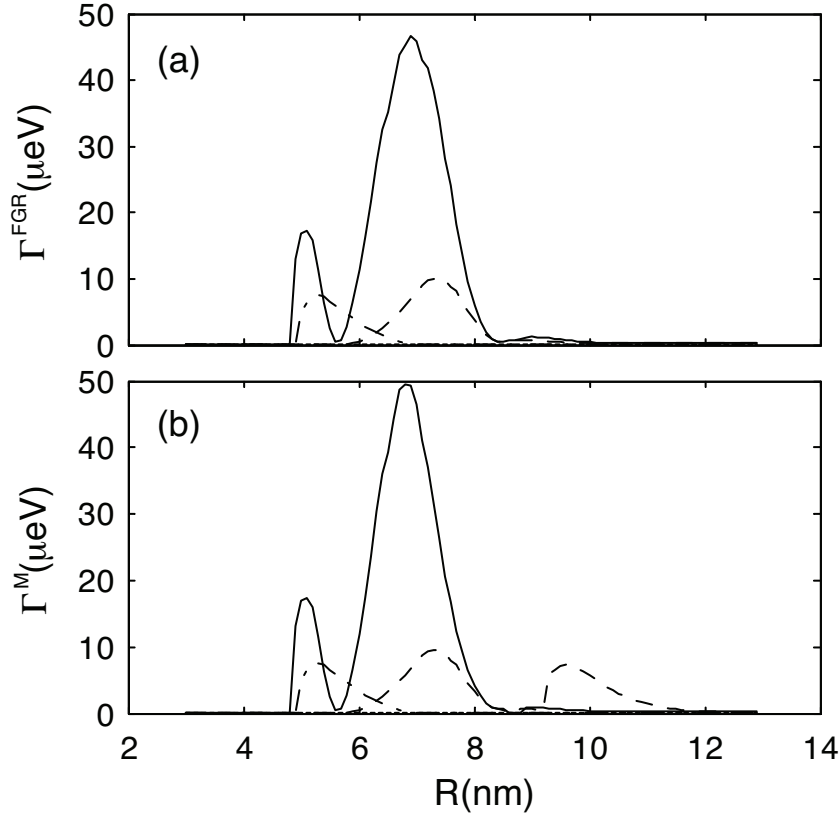


Figure 3.6: Exciton dephasing rates for the QD molecule calculated at  $T = 10$  K. (a) Fermi golden rule. (b) Markov approximation.

The FGR linewidths are broader than those calculated in the semi-Markov approximation and their ratio is  $\Gamma_{\rho}^{\text{FGR}}/\Gamma_{\rho}^{\text{SM}} = 1 + S_{\rho}$  [Mann 06], where  $S_{\rho}$  is the temperature dependent Huang-Rhys factor [Duke 65, Zimm 02]. In Fig. 3.6.(a) we show the dependence on the interdot distance  $R$ , of the FGR exciton linewidths calculated at  $T = 10$  K, where  $S_{\rho}$  is very small. Strong oscillations versus  $R$  are observed and very large values are obtained for the different levels, up to 45  $\mu\text{eV}$  compared to approximately 1  $\mu\text{eV}$  for a single QD. Both oscillations and large dephasing rates result also from a full non-Markov approach using cumulant expansion of the linear polarization [Mulj 05]. Muljarov *et al.* showed that while the phonon broadband is purely a quantum kinetic effect, the deviation of the ZPL from a Lorentzian profile depends strongly on interdot distance (via tunneling), electron-hole Coulomb interaction and asymmetry of the double dot potential. These features are contained in the FGR approximation that is then confirmed to give

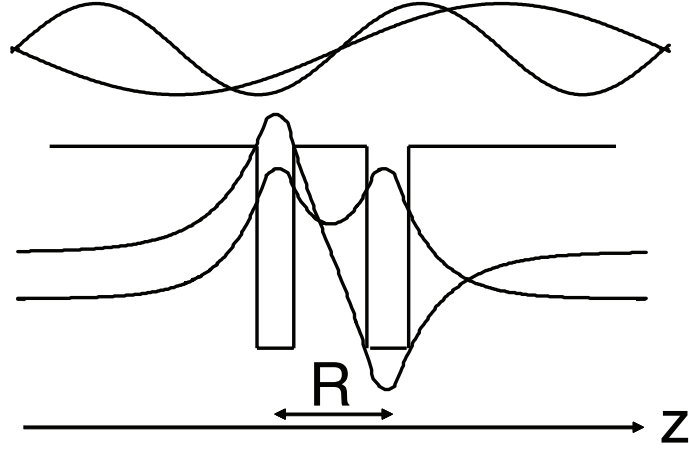


Figure 3.7: The phonon wavelength must be such to restore the parity of the superposition integral in the exciton-phonon coupling matrix.

a suitable description of the ZPL linewidths. Nevertheless, an improvement is expected to come from taking into account the non-diagonal elements of the self-energy matrix, i.e. in the Markov approximation. In this case, the phonon linewidths are calculated as  $\Gamma_{\rho}^M = -\text{Im}[\tilde{\Sigma}_{\rho}(\omega = E_{\rho}/\hbar)]$ , where  $\tilde{\Sigma}_{\rho}(\omega)$  are the eigenvalues of the matrix  $\Sigma_{\rho\sigma}(\omega) - E_{\rho}\delta_{\rho\sigma}$ . The resulting exciton dephasing rates are plotted in Fig. 3.6.(b). The main difference with respect to Fig. 3.6.(a) is a further oscillation of the linewidth of the third exciton state (dashed line) at about  $R = 10$  nm. At this distance the distinction in direct and indirect excitons does not hold yet, as Figs. 3.3.(b) and 3.5 show. The four states are still optically active and therefore this difference is significant for the measurements. The oscillatory dependence from  $R$  could explain the strong dependence measured in [Borr 03] and shown in Fig. 3.2. The measurements of the dephasing time have been performed on double layers of vertically stacked InAs/GaAs QDs with an areal dot density of about  $10^{10} \text{ cm}^{-2}$ . Here, the exciton ground-state transition (0-X) shows a Gaussian inhomogeneous broadening of the transition energy of tens of meV full width at half maximum (FWHM) attributed to fluctuations in dot size and indium concentration. We suggest that the result of the measurement can be interpreted in terms of our single-QD-molecule result, convoluted with the inhomogeneous distribution of QD energies.

The oscillations as a function of the distance can be explained as follows. According to Eqs. (3.4) and (3.10), the matrix elements of the exciton-phonon coupling potential are proportional to the superposition integral between

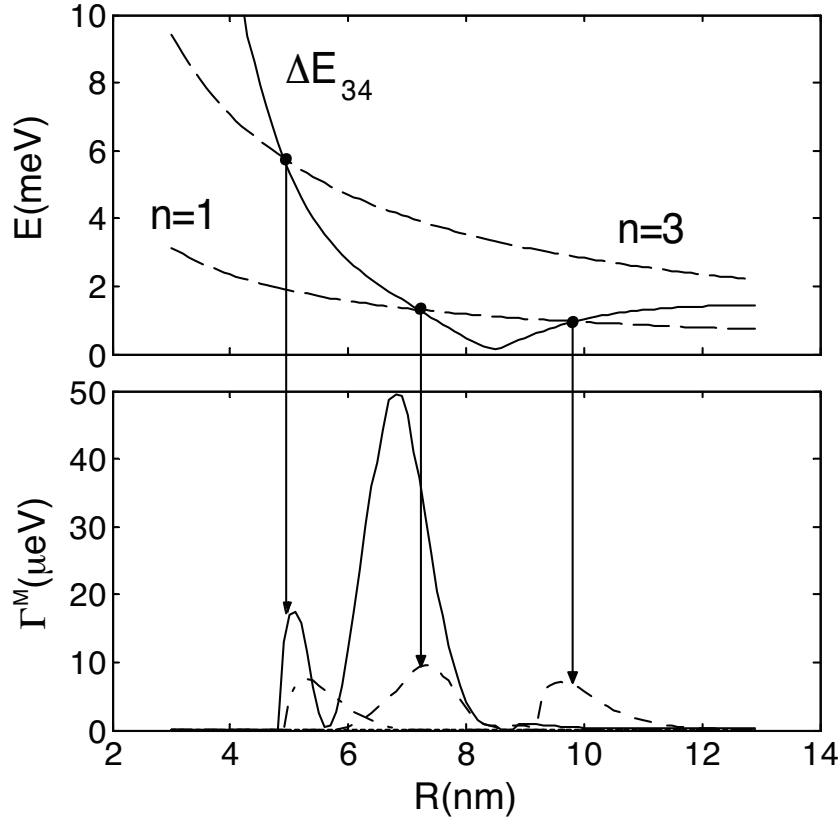


Figure 3.8: Peaks of the linewidths oscillations correspond to the interdot distances that satisfy the matching condition in Eq. (3.19).

exciton states and the phonon wave function along  $z$ . At short distance, the two wave functions have definite parity with respect to  $z = 0$  and the coupling is maximum if the photon wavelength  $\lambda_q = 2\pi/q$  is such that the function in the integral (3.4) has even parity. To fix the idea, if the exciton states have opposite parity as in Fig. 3.7, then the phonon wavelength must satisfy the condition  $R = n\lambda_q/2$ . However, the phonon wavelength must also correspond to the phonon energy that matches the transition between the two levels, i.e.,  $q = q_{\rho\sigma}$ . Putting these two conditions together results in the matching condition

$$\Delta E_{\rho\sigma} = n\pi \frac{\hbar s}{R}, \quad (3.19)$$

that is satisfied only for some values of the distance. This is shown in the upper part of Fig. 3.8, where we plot the energy distance between the two upper exciton levels (solid line) together with the right side of Eq. (3.19) for

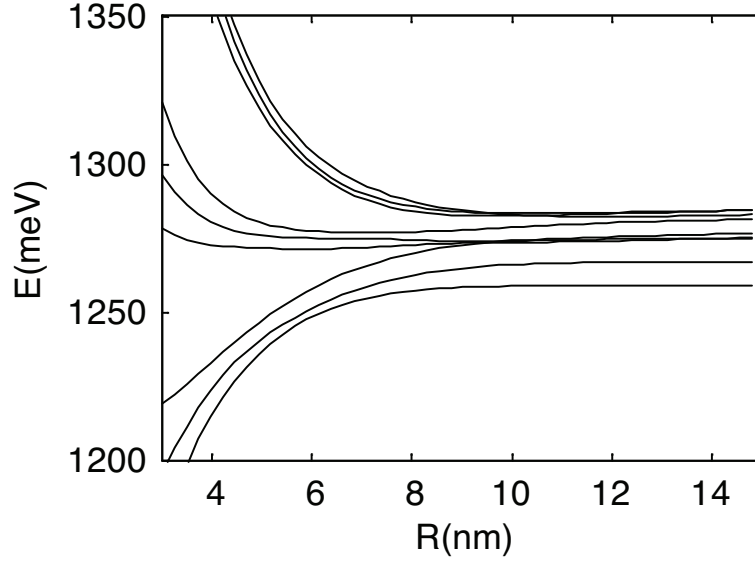


Figure 3.9: Exciton energies for the three-InAs-QD array under study, accounting for Coulomb interaction and asymmetry.

two values of  $n$  (dashed lines). The matching condition (3.19) is fulfilled at the crossing points (circles) that correspond to the peaks in the calculated linewidths. On the other hand, the polarization dephasing is suppressed in correspondence of the minima. Nevertheless, as the oscillations are very broad, the suppression is realized for well defined values of  $R$  that, furthermore, are very unlikely to be the same for the different exciton transitions of the many-QD system.

To conclude our analysis, we have studied the case of an array of three vertically stacked and equally spaced QDs. As usual, we account for the fluctuations of size, shape and components concentration from dot to dot, that are typical of self assembled QDs, by assuming that the confining potentials for the carriers in the bottom QD are 2% (4%) deeper than in the middle (top) QD. The energy levels of the three-QD system are plotted in Fig. 3.9 as a function of the interdot distance  $R$ . In Fig. 3.10 we show the calculated phonon linewidths  $\Gamma_{\rho}^M$  for the nine exciton states of this system. In this case, the exciton dephasing rates are even larger than in the case of a two-QD molecule, with values up to  $125 \mu\text{eV}$  (the corresponding oscillation maxima are truncated, for a better comparison with Fig. 3.6). In fact, because of the larger number of energetically close exciton states available, the probability for exciton-phonon scattering processes is increased and the phonon coupling is more effective. On the other hand, the exciton levels

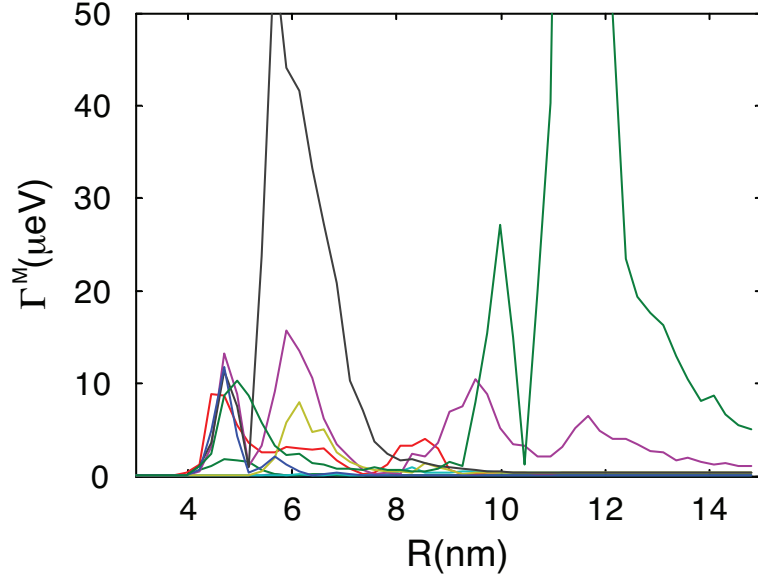


Figure 3.10: Exciton dephasing rates for a three-QD-array calculated in the Markov approximation, at  $T = 10$  K. The energy scale is the same of Fig. 3.6, in order to appreciate the difference between the two- and three-QDs case. The truncated oscillations of the black and green curve reach the maxima at  $55 \mu\text{eV}$  and  $125 \mu\text{eV}$ , respectively.

are spaced unevenly in energy and the simultaneous matching of the phonon wavelength and frequency (3.19), previously described, is consequently made easier for most values of the interdot distance  $R$ . Then, the dephasing of the quantum state is faster than in the two-QDs case, while the oscillations of the dephasing rates versus interdot distance are less dramatic, with the minima occurring at larger values of the rate.

On the basis of our results, the idea of exploiting the dephasing suppression mechanisms proposed in [Zana 98, Bert 04] in order to realize semiconductor-based quantum gates turns out to be oversimplified. In particular, in [Zana 98] the geometrical and chemical inhomogeneities of arrays of many QDs have been completely neglected. While an ideal periodicity would strongly suppress the exciton-phonon scattering, these asymmetries are expected to result in an increased rate of the polarization dephasing.

### 3.3 Conclusions

We have modeled the optical response of excitons in QDs, including the coupling to acoustic phonons in the second order Born approximation, beyond the Markov limit. Two effects, absent in the single QD case, dominate here the ZPL broadening. The first is the off-diagonal phonon-assisted coupling which produces a spectral broadening of the ZPLs significantly larger than the radiative linewidth. In terms of this mechanism we interpret the broad linewidths experimentally measured [Borr 03] in QD molecules. The second is the phonon scattering to dark states which is enhanced when the phonon wavelength matches the interdot distance. This matching condition results in an oscillatory behavior of the exciton dephasing rates in terms of which we explain the strong distance dependence of the ZPL widths measured in QD molecules by Borri *et al.* [Borr 03]. The polarization dephasing is suppressed in correspondence of the minima of the oscillations but, as the oscillations are very broad, the suppression is realized for well defined values of  $R$  only. Furthermore, these values of  $R$  depend strongly on physical parameters that determine the energy structure of the single QDs in the array, such as shape, size and relative concentration of components, that can be controlled in the growth process only to a limited extent. Then, this mechanism of decoherence suppression is not sufficiently effective to be exploited in the realization of quantum gates based on arrays of quantum dots as proposed in [Zana 98, Bert 04] on the basis of the oversimplified picture of the QD as a macroatom.

## Chapter 4

# Coherent coupling of localized exciton transitions

Nonlinear optical spectroscopy is a powerful technique to investigate the electronic structure in semiconductors. The Coulomb correlation between quasiparticles dominate the nonlinear optical response, giving rise to multi-exciton complexes. In particular, the exciton resonances dominate the optical properties of direct-gap semiconductors near the fundamental gap at low temperature [Haug 90, Chem 01]. The dynamical response of a semiconductor following excitation by an ultrafast laser pulse can be conveniently divided into coherent and incoherent regimes. The Coulomb interaction between excitons is best investigated by studying the coherent response. The latter, corresponding to the polarization of the medium, is probed in time-resolved coherent wave-mixing experiments. In particular, four-wave-mixing (FWM) experiments probe the third-order non-linear optical response given by the susceptibility tensor  $\hat{\chi}^{(3)}$ . When intense fields are used, the same excitation scheme can be also used to observe and drive optical Rabi oscillations (RO) of the population inversion in both extended [Cund 94, Quoc 98, Schu 99] and confined [Kama 01, Borr 02, Htoo 02, Zren 02, Li 03, Patt 05] systems. RO are a well-understood phenomenon in two-level spin and atomic systems. Under a strong, resonant, coherent excitation field, the population of the excited state goes through an oscillation as a function of pulse area  $\Theta(t)$ , which is defined as  $\Theta(t) = (\boldsymbol{\mu} \cdot \boldsymbol{\varepsilon}/\hbar) \int_{-\infty}^t E(t') dt'$ , where  $\boldsymbol{\mu}$  is the electric dipole moment of the transition and  $E(t)$  is the amplitude of the electric field, whose polarization vector is  $\boldsymbol{\varepsilon}$ . RO have been observed and characterized in the exciton ground-state transition of several QD ensembles [Kama 01, Htoo 02, Borr 02]. The inversion of the two-level QD-system can be induced via optical pumping of the sample [Zren 02, Patt 05]. The time-resolved state polarization is coherently controlled in both amplitude

and phase [Patt 05]. The coherent optical control of a transition is of specific interest for its application in quantum computation. As an example, in Ref. [Li 03] a single GaAs QD, for which RO between the exciton and biexciton state is demonstrated, is proposed as a two-quantum-bit system involving the crystal ground state  $|00\rangle$ , two distinguishable exciton states with orthogonal polarization  $|01\rangle$  and  $|10\rangle$ , and the biexciton state  $|11\rangle$ . A  $\Theta = \pi$  pulse tuned to the transition  $|10\rangle \leftrightarrow |11\rangle$  serve as the operational pulse of a CROT gate<sup>1</sup>, leaving unchanged the input of the gate if it is  $|00\rangle$  (the operational pulse is off-resonant) or  $|01\rangle$  (the operational pulse have wrong polarization) while Rabi flipping the population of the biexciton level between the states  $|10\rangle$  and  $|11\rangle$ .

Because of the strong similarities between coherent optical excitation of a resonant system and nuclear magnetic resonance (NMR), the concepts of multi-dimensional NMR spectroscopy have recently been adapted to the optical regime to study vibrational [Hybl 01] and electronic [Brix 05] excitations in molecules. This technique enables to determine coherent coupling between the resonances present in the system. Then, two-dimensional (2D) Fourier transform spectroscopy have been used to study many-body interactions in semiconductors [Borc 05, Li 06]. This enhanced FWM technique monitors and correlates nonlinear polarization phase evolution during two independent time periods,  $\tau$  and  $t$ , separated by a mixing time  $T$  ( $T = 0$  in a two-pulse experiment). A 2D spectrum as a function of the absorption frequency ( $\omega_1$ ) and emission frequency ( $\omega$ ) is then obtained by Fourier transforming the FWM signal with respect to the time variables  $\tau$  and  $t$ . Such a 2D spectrum can identify couplings among resonances, separate quantum mechanical pathways, and distinguish among microscopic mechanisms for the many-body interaction by providing previously inaccessible phase informations in semiconductors [Borc 05]. In particular, coherent coupling between different resonances is identified by off-diagonal signals in the two-dimensional spectrally-resolved FWM, as will be explained in the next section. Up to now, wave-mixing experiments were limited to the study of large ensembles of the quantum systems under investigation, due to reasons of both signal strength and directional selectivity. Recently, a novel implementation of transient nonlinear microscopy has been developed [Lang 06, Lang 07], that is called heterodyne spectral interferometry (HSI). This technique opens the possibility of investigating microscopic samples of subwavelength size, as is the case for most individual quantum systems.

The Chapter is organized as follows. In Sec. 4.1, we give a brief schematic

---

<sup>1</sup>A CROT gate, similarly to the standard CNOT gate, can be used as the elementary building block of quantum information devices [Macc 00, Bouw 00].

overview of the FWM and HSI techniques, explaining how the coherent exciton coupling manifests in the measured spectra. In Sec. 4.2 we develop a density matrix formalism in order to model the light-matter interaction in the HSI experimental configuration. A comparison between our results and experimental observations is given in Sec. 4.3, and some concluding remarks are presented in Sec. 4.4.

## 4.1 Four-wave-mixing and heterodyne spectral interferometry

The generic experimental configuration for time-resolved nonlinear optical experiments is shown in Fig. 4.1. A weak laser pulse  $E_1(t)$  propagating along the direction  $\mathbf{k}_1$  excites the sample at  $t = 0$ . Alone, this pulse would probe the linear properties of the sample, and hence it is called the probe pulse. A second laser pulse (pump pulse)  $E_2(t)$  propagating along  $\mathbf{k}_2$ , is delayed and excites the sample at  $t = \tau_d$ . Because of the nonlinearities in semiconductors the response of the sample to the total field is not the sum of the responses to each field. In general, two types of measurements can be performed, namely pump-probe and coherent wave-mixing experiments. Pump-probe experiments investigate both the polarization (coherent) and the population (incoherent) dynamic. The small changes in sample transmission, seen by the probe pulse and induced by the pump pulse ( $\tau_d < 0$ ), are measured. In the weak signal regime, the differential transmission spectrum reproduces the changes in the absorption spectrum of the sample induced by the second field. It can be measured for a series of time delays  $\tau_d$ . In wave-mixing experiments, the two fields coherently interfere in the sample and generate polarization waves emitting photons in background-free and momentum-conserving directions (the phase is conserved in a coherent process).

The polarization response function  $R(\tau, t)$  of the medium can be developed into different orders in the total excitation field. The  $n$ -th order component  $R^n(\tau, t)$  is a sum of contributions of different orders in the fields  $E_{1,2}$  proportional to the product  $R^{(\mathbf{n})} \propto E_1^{n_1} E_1^{m_1*} E_2^{n_2} E_2^{m_2*}$  with  $\mathbf{n} = (n_1, m_1, n_2, m_2)$  and  $n = n_1 + m_1 + n_2 + m_2$ , and is emitted in the direction  $l_1 \mathbf{k}_1 + l_2 \mathbf{k}_2$  with  $l_1 = n_1 - m_1$  and  $l_2 = n_2 - m_2$ . In particular, at the third order in the laser fields, photons are emitted in the direction  $\mathbf{k} = 2\mathbf{k}_2 - \mathbf{k}_1$ . Because of the minimum number of photons involved in this process, the experiment is called four-wave-mixing (FWM). For subwavelength-sized media, the broken translational invariance prohibits the use of wave vector selection. Neverthe-

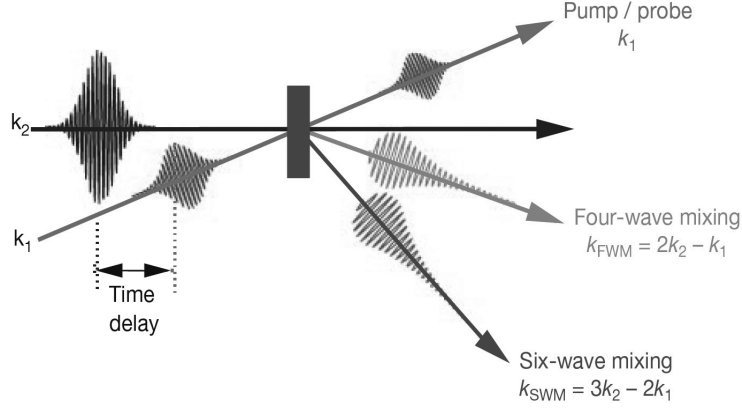


Figure 4.1: Schematic of a generic time-resolved nonlinear optical experiment (from [Chem 01]).

less, with the introduction of the heterodyne spectral interferometry (HSI) technique, is now possible to perform FWM measurements on individual, localized excitons [Lang 06, Patt 06]. The HSI is a technique that joins together FMW spectroscopy and heterodyne detection, giving access to the amplitude and phase of the third-order nonlinear response. In particular, the response function  $R(\tau, t)$  is measured several times, for varying the phases  $\phi_{1,2}$  of the two input pulses  $E_{1,2} \propto e^{i\phi_{1,2}}$ . The Fourier transform versus  $\phi_{1,2}$  allows to select the  $n$ -th order response  $R^n(\tau, t)$ . More specifically, the quantity  $R^{l_1, l_2} = \int d\phi_1 d\phi_2 R(\phi_1, \phi_2) \exp(-il_1\phi_1 - il_2\phi_2)$  is the sum of all  $R^{(\mathbf{n})}$  with equal  $l_1, l_2$ . By measuring the dependence of  $R^{l_1, l_2}$  on the input fields amplitudes, the different contributions  $R^{(\mathbf{n})}$  can be finally extracted. In particular, the FWM signal has  $\mathbf{n} = (0, 1, 2, 0)$ ,  $l_1 = -1$ ,  $l_2 = 2$  and depends on  $|E_1||E_2|^2$ . The evidence of coherent coupling between exciton states is obtained by analyzing the two-dimensional Fourier transform  $R^{-1,2}(\omega_1, \omega)$  of the FWM signal. Two coupled excitons, for example, can be cast into a four-level system consisting of the ground state, the new exciton eigenstates including the interaction, and the biexciton. In such a system, the resonances of the two-dimensional response  $R^{-1,2}(\omega_1, \omega)$  in  $\omega$  can be different from the resonances in  $\omega_1$ . In general, in a multi-level system with transition frequencies  $\omega_k$  and dipole moments  $\mu_k$ , the third order response for positive delay times can be written as [Lang 07]

$$R^{(0,-1,2,0)}(\tau, t) \propto \sum_{k \in X} \mu_k \exp(-i\omega_k \tau) \left( \sum_l \mu_l A_{kl} \exp(i\omega_l t) \right), \quad (4.1)$$

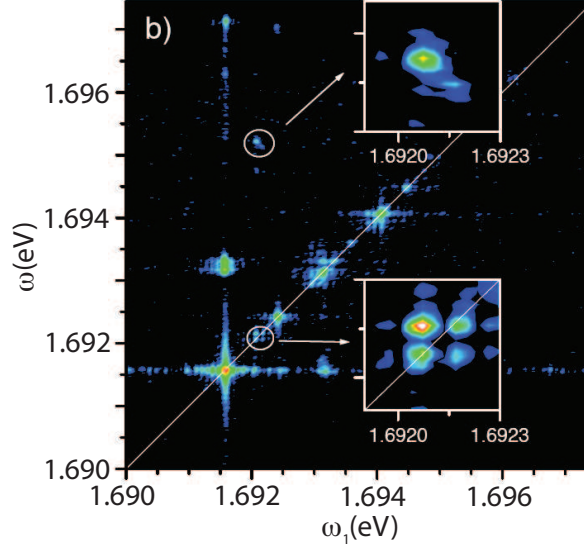


Figure 4.2:  $|R^{-1,2}(\omega_1, \omega)|^2$  derived from 2D-FWM measurements of exciton resonances localized in monolayer islands of GaAs/AlAs quantum wells. Logarithmic color scale over 3.5 orders of magnitude. Co-circular excitation polarization  $\sigma^+$  were used for pump, probe and detection. The insets show magnifications of a finestructure-split exciton (bottom) and the coupled unbound biexciton (top). Off-diagonal signals (bottom) indicate coherent coupling of the exciton states (from [Lang 07]).

where the sum runs over all exciton transitions that are active in first order. Eq. (4.1) is obtained within a simplified model in which the levels have spectral function  $A(\omega) = \delta(\omega)$ , that corresponds to neglect damping, and infinitely short excitation pulses are assumed  $E(t) = \delta(t)$ , which have spectrally flat amplitude.  $A_{kl}$  describes the amplitude of polarization transfer from the transition  $k$  (first-order resonance) to the transition  $l$  (third-order resonance). In general, the matrix  $A_{kl}$  models all the coherent excitation transfer mechanisms, such as FRET and radiative transfer that have been described in Chapter 2, and can depend on time and frequency. Two-dimensional Fourier transform of Eq. (4.1) gives

$$R^{(0,-1,2,0)}(\omega_1, \omega) \propto \sum_{k \in X} \mu_k \delta(\omega_1 + \omega_k) \left( \sum_l \mu_l A_{kl} \delta(\omega - \omega_l) \right). \quad (4.2)$$

For uncoupled two-level systems,  $A_{kl} = \delta_{kl} \mu_k \mu_l$ , so that only peaks along  $\omega_1 = \omega$  are present. Coupled transitions  $k \neq l$  instead create diagonal and off-diagonal peaks at  $(\omega_1, \omega) = (\omega_k, \omega_l)$ , whose amplitudes are still

given by  $A_{kl} = \mu_k \mu_l$ , provided that the coupling energy is larger than the linewidth [Lang 07]). In Fig. 4.2 we report a 2D-spectrum measured in [Lang 07], on excitons localized in monolayer islands of GaAs/AlAs quantum wells. The FWM spectrum is dominated by diagonal resonances, but off-diagonal peaks are also present, evidencing the coherent coupling between the involved exciton states. In the third-order regime, the off-diagonal peaks of two first-order resonances on both sides of the diagonal are expected to be equal in intensity, while in the experimental data the intensities are different, being stronger for  $\omega_1 < \omega$ . The authors propose that this can be related to higher-order contributions (e.g., all possible fifth order contributions with  $n = 5$ ,  $l_1 = -1$  and  $l_2 = 2$ ). Here, we wish to develop a simple multilevel model of excitons and biexcitons in QDs, in order to study the non-linear response to all orders in terms of 2-D spectroscopy. We will show how the basic physics of Eq. (4.2) is recovered and what are the effects of higher-order non-linearities.

## 4.2 Formulation of the model

In this section we develop a density matrix formalism that describes the physics underlying the experimental (HSI) outcomes, that have been presented in the last section. The physical quantity of interest is the nonlinear polarization emitted from a quantum system in which individual, localized resonances are coherently coupled. Some of the most common coupling mechanisms have been addressed in the previous chapters of this thesis. In Chapter 2 we have studied the coupling via the near-field of the optical polarization (Förster coupling) and the long-range radiative coupling related to the retarded contribution to the electromagnetic field, while in Chapter 3 we have addressed the coupling via vibrational modes of the crystal (exciton-phonon coupling). We have seen that the study of these coupling mechanisms is very demanding. Nevertheless, the focus of this chapter is not the coupling mechanism itself, but the way in which it is evidenced via light-matter interaction. Then, our model quantum system will consist of electronic levels coherently coupled only via Coulomb and exchange interaction. Such a coupling mechanism includes the instantaneous limit of the radiative coupling, namely the FRET, but not the radiative corrections at long distance, as discussed in Chapter 2. Our model also doesn't include the phonon coupling. Nevertheless, as stated in the introduction to the present Chapter, the nonlinear optical response of semiconductors is dominated by the Coulomb correlation. Therefore, the inclusion of Coulomb correlation in our theoretical model is needed to obtain a consistent interpretation of the experimental observations, while adding other coupling mechanisms only

serve to study their specific manifestation in this kind of spectroscopy.

Our density matrix formalism is applicable to a QD system of arbitrary number of exciton and biexciton resonances. In Sec. 4.3 we will show results relative to two specific QD systems, namely a single-QD and to a two vertically-stacked QD system. The geometry and the electronic structure of these systems are described in Sec. 1.2. In our model, a single QD has only two exciton levels, that are degenerate in energy if the dot has in-plane circular symmetry. In this case no spectral signature of coupling would be observed, as explained in the previous section. By considering an anisotropic QD, we get two exciton levels that are LT-splitting via exchange interaction, as we have shown in Sec. 2.3.1. On the other hand, in systems of two or more QDs, exciton states of distinct energy and oscillator strength are realized also in the cylindrical symmetry.

### 4.2.1 Hamiltonian and density matrix approach

The Hamiltonian that describes the QD system in interaction with the excitation electric field is

$$\hat{H} = \hat{H}_{QD} + \hat{H}_{e-m}. \quad (4.3)$$

where  $\hat{H}_{QD}$  describes the electronic structure of the QD system and  $H_{e-m}$  accounts for the carrier-light interaction. We describe electrons and holes by the Fermi operators  $\hat{c}_{i\sigma}^\dagger$  and  $\hat{d}_{i\sigma}^\dagger$  ( $\hat{c}_{i\sigma}$  and  $\hat{d}_{i\sigma}$ ) respectively, which create (annihilate) a carrier with energy  $\hbar\omega_i^{e/h}$  and spin  $\sigma = \uparrow$  or  $\sigma = \downarrow$ . We assume as usual (see Sec. 1.2) that the topmost valence states are heavy hole states, which is typical for GaAs-type materials. Then, the annihilator operator  $\hat{d}_{i\uparrow}$  ( $\hat{d}_{i\downarrow}$ ) corresponds to the heavy hole state with angular momentum component  $m_j = 3/2$  ( $m_j = -3/2$ ). The dot Hamiltonian can be written as the sum of two terms  $\hat{H}_{QD} = \hat{H}_0 + \hat{H}_c$ , that read

$$\hat{H}_0 = \sum_{i\sigma} \left( \hbar\omega_i^e \hat{c}_{i\sigma}^\dagger \hat{c}_{i\sigma} - \hbar\omega_i^h \hat{d}_{i\sigma}^\dagger \hat{d}_{i\sigma} \right), \quad (4.4a)$$

$$\begin{aligned} \hat{H}_c = & \frac{1}{2} \sum_{ijlm} \sum_{\sigma\sigma'} \left( V_{ijlm}^{ee} \hat{c}_{i\sigma}^\dagger \hat{c}_{j\sigma} \hat{c}_{l\sigma'}^\dagger \hat{c}_{m\sigma'} + V_{ijlm}^{hh} \hat{d}_{i\sigma}^\dagger \hat{d}_{j\sigma} \hat{d}_{l\sigma'}^\dagger \hat{d}_{m\sigma'} \right. \\ & \left. - 2V_{ijlm}^{eh} \hat{c}_{i\sigma}^\dagger \hat{c}_{j\sigma} \hat{d}_{l\sigma'}^\dagger \hat{d}_{m\sigma'} + 2V_{ijlm,\sigma\sigma'}^{ex} \hat{c}_{i\sigma}^\dagger \hat{d}_{j\sigma} \hat{d}_{l\sigma'}^\dagger \hat{c}_{m\sigma'} \right). \end{aligned} \quad (4.4b)$$

Term (4.4.a) accounts for the single-particle band energies, while (4.4.b) is the Coulomb interaction between the carriers in the QD system. The four terms in Eq. (4.4.b) describe the repulsion between electrons and between holes, the electron-hole attraction, and the exchange interaction, respectively.

The explicit expression of the direct and exchange Coulomb matrix elements is given in Eq. 1.33. In the rotating wave approximation, the dipole coupling to the light field is

$$\hat{H}_{e-m} = -\mathbf{E}^* \cdot \hat{\mathbf{P}} + h.c., \quad (4.5)$$

where the interband polarization of the QD system is given by

$$\hat{\mathbf{P}} = -\sum_{ij} \mu_{ij}^* \left( \hat{c}_{i\downarrow} \hat{d}_{j\downarrow} \mathbf{e}_{\sigma^+} + \hat{c}_{i\uparrow} \hat{d}_{j\uparrow} \mathbf{e}_{\sigma^-} \right). \quad (4.6)$$

Here,  $\mu_{ij}$  is the dipole matrix element of the interband optical transition and  $\mathbf{e}_{\sigma^\pm}$  is the unit polarization vector with circular  $\sigma^\pm$  polarization. Using Eq. (4.6), the light-matter interaction Hamiltonian (4.5) finally reads

$$\hat{H}_{e-m} = -\hbar \sum_{ij} \left[ \Omega_{ij,\sigma^+}^* \hat{c}_{i\downarrow} \hat{d}_{j\downarrow} \mathbf{e}_{\sigma^+} + \Omega_{ij,\sigma^-}^* \hat{c}_{i\uparrow} \hat{d}_{j\uparrow} \mathbf{e}_{\sigma^-} + h.c. \right], \quad (4.7)$$

where  $\Omega_{ij\sigma^\pm} = \mu_{ij} E_{\sigma^\pm} / \hbar$  is the Rabi frequency of the dipole transition to the single pair state  $\hat{c}_{i\sigma^\pm}^\dagger \hat{d}_{j\sigma^\pm}^\dagger |0\rangle$ , being  $E_{\sigma^\pm}$  the  $\sigma^\pm$  component of the laser field amplitude. Eq. (4.7) implements the usual selection rule that  $\sigma^+$  ( $\sigma^-$ ) light couples the  $m_j = -3/2$  ( $m_j = 3/2$ ) valence band to the spin down (up) conduction band state [Axt 05]. It is straightforward to verify that the dark electron-hole pair states  $\hat{c}_{i\downarrow}^\dagger \hat{d}_{j\uparrow}^\dagger |0\rangle$  and  $\hat{c}_{i\uparrow}^\dagger \hat{d}_{j\downarrow}^\dagger |0\rangle$  are not coupled by the Hamiltonian in Eq. (4.3) to other electronic states and thus will be not considered any further. Then, the basis of our Hilbert space is made of the ground state  $|0\rangle$ , electron-hole pair states  $\hat{c}_{i\sigma}^\dagger \hat{d}_{j\sigma}^\dagger |0\rangle$  and two-pair states  $\hat{c}_{i\sigma}^\dagger \hat{d}_{j\sigma}^\dagger \hat{c}_{l\sigma'}^\dagger \hat{d}_{m\sigma'}^\dagger |0\rangle$ . According to Pauli exclusion principle, two-pair states with  $\sigma = \sigma'$  exist only for  $i \neq l$  and  $j \neq m$ . It is advantageous to introduce the eigenstates  $|\nu\rangle$  of  $\hat{H}_{QD}$  and use it as new electronic basis (in particular,  $\nu = 1$  corresponds to the ground state). In the following we will refer to these states as exciton and biexciton states, also if, as explained in Sec. 1.2, the Coulomb correlation that is responsible of the formation of these many-particle states is correctly taken into account only by diagonalizing the Coulomb interaction over a Hilbert space much larger than the one that we consider. In the new basis our model Hamiltonian (4.3) reads

$$\hat{H} = \sum_{\nu} \hbar \omega_{\nu} |\nu\rangle \langle \nu| - \sum_{\nu\nu'} \hbar \Theta_{\nu\nu'} |\nu\rangle \langle \nu'| \quad (4.8)$$

where  $\hat{\Theta} = \hat{S} \hat{\Omega} \hat{S}^\dagger$ , the  $\hat{S}$  matrix providing the transformation between the two basis sets. The density matrix operator  $\hat{\rho}$  of the system under study, is defined by its components  $\hat{\rho}_{\nu\nu'} = |\nu\rangle \langle \nu'|$ , and it evolves in time according to

the equation  $i\hbar\partial_t\hat{\rho} = [\hat{H}, \hat{\rho}]$ . The expectation values  $\rho_{\nu\nu'} = \langle \Psi(t) | \hat{\rho}_{\nu\nu'} | \Psi(t) \rangle$  of the non-diagonal and diagonal components of the density matrix operator on the state of the system are polarizations and densities, respectively. Using Hamiltonian (4.8), the time evolution of these quantities is given by

$$\dot{\rho}_{\nu\nu'} = -i(\omega_\nu - \omega_{\nu'})\rho_{\nu\nu'} - i \sum_{\mu} (\rho_{\nu\mu}\Theta_{\mu\nu'}^* - \Theta_{\nu\mu}^*\rho_{\mu\nu'}) . \quad (4.9)$$

Our model Hamiltonian (4.8) does not take into account the influence of coupling to a reservoir. A more realistic description of the dynamic should include damping terms and, for consistence, noise operators that produce fluctuations, according to the Heisenberg-Langevin approach [Mand 95]. The latter is particularly suitable for the calculation of two-time correlation functions of the system operator as is, for example, required for the determination of the natural linewidth of a laser. In the present case, we include phenomenological damping terms for polarizations and densities in the dynamical Eqs. (4.9). We assume that all the polarization have the same constant decay rate  $\gamma_2$ , while the exciton densities decay with  $\gamma_1 = 2\gamma_2$ , thus neglecting pure dephasing mechanisms. The decay rate of the biexciton densities is instead fixed to a value  $\gamma'_1$  slightly larger than  $\gamma_1$  [Lang 00]. By defining

$$\tilde{\rho}_{\nu\nu'} = \rho_{\nu\nu'} \exp[i(\omega_\nu - \omega_{\nu'})t] , \quad (4.10a)$$

$$\tilde{\Theta}_{\nu\nu'} = \Theta_{\nu\nu'}^* \exp[i(\omega_\nu - \omega_{\nu'})t] , \quad (4.10b)$$

as quantities slowly varying in time, Eqs. (4.9) take the form

$$\dot{\tilde{\rho}}_{\nu\nu'}|_{\nu \neq \nu'} = -\gamma_2 \tilde{\rho}_{\nu\nu'} - i \left[ (\tilde{\rho} \cdot \tilde{\Theta}) - (\tilde{\Theta} \cdot \tilde{\rho}) \right]_{\nu\nu'} , \quad (4.11a)$$

$$\dot{\tilde{\rho}}_{\nu\nu}|_{\nu \in BX} = -\gamma'_1 \tilde{\rho}_{\nu\nu} - i \left[ (\tilde{\rho} \cdot \tilde{\Theta}) - (\tilde{\Theta} \cdot \tilde{\rho}) \right]_{\nu\nu} , \quad (4.11b)$$

$$\dot{\tilde{\rho}}_{\nu\nu}|_{\nu \in X} = -\gamma_1 \tilde{\rho}_{\nu\nu} + \frac{\gamma'_1}{N_X} \sum_{\mu \in BX} \tilde{\rho}_{\mu\mu} - i \left[ (\tilde{\rho} \cdot \tilde{\Theta}) - (\tilde{\Theta} \cdot \tilde{\rho}) \right]_{\nu\nu} \quad (4.11c)$$

$$\dot{\tilde{\rho}}_{11} = \gamma_1 \sum_{\mu \in X} \tilde{\rho}_{\mu\mu} - i \left[ (\tilde{\rho} \cdot \tilde{\Theta}) - (\tilde{\Theta} \cdot \tilde{\rho}) \right]_{11} , \quad (4.11d)$$

where  $(A \cdot B)_{\nu\nu'} = \sum_{\mu} A_{\nu\mu} B_{\mu\nu'}$  is the generic element of the matrix product of matrices  $A$  and  $B$ ,  $X$  and  $BX$  are the sets of exciton and biexciton states,  $N_X$  is the total number of exciton levels and we have neglected the decay from biexciton- to ground-state. Moreover, in Eq. (4.11) we assume that a biexciton has equal probability of decaying into all exciton levels, without

implementing selection rules. Eqs. (4.11) can be formally integrated as

$$\tilde{\rho}_{\nu\nu'}(t)|_{\nu \neq \nu'} = \tilde{\rho}_{\nu,\nu'}^0 e^{-\gamma_2 t} - i e^{-\gamma_2 t} \int_{-\infty}^t dt' \Xi_{\nu\nu'}(t') e^{\gamma_2 t'}, \quad (4.12a)$$

$$\tilde{\rho}_{\nu\nu}(t)|_{\nu \in BX} = \tilde{\rho}_{\nu,\nu}^0 e^{-\gamma_1' t} - i e^{-\gamma_1' t} \int_{-\infty}^t dt' \Xi_{\nu\nu}(t') e^{\gamma_1' t'}, \quad (4.12b)$$

$$\begin{aligned} \tilde{\rho}_{\nu\nu}(t)|_{\nu \in X} = & \tilde{\rho}_{\nu,\nu}^0 e^{-\gamma_1 t} + \frac{\gamma_1'}{N_X} e^{-\gamma_1 t} \sum_{\mu \in BX} \int_{-\infty}^t dt' \tilde{\rho}_{\mu\mu}(t') e^{\gamma_1 t'} \\ & - i e^{-\gamma_1 t} \int_{-\infty}^t dt' \Xi_{\nu\nu}(t') e^{\gamma_1 t'}, \end{aligned} \quad (4.12c)$$

$$\tilde{\rho}_{11}(t) = \tilde{\rho}_{11}^0 + \gamma_1 \sum_{\mu \in X} \int_{-\infty}^t dt' \tilde{\rho}_{\mu\mu}(t') - i \int_{-\infty}^t dt' \Xi_{11}(t'), \quad (4.12d)$$

being  $\tilde{\rho}_{\nu,\nu}^0$  the initial condition and  $\Xi = (\tilde{\rho} \cdot \tilde{\Theta}) - (\tilde{\Theta} \cdot \tilde{\rho})$ . In principle, these equations can be solved for any shape of the excitation field. If the system is assumed to be excited by a sequence of  $\delta$ -pulses the solution is analytical. We derive it in the next section for a two-pulse field that models the excitation field in HSI experiments.

#### 4.2.2 Simulation of HSI experiments - response to a two- $\delta$ -pulses excitation field

In the last section, we have formally solved the dynamical equations for the density matrix that describes a QD system interacting with a generic optical field. If the latter consists of a sequence of  $n$   $\delta$ -pulses exciting the sample at  $t = t_1, \dots, t_n$ , the solution (4.11) of the problem is analytical. At each time  $t_i$  ( $i = 1, \dots, n$ ), Eqs. (4.11) reduce to an algebraic system of equations that give the value  $\tilde{\rho}_{\nu\nu'}(t_i^+)$  of the density matrix after the arrival of the  $i$ -th pulse, assuming the initial condition  $\tilde{\rho}_{\nu,\nu'}^0 = \tilde{\rho}_{\nu\nu'}(t_i^-)$  (here  $t_i^-$  and  $t_i^+$  are the right and left limit of  $t$  to  $t_i$ , respectively). In particular we suppose  $\tilde{\rho}_{\nu\nu'}(t_1^-) = \delta_{\nu\nu'} \delta_{\nu,1}$ , i.e. the sample is in the ground state before the arrival of the first pulse. Each pulse results in a steplike time evolution of each polarization and density, whereas the evolution of the density matrix between two pulses ( $t_i < t < t_j$ ) is free, i.e. governed only by the damping.

In the limit of  $\delta$ -pulses, we assume that the excitation field in HSI two-beam experiments can be written as

$$E(t) = E_{\sigma^1}^1 \delta(t + \tau) \exp(i\Omega_1 t + \phi_1) + E_{\sigma^2}^2 \delta(t) \exp(i\Omega_2 t + \phi_2), \quad (4.13)$$

where the pulse of amplitude  $E^1$  ( $E^2$ ), polarization  $\sigma^1$  ( $\sigma^2$ ), frequency  $\Omega_1$  ( $\Omega_2$ ) and phase  $\phi_1$  ( $\phi_2$ ) excites the quantum system at  $t = -\tau$  ( $t = 0$ ), with

$\tau > 0$ . For fixed delay time  $\tau$  between the two pulses, and fixed phases  $\phi_i$  ( $i = 1, 2$ ), we analytically solve Eqs. (4.11) to get the time evolution of density matrix  $\tilde{\rho}^{\tau\phi}(t)$  ( $\phi = (\phi_1, \phi_2)$ ). After the first pulse, i.e. at  $t = \tau^+$ , the density matrix is the solution of the algebraic set of equations

$$\tilde{\rho}_{\nu\nu'}^{\tau\phi}(-\tau^+) = \delta_{\nu\nu'}\delta_{\nu,1} - i \left[ \tilde{\rho}^{\tau\phi}(-\tau^+) \cdot \tilde{\Theta}(-\tau) - \tilde{\Theta}(-\tau) \cdot \tilde{\rho}^{\tau\phi}(-\tau^+) \right]_{\nu\nu'}, \quad (4.14)$$

and evolves between  $t = -\tau$  and  $t = 0$  according to

$$\tilde{\rho}_{\nu\nu'}^{\tau\phi}(t) \Big|_{\nu \neq \nu'} = \tilde{\rho}_{\nu\nu'}^{\tau\phi}(-\tau^+) e^{-\gamma_2(t+\tau)}, \quad (4.15a)$$

$$\tilde{\rho}_{\nu\nu'}^{\tau\phi}(t) \Big|_{\nu \in BX} = \tilde{\rho}_{\nu,\nu}^{\tau\phi}(-\tau^+) e^{-\gamma'_1(t+\tau)}, \quad (4.15b)$$

$$\tilde{\rho}_{\nu\nu'}^{\tau\phi}(t) \Big|_{\nu \in X} = \tilde{\rho}_{\nu,\nu}^{\tau\phi}(-\tau^+) e^{-\gamma_1(t+\tau)} \quad (4.15c)$$

$$\begin{aligned} & + \frac{\gamma'_1}{N_X(\gamma_1 - \gamma'_1)} \sum_{\mu \in BX} \tilde{\rho}_{\mu,\mu}^{\tau\phi}(-\tau^+) \left[ e^{-\gamma'_1(t+\tau^+)} - e^{-\gamma_1(t+\tau)} \right], \\ \tilde{\rho}_{11}^{\tau\phi}(t) &= \tilde{\rho}_{11}^{\tau\phi}(-\tau^+) + \sum_{\mu \in X} \tilde{\rho}_{\mu,\mu}^{\tau\phi}(-\tau^+) \left[ 1 - e^{-\gamma_1(t+\tau)} \right] \\ & + \frac{\gamma_1 \gamma'_1}{\gamma_1 - \gamma'_1} \sum_{\mu \in BX} \tilde{\rho}_{\mu,\mu}^{\tau\phi}(-\tau^+) \left[ \frac{1 - e^{-\gamma'_1(t+\tau)}}{\gamma'_1} - \frac{1 - e^{-\gamma_1(t+\tau)}}{\gamma_1} \right]. \end{aligned} \quad (4.15d)$$

Evaluating Eqs. (4.15) at  $t = 0$ , gives the initial condition  $\tilde{\rho}_{\nu\nu'}^{\tau\phi}(0^-)$  for the solution of Eqs. (4.11) in correspondence to the arrival of the second pulse

$$\tilde{\rho}_{\nu\nu'}^{\tau\phi}(0^+) = \tilde{\rho}_{\nu\nu'}^{\tau\phi}(0^-) - i \left[ \left( \tilde{\rho}^{\tau\phi}(0^+) \cdot \tilde{\Theta}(0) \right) - \left( \tilde{\Theta}(0) \cdot \tilde{\rho}^{\tau\phi}(0^+) \right) \right]_{\nu\nu'}. \quad (4.16)$$

The free evolution of the density matrix for  $t > 0$  is given by equations that are identical to Eqs. (4.15), but with  $\tau = 0$ . The inversion of Eq. (4.10a) permits to retrieve the full time dependence of the density matrix, as well as the dependence of its non-diagonal elements from the resonances of the quantum system. The sum of these terms is the response of the quantum system to the exciting field

$$P(\tau, \phi, t > 0) = \sum_{\nu, \nu' > \nu} \tilde{\rho}_{\nu\nu'}^{\tau\phi}(0^+) \exp[-i(\omega_\nu - \omega_{\nu'})t - \gamma_2 t], \quad (4.17)$$

We calculate the response function (4.17) in correspondence to different values of  $\tau$  and  $\phi_{1,2}$ . As in HSI experiment, the different orders of the response are selected by Fourier transforming versus  $\phi_{1,2}$ . As explained in Sec. 4.1,

the measured signal is the sum of all  $P^{(\mathbf{n})}$  with  $(l_1, l_2) = (-1, 2)$  that reads

$$\begin{aligned} P^{-1,2}(\tau, t) &= \int d\phi_1 d\phi_2 P(\tau, \phi_1, \phi_2, t) \exp(i\phi_1 - i2\phi_2) \\ &= \sum_{\nu, \nu' > \nu} \tilde{P}_{\nu\nu'}^{-1,2}(0^+, \tau) \exp[-i(\omega_\nu - \omega_{\nu'})t - \gamma_2 t], \end{aligned} \quad (4.18)$$

with  $\tilde{P}_{\nu\nu'}^{-1,2}(\tau, 0^+) = \int d\phi_1 d\phi_2 \tilde{\rho}_{\nu\nu'}^{\tau\phi}(0^+) \exp(i\phi_1 - i2\phi_2)$  and is dominated by the FWM component that is the  $\hat{\chi}^{(3)}$  nonlinearity. Contributions to (4.18) coming from higher order nonlinearities become important in the strong excitation regime, as will be shown in the next section. Considering  $\delta$ -shaped excitation pulses results in a separation of the two time dependencies of the response function, as can be seen in the second line of Eq. (4.18). In particular, the exponential dependence from  $t$  results in simple Lorentz resonances in the frequency domain. The Fourier transform of Eq. (4.18) with respect to  $t$  and  $\tau$  gives the two-dimensional spectra

$$P^{-1,2}(\omega_1, \omega) = \int dt d\tau P^{-1,2}(\tau, t) \exp(-i\omega_1 \tau - i\omega t), \quad (4.19)$$

that is directly comparable with those observed in HSI experiments, as that reported in Fig 4.2. Results relative to many-level QD systems are presented in the next section.

### 4.3 Results

The density matrix formalism developed in the last section allows to determine the coherent response of a multilevel system to an exciting optical field, if the energy levels and the optical coupling matrix are known. The simplest scheme that permits to explain the principal characteristics of 2D-spectra observed in HSI experiments is that of a four levels system. Such a level scheme is a realistic model for several quantum systems. In particular, it is suitable to describe the electronic structure of a single QD whose optically active states, in the spin basis  $|\sigma\rangle$ , are the ground state  $|0\rangle$ , the exciton states  $|\sigma^+\rangle = \hat{c}_\downarrow^\dagger \hat{d}_\downarrow^\dagger |0\rangle$  and  $|\sigma^-\rangle = \hat{c}_\uparrow^\dagger \hat{d}_\uparrow^\dagger |0\rangle$ , and the biexciton state  $|B\rangle = \hat{c}_\downarrow^\dagger \hat{d}_\downarrow^\dagger \hat{c}_\uparrow^\dagger \hat{d}_\uparrow^\dagger |0\rangle$ . Here, the pair states are labeled only with the spin quantum number because their orbital components are all constructed with the same electron and hole state (see Sec. 1.2). The energy levels of states  $|\sigma\rangle$  are

$$\omega_0 = 0, \quad (4.20a)$$

$$\omega_{\sigma^+(\sigma^-)} = \Omega_0 + \frac{1}{2} (V^{ee} + V^{hh} - 2V^{eh}) + V_{\downarrow\downarrow(\uparrow\uparrow)}^{ex}, \quad (4.20b)$$

$$\omega_B = 2(\Omega_0 + V^{ee} + V^{hh} - 2V^{eh}) + V_{\downarrow\downarrow}^{ex} + V_{\uparrow\uparrow}^{ex}. \quad (4.20c)$$

where  $\Omega_0 = \omega^e - \omega^h$  is the energy of the electron-hole pair and we have set  $\hbar = 1$ . In the spin basis  $|\sigma\rangle$ , the optical coupling matrix reads

$$\hat{\Omega} = \begin{pmatrix} 0 & \Omega_{\sigma^+}^* & \Omega_{\sigma^-}^* & 0 \\ \Omega_{\sigma^+} & 0 & 0 & \Omega_{\sigma^-}^* \\ \Omega_{\sigma^-} & 0 & 0 & \Omega_{\sigma^+}^* \\ 0 & \Omega_{\sigma^-} & \Omega_{\sigma^+} & 0 \end{pmatrix}, \quad (4.21)$$

where the Rabi energy of the optical field is  $\Omega_{\sigma^\pm} = \mu_0 E_{\sigma^\pm}$ , and  $\mu_0$  is the dipole matrix element of the transition to both the  $|\sigma^\pm\rangle$  single-pair states. By diagonalizing the QD hamiltonian (4.4) within the subspace of single-pair states, we obtain the eigenbasis  $|\nu\rangle = |0\rangle, |+\rangle, |-\rangle, |B\rangle$ , with

$$\omega_\pm = \frac{\omega_{\sigma^+} + \omega_{\sigma^-}}{2} \pm \sqrt{\left(\frac{\omega_{\sigma^+} - \omega_{\sigma^-}}{2}\right)^2 + |V^{ex}|^2}, \quad (4.22)$$

where  $V^{ex} = V_{\uparrow\uparrow}^{ex} = V_{\uparrow\downarrow}^{ex*}$ . The QD geometry is assumed to be anisotropic, in order to have a non-zero fine structure energy splitting between states  $|+\rangle$  and  $|-\rangle$  (see Sec. 2.3.1). The case of degenerate exciton levels is not interesting because it is not possible to distinguish between diagonal and non-diagonal features in the 2D-spectra. Within the described model of four level system, the dynamical equations for the phonon assisted density matrix have already been solved for an arbitrary sequence of ultrafast pulses [Axt 05]. There, the scope of the work was determine the pulse area and temperature dependences of the carrier-phonon and carrier-field coupling. As in Ref. [Axt 05] we concentrate on a situation where the transition from the electronic ground state  $|0\rangle$  to the exciton eigenstates  $|\pm\rangle$  (0-X transition) couples selectively to orthogonally linear polarized light. This is achieved by setting  $V_{\downarrow\downarrow}^{ex} = V_{\uparrow\uparrow}^{ex}$  and  $V^{ex} = |V^{ex}|$  whereby the transformation matrix  $S$  between basis  $|\sigma\rangle$  and  $|\nu\rangle$  reads

$$\hat{S} = \begin{pmatrix} 1 & 0 & 0 & 0 \\ 0 & 1/\sqrt{2} & 1/\sqrt{2} & 0 \\ 0 & 1/\sqrt{2} & -1/\sqrt{2} & 0 \\ 0 & 0 & 0 & 1 \end{pmatrix}. \quad (4.23)$$

The energy scheme of the four level system  $|\nu\rangle$  is illustrated in Fig. 4.3.(a). A qualitative description of the biexciton in terms of Coulomb correlation has already been given in Sec. 1.2. A simplified picture of the biexciton is that of a bound state of two Coulomb interacting excitons. In Fig. 4.3.(a) the biexciton state  $|B\rangle$ , composed of states  $|+\rangle$  and  $|-\rangle$ , is assumed to have a positive binding energy  $E_B = \omega_+ + \omega_- - \omega_B$ . The optical excitation of the system to the biexciton state is a two-photon process, as long as the

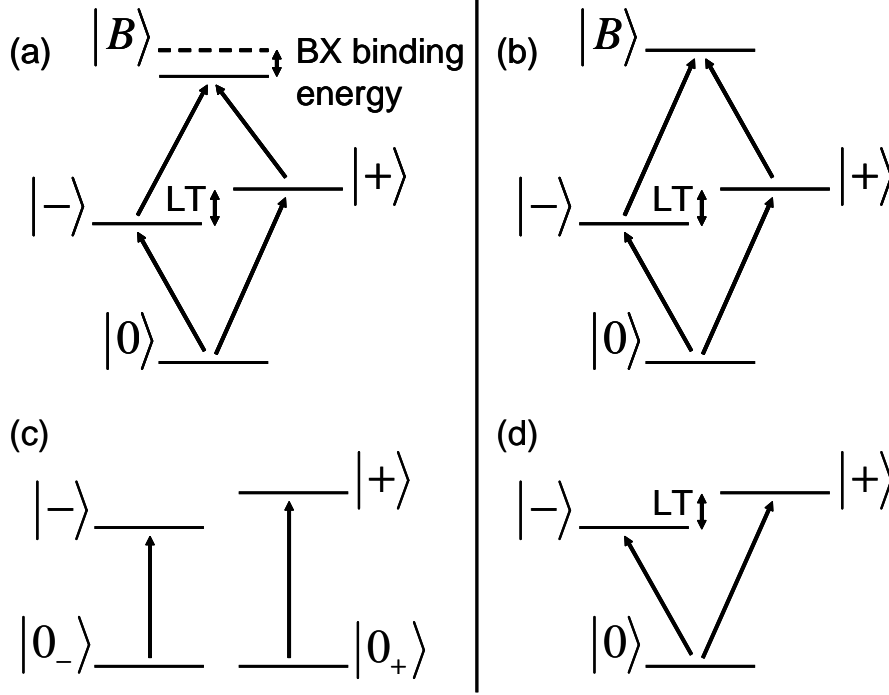


Figure 4.3: (a) Four-level scheme for the QD system under study. The biexciton  $|B\rangle$  can be depicted as a bound state of excitons  $|+\rangle$  and  $|-\rangle$ , with positive binding energy  $E_B = \hbar(\omega_+ + \omega_- - \omega_B)$ . (b) In the limit  $E_B = 0$ , the same level scheme of (a) is equivalent to scheme (c), describing two uncoupled two-level systems, as long as optical transitions with the same energy have the same dipole matrix element. (d) A three-level system in a V-scheme describes two coupled two-level systems.

initial state is the ground state. Then, in the low intensity regime, the linear response of the system to an ultrafast pulse doesn't contain biexciton signatures. Once the system has been excited to the state  $|\pm\rangle$ , a second pulse can induce the corresponding exciton-biexciton (X-BX) transition (i.e. the one with energy  $\omega_B - \omega_{\pm}$ ). This process should be observable in the third order response, resulting in a peak at the frequency  $\omega_B - \omega_{\pm}$  in the FWM spectrum.

The calculation of the response of the four level system in Fig. 4.3.(a) (i.e. with  $E_B > 0$ ), to the two-pulse excitation field of Eq. (4.13), results in the spectrum  $|P^{-1,2}(\omega_1, \omega)|^2$  of Fig. 4.4.(a). The phase of  $P^{-1,2}(\omega_1, \omega)$  is given in Fig. 4.5.(a), where the blue and red correspond to negative and positive values respectively, and horizontal and vertical lines correspond to steps of the phase. In our calculation both pulses have polarization  $\sigma^+$  and Rabi energy  $\Omega_{\sigma^+} = 5 \mu\text{eV}$ , that corresponds to a low intensity of the exciting

fields. The frequency of the first pulse is  $\Omega_1 = (\omega_+ + \omega_-)/2$  while the value of  $\Omega_2$  is unimportant, being the second  $\delta$ -pulse centered at  $t = 0$  [see Eq. (4.13)]. The linear and the FWM response can be read on the horizontal ( $\omega_1$ ) and on the vertical ( $\omega$ ) axis of Fig. 4.4.(a), respectively. Diagonal peaks at the exciton energies  $(\omega_1, \omega) = (\omega_{\pm}, \omega_{\pm})$  correspond to the linear response of the two independent two level systems  $|0\rangle, |+\rangle$  and  $|0\rangle, |-\rangle$ . The off-diagonal peaks at  $(\omega_1, \omega) = (\omega_{\pm}, \omega_{\mp})$  correspond to a third order excitation path. At  $t = -\tau$  the first pulse excites the system and create a polarization grating over 0-X transitions with energy  $\omega_{\pm}$ . If  $\tau$  is smaller than the relaxation time of the system, at  $t = 0$  the grating is still present and the second pulse interacts with it, then exciting the second 0-X transition with energy  $\omega_{\mp}$ . Then, these peaks are the spectral signature of the coherent coupling between the two 0-X transitions. In a similar way one can explain the peaks at  $(\omega_1, \omega) = (\omega_{\pm}, \omega_B - \omega_{\pm})$ . The second pulse interacts with the polarization grating produced by the first pulse over the 0-X transition with energy  $\omega_{\pm}$ , then exciting the X-BX transition with energy  $\omega_B - \omega_{\pm}$ . Then, these peaks are the signature of the coherent coupling between the 0-X and the corresponding X-BX transition. Note that all the peaks in Figs. 4.4.(a) have the same intensity, because all the optical transitions of the system under study have the same dipole matrix element. When we reduce the value of  $E_B$ , the peaks corresponding to the X-BX transitions approach the off-diagonal peaks describing the X-X coupling, until they superpose for  $E_B = 0$ . In this limit, the level scheme of Fig. 4.3.(a) becomes that of Fig. 4.3.(b) and the corresponding spectrum 4.4.(a) becomes spectrum 4.4.(b), in which only the diagonal peaks at  $(\omega_1, \omega) = (\omega_{\pm}, \omega_{\pm})$  are present. This behavior is explained by comparing the corresponding phases in Figs. 4.5.(a) and (b): the X-BX transition contributions to spectrum 4.4.(a) are exactly opposite in phase to the off-diagonal X-X contributions, thus canceling each other for  $E_B = 0$ , as Figs. 4.5.(b) shows. This result is in perfect agreement with the level scheme of Fig 4.3.(b) where the X-BX and the 0-X transitions have the same energies (i.e.  $\omega_B - \omega_{\pm} = \omega_{\mp}$ ), and the transition between states  $|\pm\rangle$  and  $|B\rangle$  is not distinguishable from that between states  $|0\rangle$  and  $|\mp\rangle$ . Fig 4.3.(b) is then a suitable representation of two independent two level systems, for which only diagonal peaks are expected, and is equivalent to the energy levels scheme in Fig 4.3.(c). In Fig. 4.4.(c) a spectrum is calculated as for Fig. 4.4.(a), but setting to zero the matrix elements of the optical coupling matrix  $\hat{\Theta} = \hat{S}\hat{\Omega}\hat{S}^{-1}$  corresponding to the X-BX transitions. The system reduces to three levels system in the V-scheme of Fig. 4.3.(d) that correspond to two coupled two-levels system for which the off-diagonal exciton peaks are observed, because the X-BX transitions with opposite phase no longer contribute to the third order spectrum. This picture is supported by the comparison of the corresponding phase structures

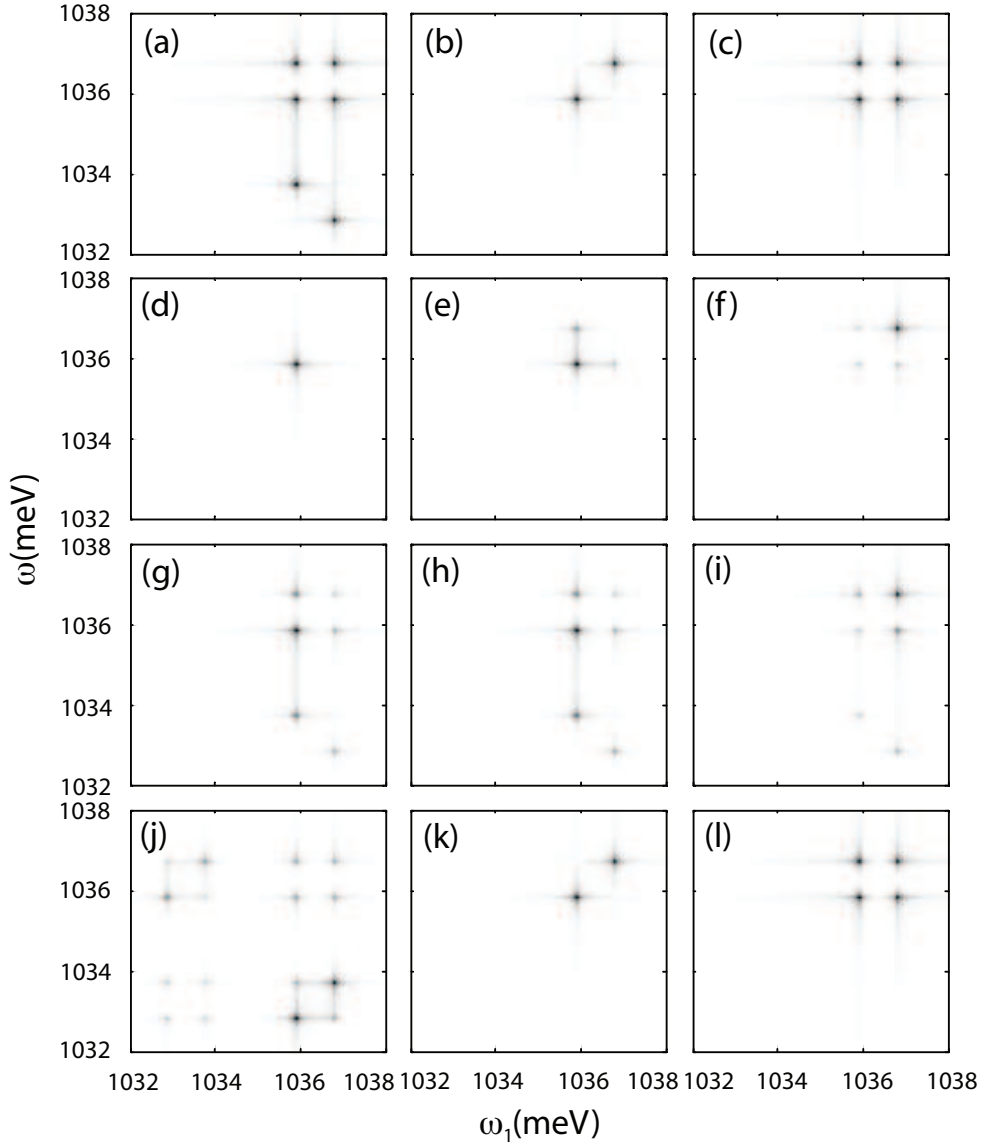


Figure 4.4: Spectra  $|P^{-1,2}(\omega_1, \omega)|^2$  calculated for the four-level systems in Fig. 4.3 in different cases, for excitation by two- $\delta$ -pulses field of Eq. (4.13), with  $\sigma^1 = \sigma^2 = \sigma^+$ ,  $\Omega_1 = (\omega_+ + \omega_-)/2$ . Linear color scale. In (a) to (i) we study the third order response in the low intensity regime, by fixing  $\Omega_{\sigma^1} = \Omega_{\sigma^2} = 5 \mu\text{eV}$ . (a), (b), (c) are calculated for the level scheme in Fig. 4.3.(a), (b), (d) respectively by assuming the same value  $\mu_0$  for the dipole moment of all the allowed optical transitions. (d), (e), (f) and (g), (h), (i) are calculated for scheme 4.3.(b) and (a) respectively, by changing the ratio between the dipole moments of different transitions (see text). (j), (k), (l) correspond to (a), (b), (c) respectively, but are calculated in the high intensity regime, with  $\Omega_{\sigma^1} = \Omega_{\sigma^2} = 1 \text{ meV}$ , in order to check spectral contributions beyond the third order non-linearity.

in Fig. 4.5.(a) and (c).

Coming back to the level scheme of Fig 4.3.(b), the two resonances can be coupled if the dipole matrix elements of the transitions are assumed to be different. Spectrum 4.4.(d) is obtained assuming a ratio 0.6 between the dipole matrix element of the transitions with energy  $\omega_+$  and that of the transitions with energy  $\omega_-$ . The straightforward result, is that the diagonal peaks have different intensity. Here, as the same dipole matrix element have been assigned to transitions with the same energy, the two two-level systems are still uncoupled and off-diagonal signals are not observed. Assuming a dipole matrix element  $\mu_0$  for the 0-X transition with energy  $\omega_+$  and for the X-BX transition with energy  $\omega_-$  and  $0.6\mu_0$  for the other two transitions, results in two coupled two-level systems, and in the appearance of two off-diagonal signals in spectrum 4.4.(e). Spectrum 4.4.(f) is obtained by assuming four different values for dipole matrix elements of the four optical transitions. Spectra 4.4.(g), (h), (i) are calculated for  $E_B > 0$ , and for the same values of the dipole matrix elements of spectra 4.4.(d), (e), (f) respectively. The comparison between spectra 4.4.(g) and (d) is qualitatively the same of that between spectra 4.4.(a) and (b). When  $E_B$  reduces to zero, the X-BX coupling signals superpose to the X-X ones and cancel them, again recovering the picture of two uncoupled two-level systems. The cancelation of the signals is only partial in the transition from spectra 4.4.(h) and (i) to spectra 4.4.(e) and (f) respectively, as, in both cases, the two resonances of the final system are coupled.

Spectra 4.4.(a) to (i) give an accurate description of the way in which the coupling between the resonances of a generic four level system manifests itself in the coherent third-order response to excitation by optical field in a two-pulses experiment. We complete our analysis studying the higher order contributions. Three more spectra are shown in Fig. 4.4, that have been calculated for excitation pulses with Rabi frequency  $\Omega_{\sigma+} = 1$  meV, while all the other parameters remain unchanged with respect to the previous cases and, in particular, all the transitions are assumed to have the same dipole matrix element  $\mu_0$ . Spectra 4.4.(j), (k), (l) should be compared to spectra 4.4.(a), (b), (c), respectively (i.e. correspond to  $E_B > 0$ ,  $E_B = 0$  and to turn off the optical X-BX transitions). Spectrum 4.4.(j) contains spectrum 4.4.(a) as low intensity limit, but in this case, FWM signal are visible also on the  $\omega_1$ -axis. In fact, the peaks at  $(\omega_1, \omega) = (\omega_B - \omega_{\pm}, \omega_{\pm})$  correspond to optical transition to the biexciton state stimulated by the first pulse via two-photon absorption processes that take place in the high intensity regime. All the other signals present in the spectrum are due to excitation processes at the fifth and successive orders. We have verified that any further increase of the excitation field only result in changing the intensities of the peaks, while the

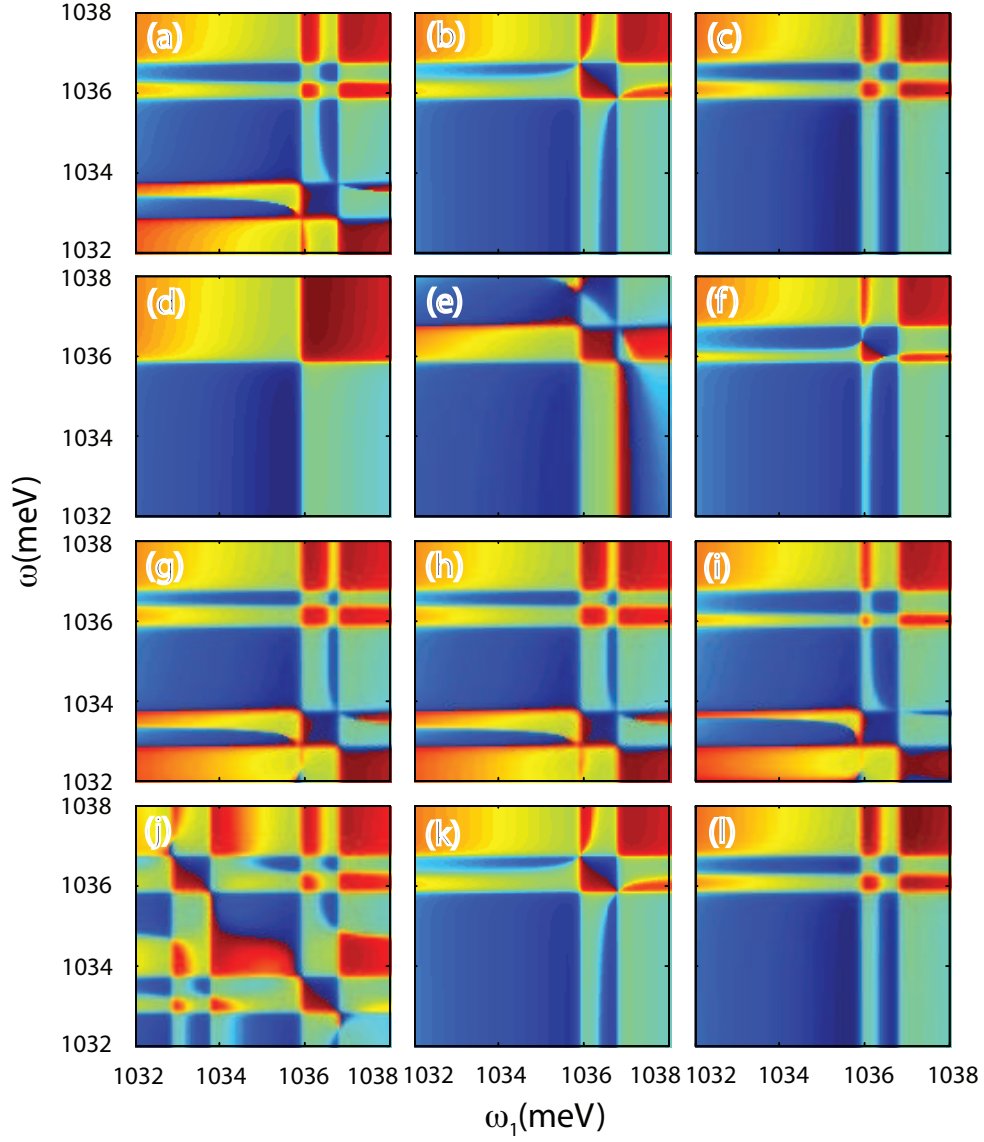


Figure 4.5: Phase of the third order response  $P^{-1,2}(\omega_1, \omega)$  corresponding to spectra in Fig. 4.4. Linear color scale.

occurrence of signal in new positions on the  $(\omega_1, \omega)$ -plane is not observed. The corresponding phase in Fig. 4.5.(j) has a complex structure that is characterized by several steps in correspondence of the four resonances of the system, on both the  $\omega_1$  and  $\omega$  axes. Nevertheless, for  $E_B = 0$  all the phases compensate as already in the low intensity regime, resulting in the phase structure in Fig. 4.5.(k) that is identical to that of Fig. 4.5.(b), and in the intensity spectrum 4.4.(k) that is qualitatively identical to 4.4.(b), the only difference being the peak intensities. An analogous analysis holds for spectrum 4.4.(l) that differs from spectrum 4.4.(c) only for the intensities of the peaks and whose phase structure 4.5.(l) is identical to 4.5.(c). The structure of the phase of third order coherent response can be very rich, depending on the multilevel system considered and on the excitation regime, and of difficult interpretation. Nevertheless, HSI technique allows for the first time the direct detection of the phase of the FWM signal, so that diagrams like those in Fig. 4.4 could be directly compared with experimentally measured phases.

We continue our analysis of the coherent response of a multilevel system to a two-pulse excitation field in the HSI experimental configuration showing results for a two-QD system. Here, we address the same QD system described in Sec. 3.1.1 consisting of two vertically stacked cylindrical QDs. The exciton and biexciton energies are plotted versus interdot distance in Fig. 4.6.(a) and (b), respectively. The exciton level structure is the same of that in Fig. 3.3.(a). The material and geometrical parameters are those used in Sec. 3.1.1, but in the present case repulsive and exchange contributions to Coulomb interaction are taken into account as well as the electron-hole attraction, resulting in a small quantitative correction to Fig. 3.3.(a). Moreover, considering spin variables results in eight exciton states, whose energy are grouped in four pairs of quasi-degenerate levels split by the exchange interaction, as the insets in Fig. 4.6.(a) show. As the splitting is of the order of 0.2 meV, while the energy scale of the system is of the order of tens of meV, the fine structure spectra are not distinguishable in the simulated spectra that we are going to show. Then, in the following analysis of the spectra we will just refer to the exciton levels as if they were just four.

The spectrum in Fig. 4.7.(a) have been calculated for the two QDs at distance  $R = 6$  nm, in the same excitation conditions of spectrum 4.4.(a). As usual, in the low excitation regime the linear and the third-order response can be read on the  $\omega_1$  and  $\omega$  axis, respectively. As for a four-level system, the spectrum contains diagonal peaks corresponding to the linear response of the independent exciton transitions, and off-diagonal peaks corresponding to the third order response of the coupled exciton resonances. If we set equal to zero all the elements of the optical coupling matrix corresponding to

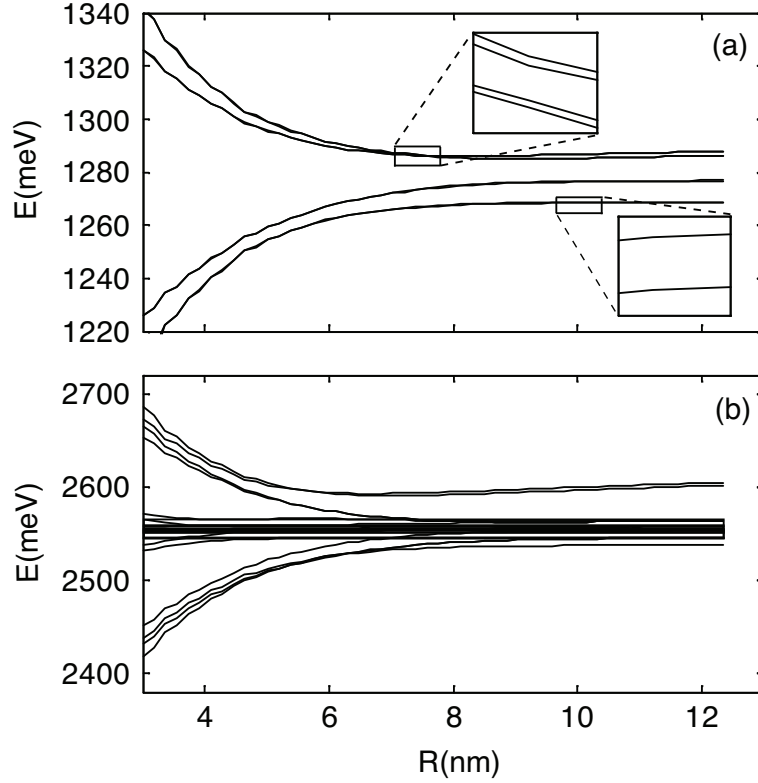


Figure 4.6: Exciton (a) and biexciton (b) energies for InAs QD molecule, as for Fig. 3.3.(a). The insets are magnifications that show the fine structure splitting of quasi-degenerate exciton levels. The weak wiggling behavior of the curves is an artifact of the numerical calculation.

the X-BX transitions, these are the only possible signals. In this condition we have calculated spectrum 4.7.(b) that correspond to a generalization of the V-level-scheme of Fig. 4.3.(d), in which coupled 0-X transition to four different excited states are possible. In this spectrum, then, 16 signals of the same intensity would be observed if all the dipole moments were equal. Nevertheless, according to Fig. 3.3.(b), for  $R = 6$  nm the highest and lowest exciton levels are more optically active than the other two, and the corresponding diagonal peaks are better visible. However, off diagonal signals rising from the third-order coupling between each pair of 0-X transitions are well visible. All the other signals present in spectrum 4.7.(a) are the signature of the third order coupling between 0-X and X-BX transitions as for the four-level system. However, in the present case many signals are observed, corresponding to both bound and unbound coupled biexcitons. When the

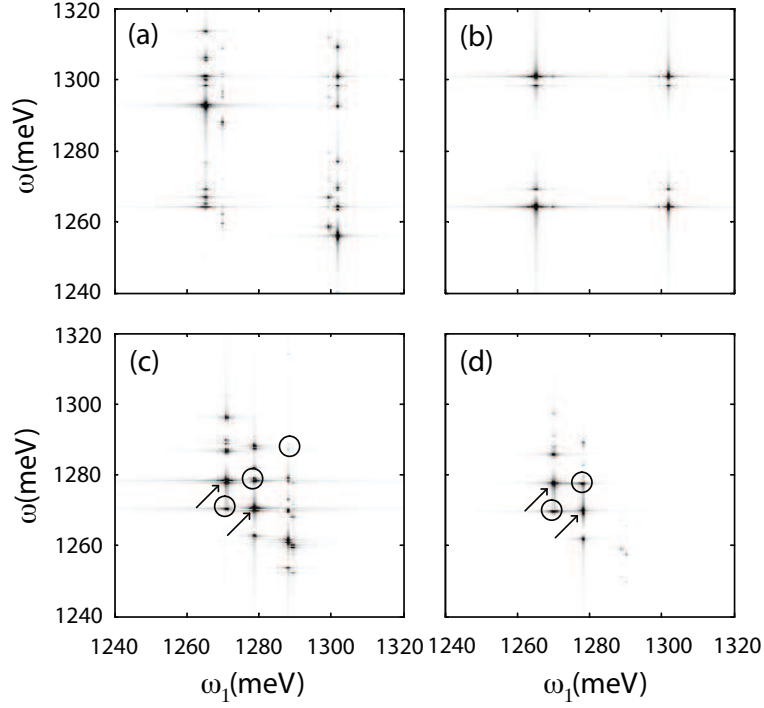


Figure 4.7: Spectra  $|P^{-1,2}(\omega_1, \omega)|^2$  calculated with the same excitation field of Figs. 4.4.(a) to (i) for a two-QD system, varying the interdot distance  $R$ . (a)  $R = 6$  nm. (b)  $R = 6$  nm as in (a), but the elements of the optical coupling matrix corresponding to the X-BX transitions are set equal to zero. (c)  $R = 11$  nm. (d) For  $R = 15$  nm the two higher energy excitons are dark and the corresponding diagonal peaks are not observed. In order to emphasize the features of the spectra, the linear color scale has been set from zero to the 10% of the maximum value of  $|P^{-1,2}(\omega_1, \omega)|^2$ , in each spectra.

interdot distance is increased, the direct excitons (i.e. localized on one of the QDs, see discussion in Sec. 3.1.1) with low energy are optically active, while the indirect excitons become dark. Spectra 4.7.(c) and (d) are calculated for  $R = 11$  nm and  $R = 15$  nm, respectively. The diagonal peaks corresponding to the linear 0-X transitions are circled. As expected, the two low-energy peaks are very intense. Nevertheless, for  $R = 11$  nm the indirect excitons are not yet completely dark and the corresponding peaks are still visible. For  $R = 15$  nm instead, the high energy peaks completely disappear. Nevertheless, their signature is still present in the third order response. These two spectra show that the Förster coupling between the direct exciton states is very efficient, resulting in intense off-diagonal peaks (arrows). Many signals

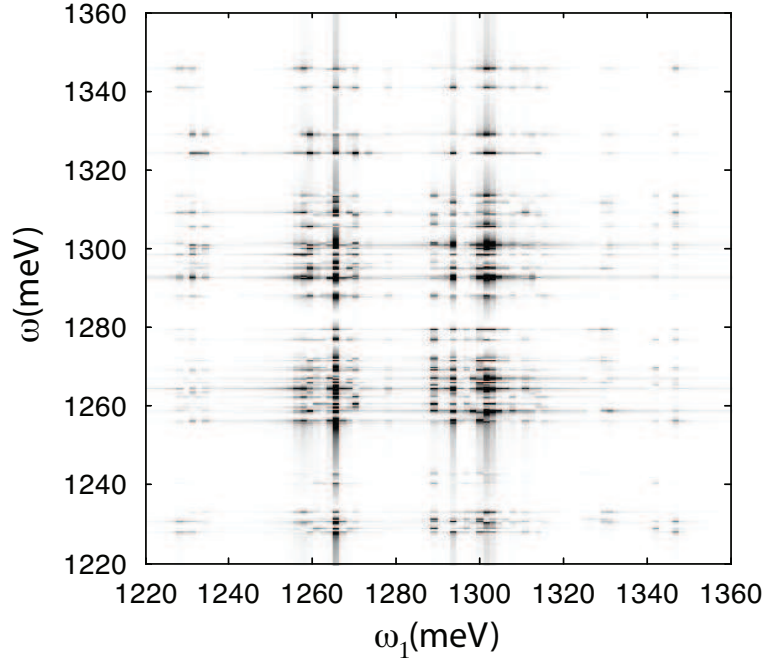


Figure 4.8: Spectrum  $|P^{-1,2}(\omega_1, \omega)|^2$  of the two QD system, calculated as in Figs. 4.7, with  $\Omega_{\sigma+} = 1$  meV and  $R = 6$  nm. In order to emphasize the features of the spectrum, the linear color scale has been set from zero to the 10% of the maximum value of  $|P^{-1,2}(\omega_1, \omega)|^2$ .

corresponding to the coupling between 0-X and X-BX transitions are present in both spectra.

To conclude our analysis, we have calculated the response of a QD molecule, with  $R = 6$  nm, to an intense field, with  $\Omega_{\sigma+} = 1$  meV. The resulting spectrum in Fig. 4.8 shows the effect of the higher order non-linearities. The increased number of energy levels with respect to the case of the simple four-level system results in a very complex spectral pattern, where signals appear in spectral positions that are linear combinations of the transition frequencies of the multilevel system. Obviously, in this regime the HSI method is no more effective for a precise characterization of the coherent coupling mechanism.

## 4.4 Conclusions

We have theoretically modeled for the first time the HSI experimental technique, developing a very general density matrix approach allowing to describe the coherent coupling between the resonances of a multilevel system. Any

---

set of coupled quantum systems can be described in our formalism, as long as the energy levels of the local quantum states, their oscillator strengths and the coupling matrix between the different systems, are known. We have simulated a HSI experiment on two systems of Coulomb correlated exciton and biexciton states, showing that the coherent coupling between two states results in off-diagonal peaks of the two-dimensional FWM spectrum, thus confirming the interpretation of Langbein *et al.* of the observed HSI spectra. We have also shown that, in the low intensity regime, each spectral signal can be associate *univocally* to a specific nonlinear third order excitation path, even if this become a difficult task if the number of levels involved is big. However, in the high intensity regime, nonlinearities of the fifth or higher order give important contributions to the spectra, that become very rich and of difficult precise interpretation. In summary, we give a solid theoretical support to a powerful experimental technique enabling to identify the coherent coupling between strongly confined quantum systems.



# Conclusions

The theoretical investigation of several interaction mechanisms between semiconductor quantum dots presented in this thesis shows that, despite its atomic-like spectrum characterized by widely spaced energy levels, a quantum dot is a complex system strongly coupled to its environment. We have shown that quantum dots forming an ensemble are coupled with each other via tunneling of the electron wave function, Coulomb interaction, mechanisms of excitation transfer over short (Förster) and long (radiative) distances, phonon-mediated coupling. All these coupling mechanisms are responsible of the decoherence of the quantum state, that is the major obstacle for a solid-state implementation of quantum information processing.

The mutual interaction between quantum dots is verified at different levels of approximation in the description of the quantum dot system. The simplest description of a quantum dot is that of a macroatom [Zana 98, Biol 00], i.e. a two-level system that does not interact with the surrounding semiconductor matrix. We have shown that, even in this oversimplified picture, quantum dots in an ensemble interact via radiative coupling. In Chapter 2, we have shown that the radiative coupling in a quantum dot ensemble is responsible of the emergence of collective modes that are *sub-radiant* and *super-radiant* with respect to the excited state of an isolated dot. The effect of the coupling on the radiative decay-rate is expected to be of the order of  $1 \mu\text{eV}$ . Despite its small magnitude, radiative coupling decays as the inverse of the interdot distance effectively coupling dots over a distance of a few hundreds of nanometers. We have shown that the radiative coupling is a long-range correction to the electrostatic Förster mechanism, due to the retardation in the electromagnetic field propagation [Para 05, Para 07]. In [Para 05] we suggest that in a dense QD sample this effect should be observable as a non-exponential decay of the photoluminescence (PL) signal. Recently [Sche 07] Scheibner *et al.* have observed the increase of the PL emission rate in QD mesas when passing from strictly non-resonant to quasi-resonant excitation, suggesting radiative coupling between the quantum dots. Furthermore, by reducing the QD density they verify that the range of the interaction in

CdSe/ZnSe QDs is at least 150 nm providing a striking confirmation of our theoretical prediction.

Beyond the picture of a macroatom, we have described quantum dot arrays as multilevel systems, taking into account the effects of the tunneling and of the Coulomb interaction. In Chapter 3, we have modeled the optical response of excitons in such a quantum dot system, further including the coupling to the vibrational modes of the crystal via an exciton-acoustic-phonon coupling Hamiltonian. In the second order Born approximation, we have shown that the off-diagonal phonon-assisted coupling in quantum dot arrays produces a spectral broadening of the zero-phonon lines significantly larger than the radiative linewidth, that could explain the broad linewidths experimentally measured [Borr 03] in QD molecules. Moreover, we have shown that the phonon scattering to dark states is enhanced when the phonon wavelength matches the interdot distance. This matching condition results in an oscillatory behavior of the exciton dephasing rates in terms of which we have explained the strong distance dependence of the ZPL widths measured in QD molecules by Borri *et al.* [Borr 03]. We have shown that the polarization dephasing is suppressed in correspondence of the minima of the oscillations but, as the oscillations are very broad, the suppression is realized for well defined values of  $R$  that, furthermore, depend strongly on structural properties of the single quantum in the array. Then, this mechanism of decoherence suppression is not sufficiently effective to be exploited in the realization of quantum gates based on arrays of quantum dots as proposed in [Zana 98, Bert 04] on the basis of the oversimplified picture of the macroatom.

The coherent coupling between the resonances of a multilevel system due to many-body interactions can be determined, in extended semiconductors, by two-dimensional Fourier transform spectroscopy [Borc 05, Li 06]. A novel implementation of this technique, the heterodyne spectral interferometry (HSI) [Lang 06, Lang 07], allowing the study of samples of subwavelength size, as is the case for most individual quantum systems, have been theoretically modeled for the first time in Chapter 4 of this thesis. We have shown that the coherent coupling between two states of a multilevel system of Coulomb correlated exciton and biexciton states, results in off-diagonal peaks of the two-dimensional spectrum, thus confirming the interpretation of Langbein *et al.* [Lang 06, Lang 07] of the observed HSI spectra. We have also shown that, in the low intensity regime, the HSI allows to associate *univocally* each spectral signal to a specific nonlinear third order excitation path, even if this become a difficult task if the number of levels involved is big, giving a solid theoretical support to a powerful experimental technique enabling to identify the coherent coupling between strongly confined quantum systems.

Research in semiconductor quantum dots has rapidly progressed from studying the fundamental properties of electronic states to a collective effort towards optoelectronic applications. The current research puts special emphasis on the realization of single- and few-dot devices, for single photon emission and quantum information processing. The present work suggests that a few-dot system can display a behavior much more complex than what was intuitively expected. Excitation transfer without tunneling, especially when mediated by radiative processes, is expected to be at the same time an obstacle and an possible advantage for technological applications. Quantum-dot molecules and quantum dots embedded in strongly resonant photonic structures (micropillars, nanocavities based on photonic crystal slabs) in particular, are rapidly emerging as the main targets of future research. The present analysis should therefore serve as starting point and a stimulus for future investigations.



# Appendix A

## Microscopic derivation of Coulomb interaction in crystals

The second quantization Coulomb Hamiltonian is

$$\hat{H}_c = \frac{1}{2} \int d\mathbf{r} d\mathbf{r}' \sum_{ss'} \hat{\psi}_s^\dagger(\mathbf{r}) \hat{\psi}_{s'}^\dagger(\mathbf{r}') \frac{e^2}{\epsilon_\infty |\mathbf{r} - \mathbf{r}'|} \hat{\psi}_{s'}(\mathbf{r}') \hat{\psi}_s(\mathbf{r}), \quad (\text{A.1})$$

where  $\hat{\psi}_s(\mathbf{r})$  and  $\hat{\psi}_s^\dagger(\mathbf{r})$  are the second quantization electron field operator, and  $\epsilon_\infty$  is the static dielectric constant.  $\hat{\psi}_s(\mathbf{r})$  can be expanded into Wannier functions of the conduction and valence bands as

$$\hat{\psi}_s(\mathbf{r}) = \sum_{\mathbf{R}cv} \left[ \hat{c}_{\mathbf{R}c} w_c(\mathbf{r} - \mathbf{R}, s) + \hat{d}_{\mathbf{R}v}^\dagger w_v(\mathbf{r} - \mathbf{R}, s) \right], \quad (\text{A.2})$$

where  $\hat{c}_{\mathbf{R}c}^\dagger$  ( $\hat{d}_{\mathbf{R}v}^\dagger$ ) is the electron (hole) creation operator at the lattice vector  $\mathbf{R}$ , specific to one of the conduction (valence) bands under consideration. From now on, we assume the two-band approximation. Even in this case, we need to take spin degeneracy as a band label. The Wannier functions  $w_a(\mathbf{r}, s)$  ( $a \in c, v$ ) are assumed to be well localized within the elementary cell. Then  $\hat{H}_c$  takes the form

$$\hat{H}_c = \frac{1}{2} \sum_{aa'bb'} \sum_{\mathbf{R}\mathbf{R}'} \hat{e}_{a\mathbf{R}}^\dagger \hat{e}_{a'\mathbf{R}'}^\dagger W^{aa'b'b}(\mathbf{R} - \mathbf{R}') \hat{e}_{b'\mathbf{R}'} \hat{e}_{b\mathbf{R}}, \quad (\text{A.3})$$

with the shorthand notation  $\hat{e}_{a\mathbf{R}} = \hat{c}_{\mathbf{R}c}$  if  $a = c$ , and  $\hat{e}_{a\mathbf{R}} = \hat{d}_{\mathbf{R}v}^\dagger$  if  $a = v$ . The coulomb matrix elements

$$W^{aa'b'b}(\mathbf{R}) = \frac{e^2}{\epsilon_\infty} \int d\mathbf{r} d\mathbf{r}' \sum_{ss'} \frac{w_a^*(\mathbf{r}, s) w_{a'}^*(\mathbf{r}', s') w_{b'}(\mathbf{r}', s') w_b(\mathbf{r}, s)}{|\mathbf{r} - \mathbf{r}' + \mathbf{R}|}, \quad (\text{A.4})$$

have the symmetry

$$W^{aa'b'b}(\mathbf{R}) = W^{a'abb'}(-\mathbf{R}) . \quad (\text{A.5})$$

We concentrate on nonlinear optical response up to the third order. Therefore we treat the Hilbert space of single electron-hole pair (or exciton) and two-pair (or biexciton) states. The former can be written as

$$|\nu\rangle = \sum_{\mathbf{R}\mathbf{R}'} \Psi_{\nu}(\mathbf{R}, \mathbf{R}') \hat{c}_{\mathbf{R}}^{\dagger} \hat{d}_{\mathbf{R}'}^{\dagger} |0\rangle , \quad (\text{A.6})$$

where  $|0\rangle$  is the vacuum state and  $\Psi_{\nu}(\mathbf{R}, \mathbf{R}')$  is exciton envelope wave function normalized according to

$$\sum_{\mathbf{R}\mathbf{R}'} \Psi_{\nu}^*(\mathbf{R}, \mathbf{R}') \Psi_{\mu}(\mathbf{R}, \mathbf{R}') = \delta_{\nu\mu} . \quad (\text{A.7})$$

The biexciton states are the factored product of two exciton states. Using the symmetry Eq. (A.5) we get

$$\begin{aligned} \hat{H}_c = & \frac{1}{2} \sum_{\mathbf{R}\mathbf{R}'} \left[ \hat{c}_{\mathbf{R}}^{\dagger} \hat{c}_{\mathbf{R}'}^{\dagger} W_C^{ee}(\mathbf{R} - \mathbf{R}') \hat{c}_{\mathbf{R}'} \hat{c}_{\mathbf{R}} + \hat{d}_{\mathbf{R}}^{\dagger} \hat{d}_{\mathbf{R}'}^{\dagger} W_C^{hh}(\mathbf{R} - \mathbf{R}') \hat{d}_{\mathbf{R}'} \hat{d}_{\mathbf{R}} \right. \\ & \left. - 2 \hat{c}_{\mathbf{R}}^{\dagger} \hat{d}_{\mathbf{R}'}^{\dagger} W_C^{eh}(\mathbf{R} - \mathbf{R}') \hat{d}_{\mathbf{R}'} \hat{c}_{\mathbf{R}} + 2 \hat{c}_{\mathbf{R}}^{\dagger} \hat{d}_{\mathbf{R}}^{\dagger} W_F(\mathbf{R} - \mathbf{R}') \hat{d}_{\mathbf{R}'} \hat{c}_{\mathbf{R}'} \right] , \quad (\text{A.8}) \end{aligned}$$

with

$$W_C^{ee}(\mathbf{R}) = W^{cccc}(\mathbf{R}) , \quad (\text{A.9a})$$

$$W_C^{hh}(\mathbf{R}) = W^{vvvv}(\mathbf{R}) , \quad (\text{A.9b})$$

$$W_C^{eh}(\mathbf{R}) = W^{cvvc}(\mathbf{R}) , \quad (\text{A.9c})$$

$$W_F(\mathbf{R}) = W^{cvcv}(\mathbf{R}) . \quad (\text{A.9d})$$

The four terms in Eq. (A.8) describe the repulsion between electrons and between holes, the electron-hole attraction, and the exchange (Förster) interaction, respectively<sup>1</sup>. To calculate the potentials in Eq. (A.9), we apply the multipole expansion

$$\frac{1}{|\mathbf{r} - \mathbf{r}' + \mathbf{R}|} = \frac{1}{R} - \frac{(\mathbf{r} - \mathbf{r}') \cdot \mathbf{R}}{R^3} + \frac{3[(\mathbf{r} - \mathbf{r}') \cdot \mathbf{R}]^2 - (\mathbf{r} - \mathbf{r}')^2 R^2}{2R^5} - \dots \quad (\text{A.10})$$

---

<sup>1</sup>We have introduced the carrier indexes  $e, h$  in order to be consistent with the notation adopted in the rest of the thesis. As we are using the electron-hole picture and assuming the two-band approximation, there is a one-to-one correspondence between the two sets of band  $(c, v)$  and carrier  $(e, h)$  indexes. When necessary, we will refer to corresponding indexes with the same label (e.g.,  $a = e$  and  $a = c$  on the two sides of the same equation) without ambiguity.

In the Coulomb potential, the leading term  $1/R$  gives the standard expression

$$W_C^0(\mathbf{R}) = \frac{e^2}{\epsilon_\infty R} \quad (\text{A.11})$$

As  $|w_a(\mathbf{r}, s)|^2$  are even function under inversion  $\mathbf{r} \rightarrow -\mathbf{r}$ , only terms with squared arguments in Eq. (A.10) give nonzero contributions, leading to a correction of order  $1/R^3$

$$\begin{aligned} \Delta W_C^{aa'}(\mathbf{R}) = & \frac{e^2}{2\epsilon_\infty R^5} \left[ (R^2 - 3X^2) \overline{x_{aa'}^2} \right. \\ & \left. + (R^2 - 3Y^2) \overline{y_{aa'}^2} + (R^2 - 3Z^2) \overline{z_{aa'}^2} \right], \end{aligned} \quad (\text{A.12})$$

with

$$\overline{x_{aa'}^2} = \int d\mathbf{r} x^2 \sum_\sigma (|w_a(\mathbf{r}, s)|^2 + |w_{a'}(\mathbf{r}, s)|^2) \quad \text{etc.} \quad (\text{A.13})$$

In the Förster potential, due to orthogonality

$$\int d\mathbf{r} \sum_s w_c^*(\mathbf{r}, s) w_v(\mathbf{r}, s) = 0, \quad (\text{A.14})$$

there is no term of order  $1/R$ , and only mixed terms in the third term of Eq. (A.10) survive, giving

$$W_F(\mathbf{R}) = \frac{R^2 |\mu_{cv}|^2 - 3 |\mathbf{R} \cdot \boldsymbol{\mu}_{cv}|^2}{\epsilon_\infty R^5}, \quad (\text{A.15})$$

being the dipole vector defined as

$$\boldsymbol{\mu}_{cv} = e \int d\mathbf{r} w_c^*(\mathbf{r}) \mathbf{r} w_v(\mathbf{r}). \quad (\text{A.16})$$

In the strong confinement regime, the heavy and light hole states of materials with zincblende structure are completely separate. We concentrate on heavy hole (hh) states, which form the lowest confinement level. The Wannier functions factorize into spin and spatial part as

$$w_{c\sigma}(\mathbf{r}) = \langle \mathbf{r} | S \rangle \delta_{s,\sigma} \quad (\text{A.17a})$$

$$w_{hh\sigma}(\mathbf{r}) = \frac{1}{\sqrt{2}} \langle \mathbf{r} | x + i\sigma y \rangle \delta_{s,\sigma} \quad (\text{A.17b})$$

with  $\sigma = \pm 1$  corresponding to  $J_z = \pm 1/2$  ( $J_z = \pm 3/2$ ) for electrons (heavy holes). Here,  $|S\rangle$  denotes a state of  $s$  symmetry, and  $|x\rangle$  a  $p$  state directed

along  $x$ . In the Förster term, only spin diagonal terms  $\sigma_c = \sigma_v = \sigma$  give a contribution. However, these states are coupled, as we show now. The dipole vector in Eq. (A.16) carries one spin label

$$\boldsymbol{\mu}_{cv}^\sigma = \langle s | \mathbf{r} | x + i\sigma y \rangle / \sqrt{2} = (\mathbf{e}_x + i\sigma \mathbf{e}_y) \mu / \sqrt{2} \quad (\text{A.18})$$

and contains the basic dipole moment  $\mu = \langle s | x | x \rangle$ . While the scalar product

$$\boldsymbol{\mu}_{cv}^\sigma \cdot (\boldsymbol{\mu}_{cv}^{\sigma'})^* = \frac{\mu^2}{2} (\mathbf{e}_x + i\sigma \mathbf{e}_y) \cdot (\mathbf{e}_x - i\sigma' \mathbf{e}_y) = \frac{\mu^2}{2} (1 + \sigma\sigma') = \mu^2 \delta_{\sigma\sigma'} \quad (\text{A.19})$$

is spin diagonal, we have

$$\mathbf{R} \cdot \boldsymbol{\mu}_{cv}^\sigma = \mu (X + i\sigma Y) / \sqrt{2} \quad (\text{A.20})$$

and the Förster potential (A.15) become

$$W_F^{\sigma\sigma'}(\mathbf{R}) = \frac{e^2 \mu^2}{\epsilon_\infty R^5} \left[ R^2 \delta_{\sigma\sigma'} - \frac{3}{2} (X + i\sigma Y)(X - i\sigma' Y) \right]. \quad (\text{A.21})$$

The spin conserving term ( $\sigma = \sigma'$ ) reads

$$W_F^{11}(\mathbf{R}) = W_F^{-1-1}(\mathbf{R}) = \frac{e^2 \mu^2}{\epsilon_\infty R^5} [Z^2 - (X^2 + Y^2)/2], \quad (\text{A.22})$$

while the spin scattering term is

$$W_F^{1-1}(\mathbf{R}) = W_F^{-11}(\mathbf{R}) = \frac{e^2 \mu^2}{\epsilon_\infty R^5} \frac{3}{2} (X + i\sigma Y)^2. \quad (\text{A.23})$$

The Förster potential in Eq. (A.15) is derived in the limit of dipole-dipole interaction. Its functional form is completely given by symmetry. The actual shape of the Wannier functions determines only the prefactor  $\mu$ . We now show that the same holds for the Coulomb correction in Eq. (A.12). Let us focus on the electron-hole term. For the  $x - y$  symmetry of Eqs. (A.17), one has  $\overline{x^2} = \overline{y^2}$ , and defining the anisotropy

$$\xi = \overline{x^2} - \overline{z^2}, \quad (\text{A.24})$$

we find the simple result

$$\Delta W_C(\mathbf{R}) = \frac{\xi}{\mu^2} W_F(\mathbf{R}). \quad (\text{A.25})$$

Note that only the hole state contribute to  $\xi$ . To be specific, if one approximate the Wannier functions by Gauss orbitals

$$w_c(\mathbf{r}) = \frac{1}{N} \exp(-r^2/4\mu^2), \quad (\text{A.26a})$$

$$w_v(\mathbf{r}) = \frac{x + iy}{\sqrt{2}\mu N} \exp(-r^2/4\mu^2), \quad (\text{A.26b})$$

with normalization  $N^2 = (2\pi)^{3/2} \mu^3$ . By construction the length scale equals the basic dipole  $\mu$ . The anisotropy come out to be  $\xi = d^2$ , ending up with

$$\Delta W_C(\mathbf{R}) = W_F(\mathbf{R}). \quad (\text{A.27})$$

The Coulomb correction is just as important as the Förster correction. However, spin transfer due to anisotropy rests exclusively on the nondiagonal Förster term.



## Acknowledgments

During the last four years I met many people that gave me great professional and emotional support. The moment to thank them has come. I'll also have the opportunity to thank the other people to whom I definitely should have said "thank you" for long time.

First of all, I wish to thank my supervisor Prof. Vincenzo Savona for giving me the chance to work in his group, but especially for his availability, humanity and patience. Begin and end being opposite and complementary concepts, it is at this point that I'd like to acknowledge the members of the jury, Prof. Robert Schaller, Prof. Andrea Fiore, Dr. Wolfgang Langbein and Dr. Paolo Schwendimann for their precious comments that took me to this final version of my thesis.

The research brought that is in your hands is the result of several collaborations. For Chapter 2 on radiative interaction, I wish to acknowledge fruitful discussions with Prof. Antonio Quattropani, Dr. Paolo Schwendimann and Prof. Roland Zimmermann. For Chapter 3 on exciton-phonon coupling, I acknowledge Prof. Roland Zimmermann and Dr. Wolfgang Langbein who, with their comments, allowed us to improve several points of the study. For Chapter 4 on theoretical modeling of heterodyne spectral interferometry, I am very thankful to Dr. Wolfgang Langbein for suggesting the topic, and for enlightening discussions. In particular, I wish to acknowledge Prof. Roland Zimmermann for directing us to a correct description of the Coulomb interaction between quantum dot electron states presented in Sec. 1.3 and Appendix A, which was fundamental to develop realistic models in Chapter 3 and Chapter 4. I also wish to thank my colleagues Davide Sarchi and Stefano Portolan for all the things that I learned from them in our discussions and for their moral support, especially during the writing of the thesis.

At this point I wish to acknowledge some people not directly involved in my work, whose support and mere presence helped me in overcoming the obstacles that, from time to time, I had to face. I must start with thanking my parents as well as my sisters along with their husbands and children for their love and constant encouragement and for helping me to become what I am, which is, actually, not that bad. Then, I wish to thank all those friends with whom I shared my first experiences in this complicated life since I was just a little "scugnizz'e Napule", and who still have time for me even if our lives have taken different directions. In particular I thank Davide, Giorgio, Giulio, Mimmo, Alessandro, Alex sensei, Antonio, Antonino, Marco Filippi, Marco Serpico, Otti and Raffaele for making me feel at home each time we meet, as if I had never left Napoli.

Going back over these last few years, I wish to thank all the people working at the Institute of Theoretical Physics for contributing to create the familiar atmosphere that made it so enjoyable to come to work every morning at the EPFL, in spite of rain, mist and snow! In particular, I thank Pascal with whom, to say it in his words, I shared much more than the office, and Aric for his curiosity toward life. I also thank Leonor and Séverine for the coffee-breaks and to be "ces obscurs objets du désir" of the corridor, Claude for turning himself into Mr. Hyde from time to time, and Rico for always having the good answer and also for the American coffee machine.

Then, I wish to thank all the members of my "Swiss family", that every day makes me feel at home more than if the Lemman Lake was salty. So, thanks to Marco and Alex for the beer (and to all the "La Bossette" community), to Gianluca for listening more than speaking, to Lorenzo and to the Grancona-Valdagno connection for "taking their time", to Nicola and Lucia for Clara, to Lorenzo and Cristina for all their improbable friends, to Plamen and Ion for teaching me the Eastern philosophy: "life is hard, but it could be harder", "we are hungry, but we are free in our country" and many more, to Adina for making of Ion an honest man, to Carlo for always having the right word at the right moment, to Klaus for Santa Krauss and uncle Hans, to Patricia for trying to kill us at the mountains with the complicity of Rosa and Oscar, to Michel for dancing like a god and to Jonas for trying to emulate him, to Mariachiara and Elisa for explaining the difference between coming from Rome or coming from anywhere else, to Caterina for her strength and her gentleness, to Petra for the pirate, to Marco for the amazing experience of the "Street Parade", to Jaqueline, Laura, Elisa, Nico, Nicu, Sam (he), Sam (she) for giving me their precious friendship.

A special thanks goes to Joanna, for bearing with me with devotion during the last months and for gracing me with her gentle smile even when I deserved to be slapped.

My last thanks are for Marina, Giulia and Miriam for driving me crazy almost all the time and for being so unique each one in their own way. You have been strong reference points for me in the last years, helping me to learn something about myself and, perhaps, about others.

# Bibliography

- [Andr 90] L. C. Andreani and F. Bassani. “Exchange interaction and polaron effects in quantum-well excitons”. *Physical Review B (Condensed Matter)*, Vol. 41, No. 11, pp. 7536–7544, 1990.
- [Andr 94] L. C. Andreani. Optical Transitions, Excitons, and Polaritons in Bulk and Low-Dimensional Semiconductor Structures *in* Confined electrons and photons *vol. 340 of* NATO Advanced Study Institute, Series B. Plenum Press, New York, 1994. Edited by E. Burstein and C. Weisbuch.
- [Axt 05] V. M. Axt, T. Kuhn, A. Vagov, and F. M. Peeters. “Phonon-induced pure dephasing in exciton-biexciton quantum dot systems driven by ultrafast laser pulse sequences”. *Physical Review B (Condensed Matter and Materials Physics)*, Vol. 72, No. 12, p. 125309, 2005.
- [Baie 04] M. H. Baier, S. Watanabe, E. Pelucchi, and E. Kapon. “High uniformity of site-controlled pyramidal quantum dots grown on prepatterned substrates”. *Applied Physics Letters*, Vol. 84, No. 11, pp. 1943–1945, 2004.
- [Bass 75] F. Bassani and G. Pastori Parravicini. Electronic states and optical transitions in solids. Pergamon Press, New York, 1975. Edited by R. A. Ballinger.
- [Bast 92] G. Bastard. Wave mechanics applied to semiconductor heterostructures. Les éditions de physique, Les Ulis, 1992.
- [Baye 01] M. Bayer, P. Hawrylak, K. Hinzer, S. Fafard, M. Korkusinski, Z. R. Wasilewski, O. Stern, and A. Forchel. “Coupling and entangling of quantum states in quantum dot molecules”. *Science*, Vol. 291, No. 5503, pp. 451–453, 2001.

- [Benn 00] C. H. Bennet and D. P. Di Vincenzo. “Quantum Information and Computation”. *Nature*, Vol. 404, No. , pp. 247–255, 2000.
- [Berg 88] P. R. Berger, K. Chang, P. Bhattacharya, J. Singh, and K. K. Bajaj. “Role of strain and growth conditions on the growth front profile of  $\text{In}_x\text{Ga}_{1-x}\text{As}$  on GaAs during the pseudomorphic growth regime”. *Applied Physics Letters*, Vol. 53, No. 8, pp. 684–686, 1988.
- [Bert 04] A. Bertoni, M. Rontani, G. Goldoni, F. Troiani, and E. Molinari. “Field-controlled suppression of phonon-induced transitions in coupled quantum dots”. *Applied Physics Letters*, Vol. 85, No. 20, pp. 4729–4731, 2004.
- [Beso 01] L. Besombes, K. Kheng, L. Marsal, and H. Mariette. “Acoustic phonon broadening mechanism in single quantum dot emission”. *Phys. Rev. B*, Vol. 63, No. 15, p. 155307, Mar 2001.
- [Best 04] G. Bester, J. Shumway, and A. Zunger. “Theory of Excitonic Spectra and Entanglement Engineering in Dot Molecules”. *Physical Review Letters*, Vol. 93, No. 4, p. 047401, 2004.
- [Bimb 99] D. Bimberg, M. Grundmann, and N. Ledentsov. Quantum Dot Heterostructures. John Wiley & Sons, Chichester, 1999.
- [Biol 00] E. Biolatti, R. C. Iotti, P. Zanardi, and F. Rossi. “Quantum Information Processing with Semiconductor Macroatoms”. *Phys. Rev. Lett.*, Vol. 85, No. 26, pp. 5647–5650, Dec 2000.
- [Bock 93] U. Bockelmann. “Exciton relaxation and radiative recombination in semiconductor quantum dots”. *Physical Review B (Condensed Matter)*, Vol. 48, No. 23, pp. 17637–17640, 1993.
- [Bona 98] N. H. Bonadeo, G. Chen, D. Gammon, D. S. Katzer, D. Park, and D. G. Steel. “Nonlinear Nano-Optics: Probing One Exciton at a Time”. *Physical Review Letters*, Vol. 81, No. 13, pp. 2759–2762, 1998.
- [Borc 05] C. N. Borca, T. Zhang, X. Li, and S. T. Cundiff. “Optical two-dimensional Fourier transform spectroscopy of semiconductors”. *Chemical Physics Letters*, Vol. 416, No. 4-6, pp. 311–315, 2005.

- [Borr 01] P. Borri, W. Langbein, S. Schneider, U. Woggon, R. L. Sellin, D. Ouyang, and D. Bimberg. “Ultralong Dephasing Time in InGaAs Quantum Dots”. *Physical Review Letters*, Vol. 87, No. 15, p. 157401, 2001.
- [Borr 02] P. Borri, W. Langbein, S. Schneider, U. Woggon, R. L. Sellin, D. Ouyang, and D. Bimberg. “Rabi oscillations in the excitonic ground-state transition of InGaAs quantum dots”. *Physical Review B (Condensed Matter and Materials Physics)*, Vol. 66, No. 8, p. 081306, 2002.
- [Borr 03] P. Borri, W. Langbein, U. Woggon, M. Schwab, M. Bayer, S. Fafard, Z. Wasilewski, and P. Hawrylak. “Exciton Dephasing in Quantum Dot Molecules”. *Physical Review Letters*, Vol. 91, No. 26 I, pp. 2674011–2674014, 2003.
- [Bouw 00] E. A. Bouwmeester, D. and A. Zeilinger. *in The Physics of Quantum Information*. Springer, Berlin, 2000.
- [Brix 05] T. Brixner, J. Stenger, H. M. Vaswani, M. Cho, R. E. Blankenship, and G. R. Fleming. “Two-dimensional spectroscopy of electronic couplings in photosynthesis”. *Nature*, Vol. 434, No. 7033, pp. 625–628, 2005.
- [Burk 99] G. Burkard, D. Loss, and D. P. DiVincenzo. “Coupled quantum dots as quantum gates”. *Physical Review B - Condensed Matter and Materials Physics*, Vol. 59, No. 3, pp. 2070–2078, 1999.
- [Carl 94] N. Carlsson, W. Seifert, A. Petersson, P. Castrillo, M. E. Pistol, and L. Samuelson. “Study of the two-dimensional three-dimensional growth mode transition in metalorganic vapor phase epitaxy of GaInP/InP quantum-sized structures”. *Applied Physics Letters*, Vol. 65, No. 24, pp. 3093–3095, 1994.
- [Chem 01] D. S. Chemla and J. Shah. “Many-body and correlation effects in semiconductors”. *Nature*, Vol. 411, No. 6837, pp. 549–557, 2001.
- [Cho 71] A. Y. Cho. “Film Deposition by Molecular-Beam Techniques”. *Journal of Vacuum Science and Technology*, Vol. 8, No. 5, pp. S31–S38, 1971.
- [Citr 92] D. S. Citrin. “Long intrinsic radiative lifetimes of excitons in quantum wires”. *Physical Review Letters*, Vol. 69, No. 23, pp. 3393–3396, 1992.

- [Citr 93a] D. S. Citrin. “Quantum-wire excitons: Polaritons and exchange effects”. *Physical Review B (Condensed Matter)*, Vol. 48, No. 4, pp. 2535–2542, 1993.
- [Citr 93b] D. S. Citrin. “Radiative lifetimes of excitons in quantum wells: Localization and phase-coherence effects”. *Physical Review B (Condensed Matter)*, Vol. 47, No. 7, pp. 3832–3841, 1993.
- [Cund 94] S. T. Cundiff, A. Knorr, J. Feldmann, S. W. Koch, E. O. Göbel, and H. Nickel. “Rabi Flopping in Semiconductors”. *Phys. Rev. Lett.*, Vol. 73, No. 8, pp. 1178–1181, Aug 1994.
- [Duke 65] C. B. Duke and G. D. Mahan. “Phonon-Broadened Impurity Spectra. I. Density of States”. *Phys. Rev.*, Vol. 139, No. 6A, pp. A1965–A1982, Sep 1965.
- [Fafa 00] S. Fafard. “Near-surface InAs/GaAs quantum dots with sharp electronic shells”. *Applied Physics Letters*, Vol. 76, No. 19, pp. 2707–2709, 2000.
- [Fafa 99] S. Fafard, Z. R. Wasilewski, C. N. Allen, D. Picard, M. Spanner, J. P. McCaffrey, and P. G. Piva. “Manipulating the energy levels of semiconductor quantum dots”. *Physical Review B (Condensed Matter and Materials Physics)*, Vol. 59, No. 23, pp. 15368–15373, 1999.
- [Fano 61] U. Fano. “Effects of Configuration Interaction on Intensities and Phase Shifts”. *Physical Review*, Vol. 124, No. 6, pp. 1866–1878, 1961.
- [Fave 03] I. Faviero, G. Cassaboïs, R. Ferreira, D. Darson, C. Voisin, J. Tignon, C. Delalande, G. Bastard, P. Roussignol, and J. M. Gerard. “Acoustic phonon sidebands in the emission line of single InAs/GaAs quantum dots”. *Physical Review B (Condensed Matter and Materials Physics)*, Vol. 68, No. 23, p. 233301, 2003.
- [Fors 65] T. Förster. *in* Modern quantum chemistry. Academic, New York, 1965. Edited by O. Sinanoglu.
- [Gil 02] B. Gil and A. V. Kavokin. “Giant exciton-light coupling in ZnO quantum dots”. *Applied Physics Letters*, Vol. 81, No. 4, pp. 748–750, 2002.

- [Gold 85] L. Goldstein, F. Glas, J. Y. Marzin, M. N. Charasse, and G. L. Roux. “Growth by molecular beam epitaxy and characterization of InAs/GaAs strained-layer superlattices”. *Applied Physics Letters*, Vol. 47, No. 10, pp. 1099–1101, 1985.
- [Goup 02] S. V. Goupalov, R. A. Suris, P. Lavallard, and D. S. Citrin. “Exciton dephasing and absorption line shape in semiconductor quantum dots”. *IEEE Journal on Selected Topics in Quantum Electronics*, Vol. 8, No. 5, pp. 1009–1014, 2002.
- [Govo 03] A. O. Govorov. “Spin and energy transfer in nanocrystals without tunneling”. *Physical Review B - Condensed Matter and Materials Physics*, Vol. 68, No. 7, pp. 753151–753156, 2003.
- [Gran 93] N. Grandjean and J. Massies. “Epitaxial growth of highly strained  $\text{In}_x\text{Ga}_{1-x}\text{As}$  on GaAs(001): The role of surface diffusion length”. *Journal of Crystal Growth*, Vol. 134, No. 1-2, pp. 51–62, 1993.
- [Grun 95] M. Grundmann, O. Stier, and D. Bimberg. “InAs/GaAs pyramidal quantum dots: Strain distribution, optical phonons, and electronic structure”. *Physical Review B (Condensed Matter)*, Vol. 52, No. 16, pp. 11969–11981, 1995.
- [Hart 00] A. Hartmann, Y. Ducommun, E. Kapon, U. Hohenester, and E. Molinari. “Few-Particle Effects in Semiconductor Quantum Dots: Observation of Multicharged Excitons”. *Physical Review Letters*, Vol. 84, No. 24, pp. 5648–5651, 2000.
- [Haug 90] H. Haug and S. W. Koch. Quantum theory of the optical and electronic properties of semiconductors. World Scientific, Singapore, 1990.
- [Hopf 58] J. J. Hopfield. “Theory of the Contribution of Excitons to the Complex Dielectric Constant of Crystals”. *Physical Review*, Vol. 112, No. 5, pp. 1555–1567, 1958.
- [Houd 94] R. Houdre, C. Weisbuch, R. P. Stanley, U. Oesterle, P. Pellandini, and M. Illegems. “Measurement of cavity-polariton dispersion curve from angle resolved photoluminescence experiments”. *Physical Review Letters*, Vol. 73, No. 15, pp. 2043–2046, 1994.

- [Howa 85] R. E. Howard, L. D. Jackel, and W. J. Skocpol. “Nanostructures: fabrication and applications”. *Microelectronic Engineering*, Vol. 3, No. 1-4, pp. 3–16, 1985.
- [Htoo 02] H. Htoon, T. Takagahara, D. Kulik, O. Baklenov, A. L. Holmes, and C. K. Shih. “Interplay of Rabi Oscillations and Quantum Interference in Semiconductor Quantum Dots”. *Phys. Rev. Lett.*, Vol. 88, No. 8, p. 087401, Feb 2002.
- [Hugh 06] S. Hughes, H. Gotoh, and H. Kamada. “Classical and quantum optical correlation effects between single quantum dots: The role of the hopping photon”. *Physical Review B (Condensed Matter and Materials Physics)*, Vol. 74, No. 11, p. 115334, 2006.
- [Hybl 01] J. D. Hybl, A. A. Ferro, and D. M. Jonas. “Two-dimensional Fourier transform electronic spectroscopy”. *Journal of Chemical Physics*, Vol. 115, No. 14, pp. 6606–6622, 2001.
- [Jord 93] S. Jorda, U. Rossler, and D. Broido. “Fine structure of excitons and polariton dispersion in quantum wells”. *Physical Review B (Condensed Matter)*, Vol. 48, No. 3, pp. 1669–1677, 1993.
- [Jord 94] S. Jorda. “Quantum theory of the interaction of quantum-well excitons with electromagnetic waveguide modes”. *Physical Review B (Condensed Matter)*, Vol. 50, No. 4, pp. 2283–2292, 1994.
- [Kama 01] H. Kamada, H. Gotoh, J. Temmyo, T. Takagahara, and H. Ando. “Exciton Rabi Oscillation in a Single Quantum Dot”. *Phys. Rev. Lett.*, Vol. 87, No. 24, p. 246401, Nov 2001.
- [Kapo 87] E. Kapon, M. C. Tamargo, and D. M. Hwang. “Molecular beam epitaxy of GaAs/AlGaAs superlattice heterostructures on non-planar substrates”. *Applied Physics Letters*, Vol. 50, No. 6, pp. 347–349, 1987.
- [Knox 63] R. S. Knox. *Theory of Excitons in Solid State Physics*. Academic Press, New York, 1963. F. Seitz and D. Turnbull eds.
- [Kohn 58] W. Kohn. “Interaction of Charged Particles in a Dielectric”. *Phys. Rev.*, Vol. 110, No. 4, pp. 857–864, May 1958.
- [Komu 83] M. Komuro, H. Hiroshima, H. Tanoue, and T. Kanayama. “Maskless etching of a nanometer structure by focused ion

- beams". *Journal of Vacuum Science and Technology B: Microelectronics and Nanometer Structures*, Vol. 1, No. 4, pp. 985–989, 1983.
- [Krau 97] P. R. Krauss and S. Y. Chou. "Nano-compact disks with 400 Gbit/in<sup>2</sup> storage density fabricated using nanoimprint lithography and read with proximal probe". *Applied Physics Letters*, Vol. 71, No. 21, pp. 3174–3176, 1997.
- [Kren 05] H. J. Krenner, M. Sabathil, E. C. Clark, A. Kress, D. Schuh, M. Bichler, G. Abstreiter, and J. J. Finley. "Direct Observation of Controlled Coupling in an Individual Quantum Dot Molecule". *Physical Review Letters*, Vol. 94, No. 5, p. 057402, 2005.
- [Krum 02] B. Krummheuer, V. M. Axt, and T. Kuhn. "Theory of pure dephasing and the resulting absorption line shape in semiconductor quantum dots". *Physical Review B (Condensed Matter and Materials Physics)*, Vol. 65, No. 19, p. 195313, 2002.
- [Kubo 57] R. Kubo. "Statistical mechanical theory of irreversible processes. I. General theory and simple applications to magnetic and conduction problems". *Journal of the Physical Society of Japan*, Vol. 12, No. 6, pp. 570–586, 1957.
- [Kuri 88] G. Kurizki and A. Z. Genack. "Suppression of molecular interactions in periodic dielectric structures". *Physical Review Letters*, Vol. 61, No. 19, pp. 2269–2271, 1988.
- [Lang 00] W. Langbein and J. M. Hvam. "Dephasing in the quasi-two-dimensional exciton-biexciton system". *Phys. Rev. B*, Vol. 61, No. 3, pp. 1692–1695, Jan 2000.
- [Lang 04a] W. Langbein, P. Borri, U. Woggon, V. Stavarache, D. Reuter, and A. D. Wieck. "Control of fine-structure splitting and biexciton binding in In<sub>x</sub>Ga<sub>1-x</sub>As quantum dots by annealing". *Physical Review B (Condensed Matter and Materials Physics)*, Vol. 69, No. 16, p. 161301, 2004.
- [Lang 04b] W. Langbein, P. Borri, U. Woggon, V. Stavarache, D. Reuter, and A. D. Wieck. "Radiatively limited dephasing in InAs quantum dots". *Physical Review B (Condensed Matter and Materials Physics)*, Vol. 70, No. 3, p. 033301, 2004.

- [Lang 06] W. Langbein and B. Patton. “Heterodyne spectral interferometry for multidimensional nonlinear spectroscopy of individual quantum systems”. *Optics Letters*, Vol. 31, No. 8, pp. 1151–1153, 2006.
- [Lang 07] W. Langbein and B. Patton. “Transient coherent nonlinear spectroscopy of single quantum dots”. *Submitted to Journal of Physics: Condensed Matter*, Vol. , No. , p. , 2007.
- [Lebe 90] J. A. Lebens, C. S. Tsai, K. J. Vahala, and T. F. Kuech. “Application of selective epitaxy to fabrication of nanometer scale wire and dot structures”. *Applied Physics Letters*, Vol. 56, No. 26, pp. 2642–2644, 1990.
- [Li 03] X. Li, Y. Wu, D. Steel, D. Gammon, T. H. Stievater, D. S. Katzer, D. Park, C. Piermarocchi, and L. J. Sham. “An All-Optical Quantum Gate in a Semiconductor Quantum Dot”. *Science*, Vol. 301, No. 5634, pp. 809–811, 2003.
- [Li 06] X. Li, T. Zhang, C. N. Borca, and S. T. Cundiff. “Many-Body Interactions in Semiconductors Probed by Optical Two-Dimensional Fourier Transform Spectroscopy”. *Physical Review Letters*, Vol. 96, No. 5, p. 057406, 2006.
- [Litv 02] D. Litvinov, A. Rosenauer, D. Gerthsen, P. Kratzert, M. Rabe, and F. Henneberger. “Influence of the growth procedure on the Cd distribution in CdSe/ZnSe heterostructures: Stranski–Krastanov versus two-dimensional islands”. *Applied Physics Letters*, Vol. 81, No. 4, pp. 640–642, 2002.
- [Loss 98] D. Loss and D. P. DiVincenzo. “Quantum computation with quantum dots”. *Phys. Rev. A*, Vol. 57, No. 1, pp. 120–126, Jan 1998.
- [Love 03] B. W. Lovett, J. H. Reina, A. Nazir, and G. A. D. Briggs. “Optical schemes for quantum computation in quantum dot molecules”. *Physical Review B (Condensed Matter and Materials Physics)*, Vol. 68, No. 20, p. 205319, 2003.
- [Lutt 55] J. M. Luttinger and W. Kohn. “Motion of Electrons and Holes in Perturbed Periodic Fields”. *Phys. Rev.*, Vol. 97, No. 4, pp. 869–883, Feb 1955.

- [Macc 00] C. Macchiavello. Quantum computation and quantum information theory. World Scientific, Singapore, 2000. Edited by C. Macchiavello, G. M. Palma and A. Zeilinger.
- [Maha 90] G. Mahan. Many particle physics. Plenum Press, New York, 1990.
- [Mand 95] L. Mandel and E. Wolf. Optical coherence and quantum optics. Cambridge University Press, Cambridge, 1995.
- [Mann 06] G. Mannarini and R. Zimmermann. “Near-field spectra of quantum well excitons with non-Markovian phonon scattering”. *Phys. Rev. B*, Vol. 73, No. 11, p. 115325, Mar 2006.
- [Mart 98] O. J. F. Martin and N. B. Piller. “Electromagnetic scattering in polarizable backgrounds”. *Physical Review E (Statistical Physics, Plasmas, Fluids, and Related Interdisciplinary Topics)*, Vol. 58, No. 3, pp. 3909–3915, 1998.
- [Mo 90] Y. W. Mo, D. E. Savage, B. S. Swartzentruber, and M. G. Lagally. “Kinetic pathway in stranski-krastanov growth of Ge on Si(001)”. *Physical Review Letters*, Vol. 65, No. 8, pp. 1020–1023, 1990.
- [Mulj 04] E. A. Muljarov and R. Zimmermann. “Dephasing in Quantum Dots: Quadratic Coupling to Acoustic Phonons”. *Physical Review Letters*, Vol. 93, No. 23, p. 237401, 2004.
- [Mulj 05] E. A. Muljarov, T. Takagahara, and R. Zimmermann. “Phonon-Induced Exciton Dephasing in Quantum Dot Molecules”. *Physical Review Letters*, Vol. 95, No. 17, p. 177405, 2005.
- [Mulj 06a] E. A. Muljarov and R. Zimmermann. “Comment on Dephasing Times in Quantum Dots due to Elastic LO Phonon-Carrier Collisions”. *Phys. Rev. Lett.*, Vol. 96, No. 1, p. 019703, Jan 2006.
- [Mulj 06b] E. A. Muljarov and R. Zimmermann. “LO Phonon-Induced Exciton Dephasing in Quantum Dots: an Exactly Solvable Model”. *arXiv:cond-mat/0605545 v1*, Vol. , No. , p. , 2006.
- [Nabe 94] Y. Nabetani, T. Ishikawa, S. Noda, and A. Sasaki. “Initial growth stage and optical properties of a three-dimensional InAs structure on GaAs”. *Journal of Applied Physics*, Vol. 76, No. 1, pp. 347–351, 1994.

- [Notz 94] R. Nötzel, J. Temmyo, and T. Tamamura. “Self-organized growth of strained InGaAs quantum disks”. *Nature*, Vol. 369, No. 6476, pp. 131–133, 1994.
- [Oppe 41] J. R. Oppenheimer. “Internal Conversion in photosynthesis, in Proceedings of the American Physical Society”. *Physical Review*, Vol. 60, No. , pp. 158–165, 1941.
- [Ortn 03] G. Ortner, M. Bayer, A. Larionov, V. B. Timofeev, A. Forchel, Y. B. Lyanda-Geller, T. L. Reinecke, P. Hawrylak, S. Fafard, and Z. Wasilewski. “Fine Structure of Excitons in InAs/GaAs Coupled Quantum Dots: A Sensitive Test of Electronic Coupling”. *Physical Review Letters*, Vol. 90, No. 8, p. 086404, 2003.
- [Ortn 05a] G. Ortner, M. Bayer, Y. Lyanda-Geller, T. L. Reinecke, A. Kress, J. P. Reithmaier, and A. Forchel. “Control of Vertically Coupled InGaAs/GaAs Quantum Dots with Electric Fields”. *Physical Review Letters*, Vol. 94, No. 15, p. 157401, 2005.
- [Ortn 05b] G. Ortner, R. Oulton, H. Kurtze, M. Schwab, D. R. Yakovlev, M. Bayer, S. Fafard, Z. Wasilewski, and P. Hawrylak. “Energy relaxation of electrons in InAs/GaAs quantum dot molecules”. *Physical Review B (Condensed Matter and Materials Physics)*, Vol. 72, No. 16, p. 165353, 2005.
- [Para 05] G. Parascandolo and V. Savona. “Long-range radiative interaction between semiconductor quantum dots”. *Physical Review B - Condensed Matter and Materials Physics*, Vol. 71, pp. 45335–10, 2005.
- [Para 07] G. Parascandolo and V. Savona. “Long-range radiative interaction between semiconductor quantum dots”. *Superlattices and Microstructures* (to appear), Vol. , p. , 2007.
- [Patt 05] B. Patton, U. Woggon, and W. Langbein. “Coherent Control and Polarization Readout of Individual Excitonic States”. *Physical Review Letters*, Vol. 95, No. 26, p. 266401, 2005.
- [Patt 06] B. Patton, W. Langbein, U. Woggon, L. Maingault, and H. Mariette. “Time- and spectrally-resolved four-wave mixing in single CdTe/ZnTe quantum dots”. *Physical Review B (Condensed Matter and Materials Physics)*, Vol. 73, No. 23, p. 235354, 2006.

- [QCR 04] QCR. “A Quantum Information Science and Technology Roadmap”. 2004. [http://qist.lanl.gov/qcomp\\_map.shtml](http://qist.lanl.gov/qcomp_map.shtml).
- [Quoc 98] F. Quochi, G. Bongiovanni, A. Mura, J. L. Staehli, B. Deveaud, R. P. Stanley, U. Oesterle, and R. Houdre. “Strongly Driven Semiconductor Microcavities: From the Polariton Doublet to an ac Stark Triplet”. *Physical Review Letters*, Vol. 80, No. 21, pp. 4733–4736, 1998.
- [Rodt 03] S. Rodt, R. Heitz, A. Schliwa, R. L. Sellin, F. Guffarth, and D. Bimberg. “Repulsive exciton-exciton interaction in quantum dots”. *Phys. Rev. B*, Vol. 68, No. 3, p. 035331, Jul 2003.
- [Savo 02] V. Savona. Radiative coupling vs. exciton localization in quantum wells, in *Radiation-Matter Interaction in Confined Systems, pages 101-111*, L. C. Andreani, G. Benedek and E. Molinari Editor. SIF, Bologna, 2002.
- [Savo 95] V. Savona, L. C. Andreani, P. Schwendimann, and A. Quattropani. “Quantum well excitons in semiconductor microcavities: unified treatment of weak and strong coupling regime”. *Solid State Communications*, Vol. 93, No. 9, pp. 733–739, 1995.
- [Savo 96] V. Savona, F. Tassone, C. Piermarocchi, A. Quattropani, and P. Schwendimann. “Theory of polariton photoluminescence in arbitrary semiconductor microcavity structures”. *Physical Review B (Condensed Matter)*, Vol. 53, No. 19, pp. 13051–13062, 1996.
- [Sche 07] M. Scheibner, T. Schmidt, L. Worschech, A. Forchel, G. Bacher, T. Passow, and D. Hommel. “Superradiance of quantum dots”. *Nature Physics*, Vol. 3, No. 2, pp. 106–110, 2007.
- [Schu 99] A. Schülzgen, R. Binder, M. E. Donovan, M. Lindberg, K. Wundke, H. M. Gibbs, G. Khitrova, and N. Peyghambarian. “Direct Observation of Excitonic Rabi Oscillations in Semiconductors”. *Phys. Rev. Lett.*, Vol. 82, No. 11, pp. 2346–2349, Mar 1999.
- [Sham 66] L. J. Sham and T. M. Rice. “Many-Particle Derivation of the Effective-Mass Equation for the Wannier Exciton”. *Phys. Rev.*, Vol. 144, No. 2, pp. 708–714, Apr 1966.

- [Solo 96] G. S. Solomon, J. A. Trezza, A. F. Marshall, and J. S. Harris, Jr. “Vertically Aligned and Electronically Coupled Growth Induced InAs Islands in GaAs”. *Phys. Rev. Lett.*, Vol. 76, No. 6, pp. 952–955, Feb 1996.
- [Stie 99] O. Stier, M. Grundmann, and D. Bimberg. “Electronic and optical properties of strained quantum dots modeled by 8-band k [center-dot] p theory”. *Physical Review B (Condensed Matter and Materials Physics)*, Vol. 59, No. 8, pp. 5688–5701, 1999.
- [Stin 06] E. A. Stinaff, M. Scheibner, A. S. Bracker, I. V. Ponomarev, V. L. Korenev, M. E. Ware, M. F. Doty, T. L. Reinecke, and D. Gammon. “Optical Signature of Coupled Quantum Dots”. *Science*, Vol. 311, No. , pp. 636–638, 2006.
- [Stra 37] I. N. Stranski and L. Krastanow. “Zur Theorie der orientierten Ausscheidung von Ionenkristallen aufeinander”. *Sitzungsberichte d. akad. d. Wissenschaften in Wien*, Vol. Band 146, No. Abt. IIb, p. 797, 1937.
- [Tass 90] F. Tassone, F. Bassani and L. C. Andreani. “Resonant and surface polaritons in quantum wells”. *Nuovo Cimento*, Vol. 12 D, No. 12, pp. 1673–1687, 1990.
- [Tass 95] F. Tassone and F. Bassani. “Reflectivity of the quantum grating and the grating polariton”. *Physical Review B (Condensed Matter)*, Vol. 51, No. 23, pp. 16973–16983, 1995.
- [Troi 00] F. Troiani, U. Hohenester, and E. Molinari. “Exploiting exciton-exciton interactions in semiconductor quantum dots for quantum-information processing”. *Physical Review B (Condensed Matter and Materials Physics)*, Vol. 62, No. 4, pp. R2263–R2266, 2000.
- [Van 94] R. Van Grondelle, J. P. Dekker, T. Gillbro, and V. Sundstrom. “Energy transfer and trapping in photosynthesis”. *Biochimica et Biophysica Acta - Bioenergetics*, Vol. 1187, pp. 1–65, 1994.
- [Vill 04] J. M. Villas-Boas, A. O. Govorov, and S. E. Ulloa. “Coherent control of tunneling in a quantum dot molecule”. *Physical Review B (Condensed Matter and Materials Physics)*, Vol. 69, No. 12, p. 125342, 2004.

- [Weis 92] C. Weisbuch, M. Nishioka, A. Ishikawa, and Y. Arakawa. “Observation of the coupled exciton-photon mode splitting in a semiconductor quantum microcavity”. *Physical Review Letters*, Vol. 69, No. 23, pp. 3314–3317, 1992.
- [Xie 95] Q. Xie, A. Madhukar, P. Chen, and N. P. Kobayashi. “Vertically self-organized InAs quantum box islands on GaAs(100)”. *Physical Review Letters*, Vol. 75, No. 13, pp. 2542–2545, 1995.
- [Yu 96] P. Yu and M. Cardona. *Fundamentals of semiconductors*. Springer-Verlag, Berlin, 1996.
- [Zana 98] P. Zanardi and F. Rossi. “Quantum information in semiconductors: Noiseless encoding in a quantum-dot array”. *Physical Review Letters*, Vol. 81, No. 21, pp. 4752–4755, 1998.
- [Zimm 02] R. Zimmermann and E. Runge. *Dephasing in quantum dots via electron-phonon interaction*, in *Proceedings of the 26th ICPS, Edinburgh, Scotland, United Kingdom*. Inst. of Physics Publ., Bristol and Philadelphia, 2002.
- [Zren 02] A. Zrenner, E. Beham, S. Stuffer, F. Findeis, M. Bichler, and G. Abstreiter. “Coherent properties of a two-level system based on a quantum-dot photodiode”. *Nature*, Vol. 418, No. 6898, pp. 612–614, 2002.



# Curriculum Vitae

**Gaetano Parascandolo**

Born on May 14<sup>th</sup>, 1977, in Naples

EPFL SB ITP GR-SA  
PH H2 455 (Bâtiment PH)  
Station 3  
CH-1015 Lausanne  
Tel. +41-21-693 3417

**E-mail:** Gaetano.Parascandolo@epfl.ch

## Education:

May 2003 - Present: PhD studies, Theoretical Physics Institute of the Ecole Polytechnique Fédérale de Lausanne, Switzerland, under the direction of Prof. Vincenzo Savona.

October 1996 - October 2002: Undergraduate studies, Faculty of Physics of the Università degli studi di Napoli Federico II, Italy. Degree in Physics from the Università degli studi di Napoli Federico II (Laurea in Fisica, 110/110 cum laude), under the supervision of Prof. Domenico Ninno and Dr. Giovanni Cantele. Title of the dissertation: Effetti di correlazione elettrone-elettrone in strutture di silicio poroso (Electron-electron correlation effects in porous silicon nanostructures).

September 1990 - July 1996: High school studies, Napoli, Italy. Scientific Bachelor.

## Professional experience

Research in the frame of PhD studies. 200 hours of teaching activities (assistant for undergraduate courses).

April 28<sup>th</sup> - May 5<sup>th</sup>, 2001 : Guide for the scientific exposition Frammenti di imparagiocando , promoted by INFN (National Institute for the Physics of Matter).

## Teaching experience

From October 2003 to present assists in the following undergraduate courses: introduction to numerical simulation, general physics, mathe-

mathematical analysis, statistical physics, advanced statistical physics.

### **Research interests**

Theory of condensed matter physics. In particular, electronic states and optical properties of semiconductor nanostructures.

### **Language skills**

Italian: mother language.

English: fluent, spoken and written.

French: fluent, spoken and written.

German: basic knowledge.

Spanish: basic knowledge.

### **Other skills**

Knowledge of Windows XP, Macintosh, Linux and Unix operating systems. Matlab programming, especially for computational physics and numerical simulations. Basic knowledge of Fortran 77 and Fortran 90 programming.

### **Publications**

G. Parascandolo, G. Cantele, D. Ninno and G. Iadonisi, Interplay between quantum confinement and electron-electron interaction in deformed silicon quantum wires, *Phys. Rev. B*, **68**, 245318 (2003).

G. Parascandolo and V. Savona, Long-range radiative interaction between semiconductor quantum dots, *Phys. Rev. B*, **71**, 45335 (2005).

G. Parascandolo and V. Savona, Long-range radiative interaction between semiconductor quantum dots, *Superlattices and Microstructures*, doi: 10.1016/j.spmi.2007.03.007, 2007.

### **Conferences**

G. Parascandolo and V. Savona, Long-range radiative interaction between semiconductor quantum dots, EQUONT-3, September 19-23, 2004. Cambridge, United Kingdom. (poster)

G. Parascandolo and V. Savona, Dephasing in quantum dot molecules via exciton-acoustic phonon coupling, OECS-9, September 5-10, 2005. Southampton, United Kingdom. (oral)

G. Parascandolo and V. Savona, Theory of transient four-wave mixing in coupled quantum dot systems, ICPS-28, July 24-28, 2006. Vienna, Austria. (poster)

G. Parascandolo and V. Savona, Long-range radiative interaction between semiconductor quantum dots, PLMCN6, September 25-29, 2006. Magdeburg, Germany. (oral)